**Title**

Low Cycle Fatigue Behavior and Kinetics of Dislocation Glide in Alloys for Structural and Hydrogen Energy Applications

**Author**

Marques Oliveira, Dayane

**Publication Date**

2022

# Low Cycle Fatigue Behavior and Kinetics of Dislocation Glide in Alloys for Structural and Hydrogen Energy Applications

By

DAYANE MARQUES OLIVEIRA
DISSERTATION

Submitted in partial satisfaction of the requirements for the degree of

DOCTOR OF PHILOSOPHY

in

Materials Science and Engineering

in the

OFFICE OF GRADUATE STUDIES

of the

UNIVERSITY OF CALIFORNIA

DAVIS

Approved:

Jeffery C. Gibeling, Chair

Jeremy K. Mason

Michael R. Hill

Committee in Charge

2022

# Dedication

*This dissertation is dedicated to my parents, Geralda Aparecida Lana Oliveira and Jose Nazario de Oliveira, who did not measure efforts to support my journey (far) away from home. It is also dedicated to my fiancé, Nicholas Wayne Lundgren, who has been a constant source of encouragement, support, and inspiration throughout my Ph.D. program.*

# Abstract

This study explores critical issues in the fatigue behavior and fundamental mechanisms of cyclic deformation in alloys for structural and hydrogen-energy applications using plastic strain-controlled low cycle fatigue (LCF) and constant microstructure plastic strain rate change experiments. The materials of interest are strain-hardened Type 316L austenitic stainless steel and annealed CrMnFeCoNi high entropy alloy (HEA), both in the hydrogen-precharged (H-precharged) and non-charged conditions. The LCF tests were conducted at a constant plastic strain rate of $1\text{x}10^{-3}$ $s^{-1}$, probing plastic strain amplitudes between 0.1% and 0.7% in 316L and between 0.3% and 0.8% in the CrMnFeCoNi alloy. The plastic strain rate change experiments are a unique type of experiment designed to explore the fundamental mechanisms that control dislocation glide in the context of thermal activation theory. They were conducted periodically at two different regions of the lifetime, probing operational activation area values that represent the evolving and dynamic equilibrium states of the microstructure at plastic strain amplitudes between 0.3% and 0.8%.

In the strain-hardened 316L austenitic stainless steel, cyclic stress response curves show continuous softening in both H-precharged and non-charged conditions at all plastic strain amplitudes. Internal hydrogen increases the cyclic strength by enhancing the effective component of the flow stresses, especially at low plastic strain amplitude. However, the increase in effective stress is accompanied by a significant reduction in initiation and total fatigue lifetimes in the H-precharged condition. At high amplitudes, back stresses become more significant in both material conditions and, although hydrogen still leads to earlier failure, the difference in LCF lifetimes is reduced. Scanning electron microscopy (SEM) observations reveal earlier onset of multiple slip in the presence of hydrogen at low strain amplitudes, indicating that the premature failure in the H-

precharged condition is likely due to microcracks initiating at intersecting planar slip bands. Calculations of operational activation area during cyclic deformation suggest that dislocation glide is controlled by solute atoms, forest dislocations and cross slip in all material conditions, except at low plastic strain amplitudes, where cross slip is not active in the H-precharged condition. In the context of thermally activated deformation, hydrogen affects the dislocation glide resistance by decreasing both the dislocation activation distance and spacing. The Haasen plot also indicates the presence athermal obstacles to dislocation glide. Based on transmission scanning electron microscopy (STEM) observations, these obstacles are likely to be dislocation cell walls in the non-charged condition at all amplitudes and in the H-precharged condition at high amplitudes, and dense dislocation tangles in the H-precharged condition at low strain amplitude. Because different dislocation arrangements are favored at different plastic strain amplitudes in the presence of hydrogen, the athermal stresses also are also amplitude dependent in the H-precharged condition. Therefore, hydrogen affects both the dislocation glide kinetics and the microstructural evolution in strain-hardened 316L under cyclic straining.

In the annealed CrMnFeCoNi alloy, the hysteresis loops reveal an unusual small yield point in the first cycle (monotonic behavior) at all plastic strain amplitudes. Furthermore, the work hardening rates are very low during the initial cycles. These phenomena are likely associated with the compositional complexity of this alloy and the very low dislocation density after annealing. Calculations of operational activation area reveal that dislocation interactions with the solid-solution matrix and forest dislocations control the rate of cyclic deformation in the CrMnFeCoNi alloy. Although dislocation cell structures are reported to develop during cyclic straining, cross slip is not an operative rate-controlling mechanism. The results demonstrate that, despite the different microstructural evolution under LCF testing, the kinetics of dislocation glide in this alloy

are the same under monotonic and cyclic loading conditions. Furthermore, the compositional complexity does not lead to different rate-controlling obstacles compared to those observed in conventional solution strengthened alloys under similar deformation conditions. Comparing the cyclic behavior of non-charged and H-precharged CrMnFeCoNi, the addition of hydrogen leads to serrated flow during the first cycle, which indicates a hydrogen pinning effect on mobile dislocations that is overcome by an increase in dislocation density with further straining. Cyclic hardening and softening followed by a region of approximately constant peak stresses that extend to the end of life characterize the cyclic stress response in both material conditions. Hydrogen increases the peak stresses by enhancing the effective stresses in this HEA, but it does not affect the evolution of back stresses. Furthermore, severe reduction in crack initiation and total lifetimes are observed in the H-precharged condition. The analysis of fracture surfaces reveals this reduction is due to brittle intergranular failure in H-precharged CrMnFeCoNi, consistent with a reported model of hydrogen-induced strain incompatibility across grain boundaries.

This dissertation work contains the first fundamental studies of dislocation glide processes during cyclic deformation of strain-hardened Type 316L austenitic stainless steel and annealed CrMnFeCoNi alloy using a unique “mechanical microscopy” approach. It is also the first study of the influence of hydrogen on dislocation glide processes in 316L stainless steel. Lastly, it is the first study to show extremely detrimental effects of hydrogen in CrMnFeCoNi during low cycle fatigue. Together, these studies help advance our understanding of the opportunities and limitations of using these materials in fatigue-critical structural and hydrogen energy related applications.

# Acknowledgements

Words cannot express my gratitude to my family, friends, mentors and colleagues for the continuous professional and personal support I have received during these years of graduate school.

I would like to start by thanking my parents Geralda A. L. Oliveira and Jose N. Oliveira for encouraging me to fly high and pursue my dreams. Despite the physical distance, the two of you, as well as Sabrina (sister) and Lucas (brother) have always been present. You all are my inspiration and I hope to make you proud, always!

I feel blessed to have met my fiancé Nicholas Lundgren during my journey at UC Davis. Thanks for lifting me up in hard days and for celebrating happy days with me. You inspire me to work hard and to always try.

I would like to express my deep gratitude to my research advisor, Prof. Jeffery Gibeling. I truly appreciate the opportunity to navigate grad school under your guidance. Thank you for making me "fatigued" and "stressed" with research and for making time to assist me whenever I needed help. You have prepared me to be a great professional, and I am proud to be your student.

I also deeply appreciate all the research feedback I have received from my collaborators at SNLL, Dr. Chris San Marchi and Dr. Doug Medlin, and at ORNL, Dr. Easo George, in addition to my dissertation committee, Prof. Jeffery Gibeling, Prof. Jeremy Mason and Prof. Mike Hill. Your guidance and expertise have enriched my dissertation work. A special thanks to Dr. George Kaschner, who helped me with the experimental setup and inspired me to write more on white boards. Thanks for the insightful research discussions and for your mentorship.

Last but not least, I would like to thank all my lab mates and friends in Davis who helped making this grad school journey less bumpy and more enjoyable: Bill Bania, Bing Yang, Boyi Qu, Christine Smudde, Gianmarco Monfared and Mingwei Zhang. You are all very special to me and I hope to maintain you close for the years to come.

# Table of Contents

# List of Figures

# List of Tables

# Chapter 1. Introduction

The fatigue behavior of metallic materials has been a topic of careful and constant investigation that started almost 200 years ago with the advent of railroad systems. The concept of early failure due to a gradual deterioration of the material's structure during service was introduced by Rankine [1] in an 1843 report regarding a fatal railway accident in France in the previous year. 12 years later, Braithwaite [2] used the term 'fatigue of metals' to describe the fracture resulting from repeated loading conditions that "disturb" the material from its "state of rest". Since then, several studies have been conducted to better understand fatigue behavior and mechanisms of fatigue failure in metallic materials, and a nice summary of the major contributions is provided by Suresh [3].

There are two main approaches commonly used to study different aspects of fatigue damage and lifetime. According to Suresh [4], the *total-life* approach characterizes processes that lead to crack initiation and final failure in uncracked (smooth or notched) solids, and tests can be conducted under stress-control (*high cycle fatigue or HCF*) or strain-control (*low cycle fatigue or LCF*). On the other hand, the *damage-tolerant* approach applies the theory of fracture mechanics to characterize fatigue crack propagation in solids containing crack-like defects (pre-cracked). The current work uses the total-life approach and, more specifically, plastic strain-controlled LCF tests, as a tool to study mechanisms of cyclic deformation in metallic materials.

Plastic strain is the strain component responsible for damage and final failure [4, 5]. The idea of characterizing fatigue lifetime in terms of plastic strain amplitude ($\Delta\varepsilon_p/2$) was first introduced independently by Coffin [6] and Manson [7], which resulted in the well-known Coffin-Manson relationship (Eq. (1.1)):

$$\frac{\Delta\varepsilon_p}{2} = \varepsilon_f'\left(2N_f\right)^c \qquad \text{Eq. (1.1)}$$

where $\varepsilon_f'$ is the fatigue ductility coefficient (approximately the true plastic strain at failure, $\varepsilon_f$, from monotonic tests), $2N_f$ is the number of reversals to failure, and c is the fatigue ductility exponent (-0.5 to -0.7 in most metallic materials) [4]. During cyclic deformation, plastic strain induces microstructural changes that lead to hardening and/or softening, strain localization, crack initiation and propagation, and finally fatigue failure [5]. Therefore, controlling plastic strain during LCF tests represents a more systematic approach than load- and total strain-controlled modes to understand deformation processes, especially when different compositions or different material conditions are being compared. In addition, it allows for a constant plastic strain rate throughout the tests, which is a variable describing the mechanical state of the material [8].

Despite the benefits mentioned above, conducting LCF tests under plastic strain control is very challenging. As illustrated in Fig. 1.1, the stress response in the elastic regime (highlighted) becomes vertical when plotted against plastic strain. Experimentally it means that, in plastic strain control using a servohydraulic testing system, an infinitesimal change in plastic strain can lead to a very large change in stress, enough to cause mechanical instability and a machine shutdown. To overcome this limitation, the control channels must be carefully tuned to operate at the 'edge of instability', i.e., maintain a rapid response with minimum stress oscillations during the reversals while sluggish enough to remain stable [9, 10]. True plastic strain-controlled LCF tests were extensively used by Mughrabi and colleagues [11-20] to study mechanisms of cyclic deformation in both body- and face-centered cubic materials, and remarkable contributions were made towards the fundamental understanding of cyclic stress response and dislocation arrangements in fatigue.

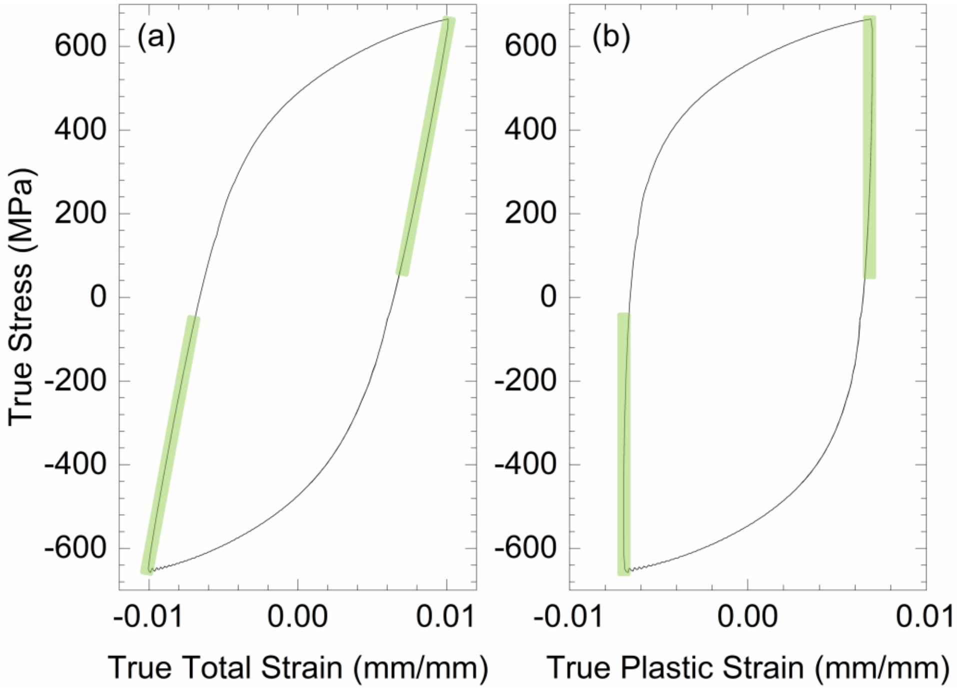

Fig. 1.1: Comparison between (a) true stress vs true total strain and (b) true stress vs true plastic strain behaviors in low cycle fatigue. The highlighted segments represent regions of pure elastic loading.

Although much groundwork has been covered in the field of LCF, there is still the need to re-evaluate the cyclic behavior of commercially available alloys in the context of novel applications, such as in the hydrogen energy industry. The interest in hydrogen as an energy carrier has emerged with the increasing demand for alternative energy solutions in place of traditional carbon-based approaches. This idea is accompanied by a plan to scale up the national hydrogen production and use in transportation, chemical and industrial processes, power generation and hybrid energy systems [21]. One of the most commonly used alloys in hydrogen handling systems is the Type 316L austenitic stainless steel due to its resistance to hydrogen embrittlement [22, 23]. The effect of hydrogen on the fatigue behavior of this alloy has been widely investigated under *load-controlled* HCF tests [24-28], and the focus has been on establishing fatigue performance-based criteria for hydrogen service [29]. However, there is a lack of LCF studies under *total strain* [30] and *plastic strain* control that characterize mechanisms of cyclic deformation and fatigue failure in Type 316L stainless steel in presence of hydrogen.

In addition to understanding the fatigue response of existing materials in novels applications, detailed LCF studies must be conducted in new materials, such as the group of materials known as high entropy alloys, to determine their applicability in energy, transportation, and infrastructure sectors. High entropy alloys represent a new class of metallic materials in which, unlike in conventional alloy design, compositions towards the center of phase diagrams are explored. This alloy design concept was first introduced by Cantor, *et al.* [31] and Yeh, *et al.* [32] in 2004 and, since then, several compositions have been developed and tested. Among them, the equiatomic single-phase FCC CrMnFeCoNi composition, also known as the Cantor alloy, has shown promising mechanical behavior for future structural application, as summarized by George, *et al.* [33], Li, *et al.* [34] and Cantor [35]. However, fundamental understanding of the mechanisms of cyclic deformation and environmental degradation is still necessary before this alloy becomes commercially available.

Despite the valuable information obtained through LCF tests, conventional experiments at a constant plastic strain rate are not able to inform about the dislocation interactions that control the rate of cyclic deformation. For that, transient tests such as (plastic) strain rate change tests must be performed, and the relationship between flow stress and plastic strain rate used to calculate thermal activation parameters that reflect the length scale of dislocations moving through discrete obstacles on the glide plane [36]. Therefore, the goal of this dissertation is to integrate plastic strain-controlled LCF tests and plastic strain rate change experiments to characterize the fundamental mechanisms of cyclic deformation in Type 316L austenitic stainless steel and CrMnFeCoNi high entropy alloy for structural and hydrogen energy applications. The results are separated into four main chapters, described as follows. Chapter 2 is entitled 'The Influence of Hydrogen on the Low Cycle Fatigue Behavior of Strain-Hardened 316L Stainless Steel', and it is collaboration with Chris W. San Marchi and Douglas L. Medlin, from Sandia National Laboratories, Livermore (SNLL). This is a published work that describes the LCF behavior of strain-hardened 316L stainless steel in the non-charged and hydrogen-precharged (H-precharged) conditions. In addition to informing about the evolution of effective and back stresses and the total fatigue lifetime, this chapter introduces a new methodology for estimating fatigue crack initiation lifetime using stress-strain hysteresis loop data. Chapter 3 is entitled "The Kinetics of Dislocation Glide During Low Cycle Fatigue of 316L Stainless Steel Containing Hydrogen", and it is a continuation of the study conducted in Chapter 2 in collaboration with researchers from SNLL. In this chapter, plastic strain rate change experiments are used to calculate thermal activation parameters. Along with scanning transmission electron microscopy (STEM) images, the results reveal the influence of hydrogen on microstructural development and thermally activated dislocation glide during cyclic straining. In Chapter 4, the "Influence of Hydrogen on the Low Cycle Fatigue Behavior of the Equiatomic CrMnFeCoNi High Entropy Alloy" is investigated. This study is a collaboration with Chris W. San Marchi from SNLL and Easo P. George from Oak Ridge National Laboratory (ORNL), and it informs about the changes in LCF response and fatigue failure mode induced by the presence of hydrogen. The study in Chapter 5 is a collaboration with Easo P. George (ORNL) and describes the "The Kinetics of Dislocation Glide During Low Cycle Fatigue of the Equiatomic CrMnFeCoNi High Entropy Alloy". It focuses on identifying the thermal obstacles influencing cyclic deformation in this alloy and whether the rate-controlling mechanisms are different than those found under monotonic loading conditions. Chapter 6 provides an overall summary and insight into future research opportunities and, finally, the Appendices include details on the methodology proposed for estimation of initiation lifetime, in addition to relevant data from LCF and plastic strain rate change experiments.

## References

[1] W. J. M. Rankine. On the causes of the unexpected breakage of the journals of railway axles; and on the means of preventing such accidents by observing the law of continuity in their construction. Minutes of the Proceedings of the Institution of Civil Engineers, *Thomas Telford-ICE Virtual Library*, 1843, pp. 105-107.

[2] F. Braithwaite. On the fatigue and consequent fracture of metals. Minutes of the Proceedings of the Institution of Civil Engineers, *Thomas Telford-ICE Virtual Library*, 1854, pp. 463-467.

[3] S. Suresh. Chapter 1 - Introduction and overview. Fatigue of Materials, *Cambridge university press*, Cambridge, 1998, pp. 1-35.

[4] S. Suresh. Fatigue of Materials. *Cambridge University Press*, Cambridge, 1998.

[5] H. Mughrabi. Cyclic Deformation and Fatigue: Some Current Problems. in: H. J. McQueen, J.-P. Bailon, J. I. Dickson, *et al.* (Eds.) Proceedings 7th International Conference on the Strength of Metals and Alloys, *Pergamon Press*, Oxford, 1986, pp. 1917-1942.

[6] L. F. Coffin, Jr. A study of the effects of cyclic thermal stresses on a ductile metal. *Transactions of the American Society of Mechanical Engineers, New York* 76 (1954) 931-950.

[7] S. S. Manson. Behavior of Materials under Conditions of Thermal Stress. *National Advisory Committee for Aeronautics*, 1954, pp. 1-34.

[8] E. W. Hart. A Phenomenological Theory for Plastic Deformation of Polycrystalline Metals. *Acta Metall.* 18 (6) (1970) 599-610.

[9] H. J. Christ, H. Mughrabi, S. Kraft, *et al.* The Use of Plastic Strain Control in Thermomechanical Fatigue Testing. in: B. J., R. L., S. M., *et al.* (Eds.), Fatigue under Thermal and Mechanical Loading: Mechanisms, Mechanics and Modelling, *Springer*, 1996, pp. 1-14.

[10] G. C. Kaschner, J. C. Gibeling. A study of the mechanisms of cyclic deformation in f.c.c. metals using strain rate change tests. *Mater. Sci. Eng., A* 336 (1-2) (2002) 170-176.

[11] H. Mughrabi. The cyclic hardening and saturation behaviour of copper single crystals. *Mater. Sci. Eng.* 33 (2) (1978) 207-223.

[12] H. Mughrabi. Cyclic Deformation and Fatigue Fracture of Alpha-Iron Polycrystals. *Z Metallkd* 66 (12) (1975) 719-724.

[13] H. Mughrabi, C. Wuthrich. Asymmetry of Slip and Shape Changes during Cyclic Deformation of Alpha-Iron Single-Crystals. *Philos Mag* 33 (6) (1976) 963-984.

[14] H. Mughrabi, K. Herz, X. Stark. Effect of Strain-Rate on Cyclic Deformation Properties of Alpha-Iron Single-Crystals. *Acta Metall.* 24 (7) (1976) 659-668.

[15] H. Mughrabi, K. Herz, X. Stark. Cyclic Deformation and Fatigue Behavior of Alpha-Iron Monocrystals and Polycrystals. *Int J Fracture* 17 (2) (1981) 193-220.

[16] F. Ackermann, H. Mughrabi, A. Seeger. Temperature-Rate and Strain-Rate Dependence of the Flow-Stress of Ultrapure Niobium Single-Crystals in Cyclic Deformation. *Acta Metall.* 31 (9) (1983) 1353-1366.

[17] C. Sommer, H. Mughrabi, D. Lochner. Influence of temperature and carbon content on the cyclic deformation and fatigue behaviour alpha-iron. Part I. Cyclic deformation and stress-behaviour. *Acta Mater* 46 (5) (1998) 1527-1536.

[18] R. Zauter, H. J. Christ, H. Mughrabi. Some Aspects of Thermomechanical Fatigue of AISI 304L Stainless Steel: Part I. Creep-Fatigue Damage. *Metall Mater Trans A* 25 (2) (1994) 401-406.

[19] R. Zauter, H. J. Christ, H. Mughrabi. Some Aspects of Thermomechanical Fatigue of AISI 304L Stainless Steel: Part 2. Dislocation Arrangements. *Metall Mater Trans A* 25 (2) (1994) 407-413.

[20] H. J. Christ, H. Mughrabi. Cyclic Stress-Strain Response and Microstructure under Variable Amplitude Loading. *Fatigue Fract Eng M* 19 (2-3) (1996) 335-348.

[21] Department of Energy Hydrogen Program Plan. in: DOE (Ed.) 2020.

[22] C. San Marchi, B. P. Somerday. Comparison of stainless steels for high-pressure hydrogen service. Pressure Vessels and Piping Conference, *American Society of Mechanical Engineers*, 2014, p. V06BT06A023.

[23] C. San Marchi, J. A. Zimmerman, X. Tang, *et al.* Fatigue Life of Austenitic Stainless Steel in Hydrogen Environments. ASME 2015 Pressure Vessels and Piping Conference, Boston, Massachusetts, USA, 2015.

[24] P. J. Gibbs, K. A. Nibur, C. San Marchi. Plastic Ratcheting and Fatigue Crack Formation in Austenitic Steels with Hydrogen. in: B. P. Somerday, P. Sofronis (Eds.), International Hydrogen Conference (IHC 2016): Materials Performance in Hydrogen Environments, *ASME Press*, 2017, pp. 306-315.

[25] K. E. Nygren, A. Nagao, P. Sofronis, *et al.* The Role of Microstructure in Hydrogen-Induced Fatigue Failure of 304 Austenitic Stainless Steel. *Metall. Mater. Trans. A* 51 (11) (2020) 5704-5714.

[26] K. E. Nygren, A. Nagao, S. Wang, *et al.* Influence of internal hydrogen content on the evolved microstructure beneath fatigue striations in 316L austenitic stainless steel. *Acta Mater* 213 (2021).

[27] T. Iijima, H. Enoki, J. Yamabe, *et al.* Effect of High Pressure Gaseous Hydrogen on Fatigue Properties of SUS304 and SUS316 Austenitic Stainless Steel. ASME 2018 Pressure Vessels and Piping Conference, 2018.

[28] P. J. Gibbs, C. San Marchi, K. A. Nibur, *et al.* Comparison of Internal and External Hydrogen on Fatigue-Life of Austenitic Stainless Steels. ASME 2016 Pressure Vessels and Piping Conference, Vancouver, British Columbia, Canada, 2016, pp. 1-8.

[29] C. San Marchi, J. Yamabe, M. Schwarz, *et al.* Global Harmonization of Fatigue Life Testing in Gaseous Hydrogen. ASME 2018 Pressure Vessels and Piping Conference, *American Society of Mechanical Engineers Digital Collection*, 2018.

[30] T. T. Nguyen, J. Park, S. H. Nahm, *et al.* Ductility and fatigue properties of low nickel content type 316L austenitic stainless steel after gaseous thermal pre-charging with hydrogen. *Int. J. Hydrogen Energy* 44 (51) (2019) 28031-28043.

[31] B. Cantor, I. T. H. Chang, P. Knight, *et al.* Microstructural development in equiatomic multicomponent alloys. *Mater. Sci. Eng., A* 375-377 (2004) 213-218.

[32] J. W. Yeh, S. K. Chen, S. J. Lin, *et al.* Nanostructured high-entropy alloys with multiple principal elements: Novel alloy design concepts and outcomes. *Adv. Eng. Mater.* 6 (5) (2004) 299-303.

[33] E. P. George, W. A. Curtin, C. C. Tasan. High entropy alloys: A focused review of mechanical properties and deformation mechanisms. *Acta Mater.* 188 (2020) 435-474.

[34] Z. Z. Li, S. T. Zhao, R. O. Ritchie, *et al.* Mechanical properties of high-entropy alloys with emphasis on face-centered cubic alloys. *Prog. Mater Sci.* 102 (2019) 296-345.

[35] B. Cantor. Multicomponent high-entropy Cantor alloys. *Prog. Mater Sci.* 120 (2021).

[36] U. F. Kocks, A. S. Argon, M. F. Ashby. Thermodynamics and Kinetics of Slip. *Prog. Mater Sci.* 19 (1975) 1-281.

# Chapter 2. The Influence of Hydrogen on the Low Cycle Fatigue Behavior of Strain-Hardened 316L Stainless Steel[1]

## Abstract

The present study focuses on the low cycle fatigue (LCF) behavior of strain-hardened 316L stainless steel under plastic strain control, aiming to understand the influence of internal hydrogen on fatigue performance and cyclic deformation behavior for energy-related technologies. The strain-hardened 316L specimens tested at plastic strain amplitudes between 0.1% and 0.7% with and without hydrogen displayed continuous cyclic softening. Internal hydrogen increases the cyclic strength of this steel, with a greater difference in strength at low plastic strain amplitudes. A Bauschinger analysis revealed that effective stresses represent the major contribution to the flow stress for all material conditions and amplitudes. At low plastic strain amplitudes, effective stresses are responsible for differences in cyclic strength between hydrogen-precharged and non-charged specimens. In contrast, back stresses become more significant at high amplitudes, and more similar deformation structures are observed. Although internal hydrogen reduced the total LCF lifetime at all amplitudes, this degradation is more significant in the low amplitude regime. This result is attributed to high effective stresses that lead to the onset of multiple slip at lower cumulative plastic strains in the hydrogen-precharged condition compared to the non-charged condition at low amplitudes. In addition, the evolution of the apparent elastic response of the material suggests that the primary crack(s) nucleates at a smaller percentage of the total lifetime and propagated in fewer number of cycles in the hydrogen-precharged than in the non-charged condition. Fracture surface and gage section observations revealed a transgranular crack path and planar slip traces in both

---

[1] Published as D. M. Oliveira, C. W. San Marchi, D. L. Medlin, and J. C. Gibeling. *Mater. Sci. Eng., A* (2022): 143477.

material conditions, with internal hydrogen promoting multiple slip at lower values of cumulative plastic strain than in the non-charged condition.

**Keywords**: Low Cycle Fatigue, Plastic Strain Control, Hydrogen, Bauschinger Stresses, Multiple Slip

## 2.1. Introduction

The growing demand for alternative energy solutions has motivated consideration of hydrogen technologies in place of traditional carbon-based approaches, for example in fuel cell electrical vehicles, heating, steel making and chemical reduction processes, as well as for energy storage (i.e., use of renewable energy to generate hydrogen) [1-3]. Although hydrogen fuel cell vehicles are already commercially available, further advancements in material selection and component design require a fundamental understanding of mechanical performance in the presence of high-pressure gaseous hydrogen. The fatigue behavior of materials used in hydrogen storage and distribution systems is particularly important since components are often exposed to dynamic loading conditions, where the absorbed hydrogen may affect the deformation mechanisms and shorten service life.

In previous work on this topic, Gibbs, *et al.* [4] investigated the effect of internal hydrogen on the high cycle fatigue (HCF) behavior of 316L austenitic stainless steel. Results from load-controlled tension-tension tests of smooth specimens demonstrated that hydrogen has a detrimental effect on fatigue life and slightly enhances the accumulation of plastic deformation at a given number of cycles when testing is performed at similar stress levels relative to the yield strength. Similar hydrogen-induced degradation in fatigue performance has been reported in several (load-controlled) HCF studies of austenitic stainless steels, examples of which include the work of Kuromoto, *et al.* [5], Nygren, *et al.* [6, 7], Iijima, *et al.* [8] and Gibbs, *et al.* [9]. According to Gibbs, *et al.* [4], the main contributions of hydrogen to the fatigue behavior of 316L steel are to increase the yield strength and to change the deformation character. Although a significant research effort has been devoted to investigating the interactions between hydrogen and the dynamic microstructure [6, 7, 10-13], no unified understanding has been accepted. Additionally, the higher strength of material containing hydrogen means that in load-controlled tests the imposed plastic strains differ between the specimens with and without hydrogen when they are tested at the same load amplitude. However, fatigue crack initiation processes are well-known to be controlled by plastic strain [14-17]. Thus, *load-controlled* high cycle fatigue tests may not enable an appropriate comparison of mechanisms between materials with and without internal hydrogen. This matter is further complicated by the fact that hydrogen usually leads to changes in ductility [4, 9, 18, 19].

To avoid these concerns regarding high cycle fatigue testing, *strain-controlled* low cycle fatigue (LCF) tests represent a meaningful method of identifying the mechanisms of hydrogen-assisted fatigue. This approach emphasizes the deformation component that induces fatigue damage and crack initiation. It is also a more realistic representation of the behavior near crack tips and defects in the material, where local stresses often exceed the yield strength [20]. One of the few total strain-controlled fatigue studies of austenitic steels available in the literature was conducted by Nguyen, *et al*. [21] on a low nickel content hydrogen-precharged (H-precharged) 316L stainless steel. It was observed that internal hydrogen significantly reduced the fatigue life, especially at high total strain amplitudes. Post-fracture characterization using electron backscatter diffraction (EBSD) revealed strain-induced martensitic transformation at the grain boundaries for both material conditions. According to the authors, hydrogen diffuses through the phase transformation zone and accumulates at the crack tip, resulting in the nucleation of microcracks, continuous crack tip sharpening and enhancement of crack propagation. Nguyen, *et al*. concluded that both processes of microcrack initiation and crack growth were responsible for the degradation of the LCF life in their H-precharged 316L stainless steel with low nickel content [21], although this observation may depend on the rate of cycling.

Due to the limitations noted above for *load-controlled* HCF and the limited data for *strain-controlled* LCF of hydrogen-containing austenitic stainless steels, the present study uses *plastic strain-controlle*d LCF tests to reveal new insights into the mechanism(s) of hydrogen-assisted fatigue. Unlike other testing modes, this approach allows for a direct evaluation of the plastic component of cyclic deformation under a constant plastic strain rate although the frequency differs for each amplitude. By keeping the plastic strain rate constant, known rate effects on hydrogen-assisted fatigue and fracture [22-26] are controlled for. This is an important distinction of the results presented here compared to conventional strain- and load-controlled tests, where the plastic strain rate can differ by an order of magnitude (or more) between different stress/strain amplitudes representing the low cycle and high cycle regimes. Furthermore, these other testing modes represent different deformation constraint conditions and different fatigue life dependences on strength and ductility [14].

## 2.2. Materials and Methods

The strain-hardened 316L austenitic stainless steel tested in the current study was commercially obtained as a 14.3 mm diameter round bar with the mill composition given in Table 2.1. Low cycle fatigue specimens were machined to the geometry shown in Fig. 2.1. The gage surfaces were mechanically polished with SiC paper and diamond polishing compounds down to 0.25 micron, followed by ultrasonic cleaning in deionized water to remove debris from the surface.

Table 2.1: Chemical composition (wt%) of 316L stainless steel specimens [4].

| **Ni** | **Cr** | **Mo** | **Mn** | **Si** | **Cu** | **C** | **N** | **Co** | **S** | **P** | **Fe** |
|---|---|---|---|---|---|---|---|---|---|---|---|
| 12.10 | 17.62 | 2.06 | 1.31 | 0.57 | 0.30 | 0.021 | 0.04 | 0.33 | 0.025 | 0.024 | Bal. |

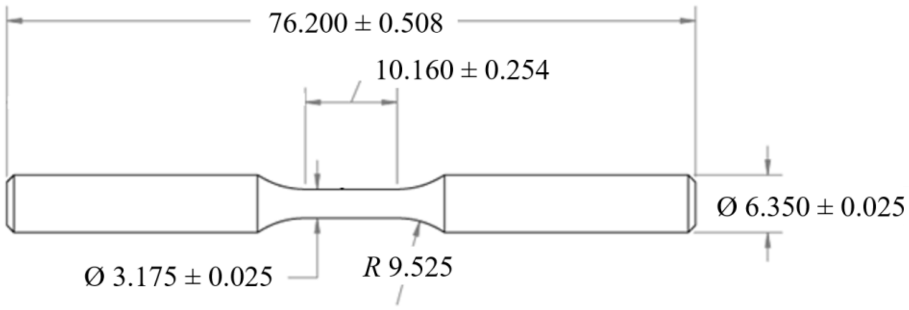

Fig. 2.1: LCF specimen geometry and dimensions. All values are in mm.

The tested conditions were as-received (AR), H-precharged (PC) and heat-treated (HT). The 316L specimens in the AR condition had no intentional addition of hydrogen. The PC specimens were thermally charged in an autoclave with hydrogen gas pressure of 138 MPa at temperature of 573 K for approximately 13 days, which is sufficient time to saturate the specimen [27]. The concentration of hydrogen in the grip section of a PC specimen was measured by inert gas fusion-infrared absorbance at the conclusion of a fatigue testing and found to be 155 wt. ppm (parts per million by weight). This hydrogen concentration is typical for these materials and precharging conditions [27]. To confirm that the thermal exposure required for the precharging process was not itself influencing the LCF lifetime, control specimens (HT) were also prepared. These specimens were subjected to the same thermal exposure as for the precharging conditions, but in air rather than hydrogen. No signs of oxidation were visually detected on the surface of the HT specimens.

Low cycle fatigue tests were conducted in true plastic strain control in an MTS servo-hydraulic testing system equipped with a load cell and an extensometer. The alignment of the load frame was verified using a strain-gaged standard round specimen. The test command was controlled by MTS TestStar and Testware-SX running software procedures adapted from Walley, *et al.* [28]. The experiments were performed at room temperature in a fully reversed mode (ratio of minimum to maximum plastic strain R = -1), using a constant plastic strain rate ($\dot{\varepsilon}_p$) of $1x10^{-3}$ $s^{-1}$ and plastic strain amplitudes ($\Delta\varepsilon_p/2$) between 0.1 and 0.7%.

True plastic strain, $\varepsilon_p$, is a computed variable determined from the measured load $L$ and total engineering strain, $e_t$. The true elastic strain is calculated from the ratio of the true stress to the elastic modulus $E$ and subtracted from the true total strain to evaluate $\varepsilon_p$, as shown in Eq. (2.1):

$$\varepsilon_p = \ln(1 + e_t) - (1 + e_t) \times \frac{L}{A_0 E} \qquad \text{Eq. (2.1)}$$

In this calculation, $A_0$ is the initial cross-sectional area. The elastic modulus $E$ was initially obtained from strain-controlled tensile tests, conducted at a total strain rate of $2x10^{-4}$ $s^{-1}$. Then, the modulus was adjusted by an iterative process of running approximately 10 LCF cycles and manually re-calculating the modulus from the first stress-plastic strain hysteresis loop so that the loading and unloading portions were nearly vertical.

The failure criterion for this study was defined as the cycle at which the magnitude of the tension peak stress is 20% less than the magnitude of the compression peak stress; this difference in stress is associated with the formation of cracks that open in tension. Tests were terminated when this condition was reached, usually prior to rupture of the specimen. After failure, scanning electron (SEM) and confocal microscopes were used to characterize the microscopic features that evolved on the polished surface of the gage section due to the imposed cycle deformation. The instruments used were a Thermo Fisher Quattro S SEM operating at an accelerating voltage of 5-15 kV in the secondary electron imaging mode, and a Zeiss Axio CSM 700 confocal microscope. Fatigue fracture surfaces were then exposed by pulling the tested specimens in tension at a high loading rate and observed using the same SEM instrument and operating parameters. Additional interrupted LCF tests were conducted at amplitudes of 0.3 and 0.8% for scanning transmission electron microscopy (STEM) examination of dislocation arrangements with and without hydrogen. Images were acquired using a Thermo Fisher Themis Z instrument operating at 300 kV using a bright-field STEM detector with a beam convergence of 3.0 mrad. The specimens for transmission electron microscopy were cut perpendicular to the loading axis from the gage section of the fatigue specimens. The slices were mechanically thinned and polished to approximately 120 μm thickness, finishing with SiC polishing paper (p4000). Final specimen thinning to electron transparency was conducted in a Struers TenuPol-5 electropolishing system using a solution of 90 vol. % ethanol and 10 vol. % perchloric acid and operated at 24.6 V and a temperature of -10±0.4°C. The measured polishing currents varied by specimen and over the course of the electropolishing but were typically in the range of 52 – 84 mA.

To further understand the connection between the mechanical response and the deforming microstructure, effective ($\sigma_e$) and back ($\sigma_b$) stresses were calculated from the evolving hysteresis loops using the Bauschinger analysis expressed in Eq. (2.2) [29, 30]:

$$\sigma_e = \frac{\sigma_{max} - \sigma_o}{2} \; ; \; \sigma_b = \frac{\sigma_o - \sigma_{min}}{2} \qquad \text{Eq. (2.2)}$$

where $\sigma_o$ is the reverse yield stress, taken at a true plastic strain offset of 0.1% [31, 32], and $\sigma_{max}$ and $\sigma_{min}$ represent the maximum and minimum peak stresses in each hysteresis loop, respectively. Effective stress represents the component of the flow stress associated with the motion of dislocations through a field of short-range obstacles, such as solute atoms and dislocation forests. On the other hand, back stresses originate from interactions between dislocations and long-range obstacles, such as grain boundaries, deformation twins and dislocation cell walls [31-34].

In addition, the initiation lifetime was estimated from the analysis of the apparent elastic response of the material. The collected load and total strain data were used to compute the slopes of the tensile elastic unloading portions of the true stress-total strain hysteresis loops through linear least squares regression. Then, the plot of the unloading slope as a function of the cycle number was smoothed and fitted with an exponential decay equation to determine the number of cycles necessary to produce a 1% decrease in unloading slope, defined here as the fatigue crack initiation lifetime. Additional details of the new methodology used for this slope analysis are included in the Appendix A.1.

## 2.3. Results

### *2.3.1. Hysteresis Loops*

The hysteresis loops record the variations of cyclic true stress as a function of the applied true plastic strain and provide information about the plastic work for each cycle and the changes in flow stress with cycling. Fig. 2.2 shows representative hysteresis loops for AR and PC 316L specimens tested at a plastic strain amplitude of 0.7%. The loops are symmetric along the plastic strain axis, and the elastic unloading segments after tension and compression are nearly vertical and parallel to each other. These loop shapes are typical for plastic strain-controlled tests in which the correct elastic modulus is used for the calculations of elastic strains and non-linear elasticity effects are absent [35-38]. The hysteresis loops in Fig. 2.2 also show that both AR and PC conditions softened with increasing number of cycles, and this observation extends to all tested amplitudes.

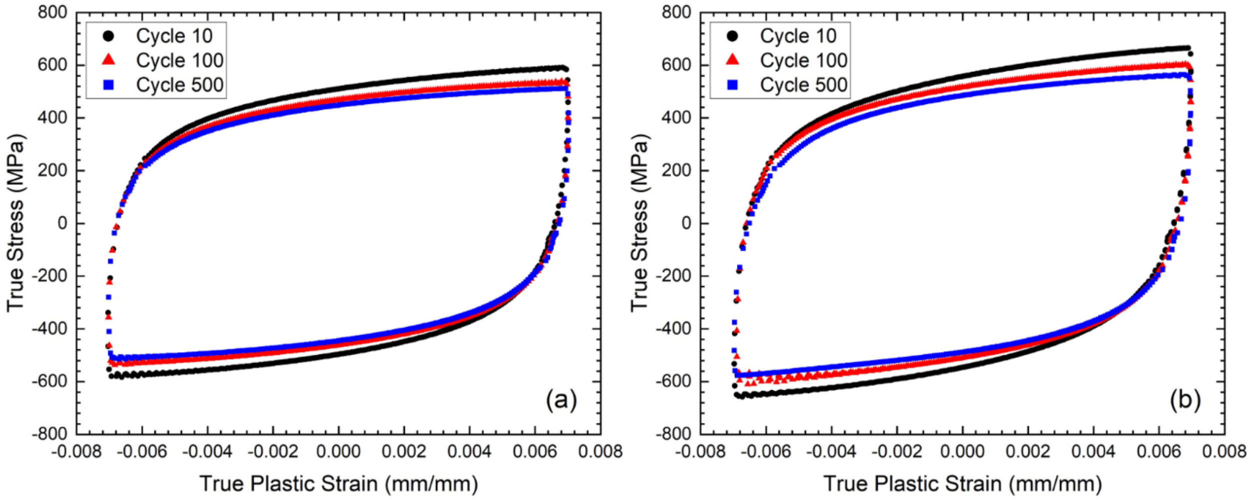

Fig. 2.2: Hysteresis loops for (a) AR and (b) PC 316L stainless steel specimens tested at $\Delta\varepsilon_p/2$ = 0.7%. The black (circle), red (triangle) and blue (square) loops show the stress-strain response for cycles number 10, 100 and 500, respectively.

### *2.3.2. Cyclic Stress Response Curves and Bauschinger Analysis*

The cyclic stress response curves shown in Fig. 2.3 represent the evolution of tension and compression peak stresses with cycling for the AR, PC and HT conditions at 0.2 and 0.7% plastic strain levels. None of the tested specimens reached cyclic stress saturation. Instead, there was rapid initial softening followed by a region of reduced and nearly constant rate of softening, which represents the majority of the LCF lifetime. Tension and compression peak stresses have similar magnitudes throughout the test. Near the end of life, tension and compression stresses diverge, which is due to the differences in load carrying capacity and effective cross-sectional area of the cracked surfaces under tension and compression.

Fig. 2.3 clearly shows the strengthening effect of H-precharging, consistent with previous studies of the response of austenitic stainless steels in tension and high cycle fatigue [4, 9, 21, 39-43]. The increase in strength is also confirmed by the (engineering) 0.2% offset yield strength from the first quarter cycle of fatigue specimens tested at 0.7% plastic strain amplitude. The obtained values of yield strength for the AR and PC conditions are 587 MPa and 666 MPa, respectively.

The PC specimens also exhibit a shorter fatigue life compared to the non-charged AR and HT conditions at the same plastic strain amplitude. At low amplitudes (Fig. 2.3 (a)), AR and HT specimens exhibit similar LCF lifetimes, and hydrogen decreases the total life by a factor of 3. At high amplitudes (Fig. 2.3 (b)), the fatigue life is decreased by a factor of 1.5 when internal hydrogen is added. Although the heat treatment appears to positively affect the LCF resistance at a plastic strain amplitude of 0.7%, that was not true at 0.2% nor was it true at 0.4% (results not shown). Only one HT test was performed at each amplitude, so further interpretation of this result would not be statistically significant. However, these observations confirm that the reduced lifetime in the PC specimens is due to hydrogen and not to the thermal conditions required to hydrogen-charge the material.

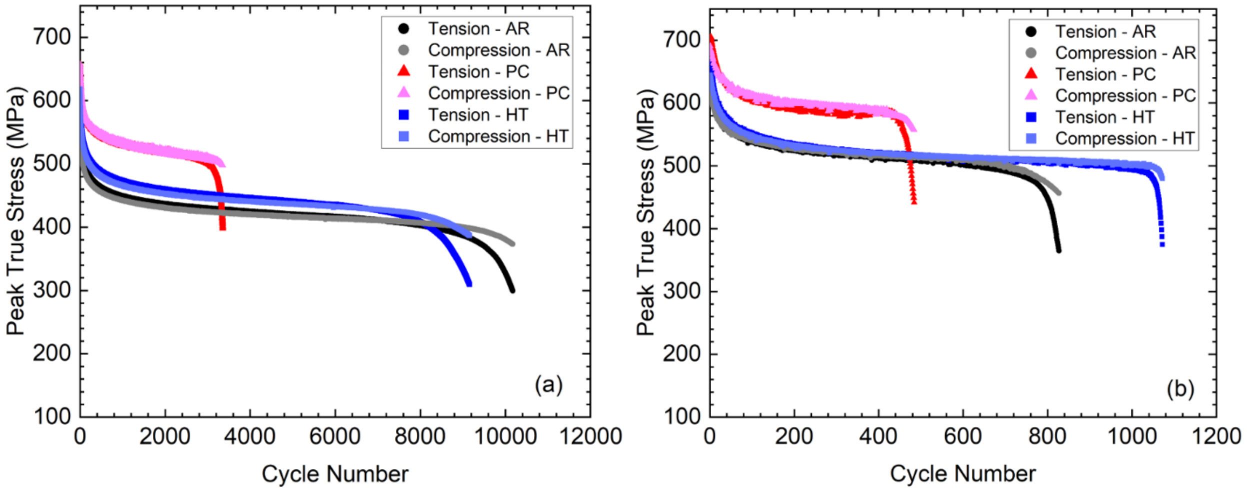

Fig. 2.3: Cyclic stress response curves for AR (black circle), PC (red triangle) and HT (blue square) conditions tested at $\Delta\varepsilon_p/2$ of (a) 0.2% and (b) 0.7%.

Fig. 2.4 shows the peak (total) tension stresses as well as effective and back stresses plotted as a function of applied cumulative plastic strain for AR and PC conditions at (a) 0.2% and (b) 0.7%

plastic strain amplitudes. For all amplitudes and conditions, the effective stresses were the predominant component of the peak stresses. At low amplitude (Fig. 2.4 (a)), the back stresses display similar magnitude for both conditions, thus the difference in cyclic strength between AR and PC is attributed to the influence of internal hydrogen on the effective stresses. At high plastic strain amplitude (Fig. 2.4 (b)), the contribution of back stresses to the total stresses becomes more significant for both conditions. The higher cyclic strength observed in the PC condition for plastic strain amplitude of 0.7% compared to 0.2% appears to be related to greater back stresses, since the effective stresses show relatively little change compared to the lower strain amplitude. Additionally, differences in strength between PC and AR conditions at high strain amplitudes are due in equal measure to differences in effective and back stresses (unlike the case at low amplitudes), suggesting that these conditions have more similar behavior in this amplitude regime.

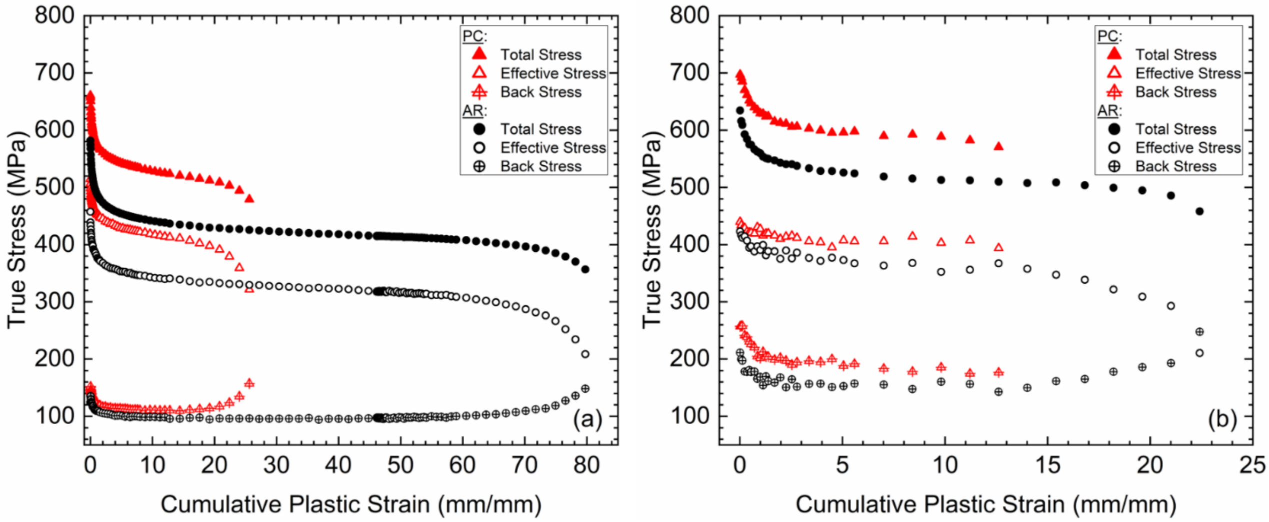

Fig. 2.4: Contributions to the peak tension flow stress for AR (black circle) and PC (red triangle) conditions tested at $\Delta\varepsilon_p/2$ of (a) 0.2% and (b) 0.7%. Effective stresses and back stresses are represented by open and crossed symbols, respectively.

### *2.3.3. Cyclic Stress-Strain Curves*

Since the materials did not reach saturation under the current fatigue testing conditions, the stresses at half-life were considered as a basis for comparing the cyclic strength. The individual symbols in Fig. 2.5 represent the peak tension stress at half-life as a function of the plastic strain amplitude for the AR, PC and HT conditions, and the dashed lines indicate the fit to the standard cyclic form of the Hollomon relationship [44], which is an empirical representation of strain hardening in polycrystalline materials. These cyclic hardening curves are essentially parallel for the AR and PC conditions, and the HT data points fall within the range for the AR behavior. The cyclic data also reinforce the results shown in Fig. 2.3 regarding the strengthening effect of internal hydrogen at all plastic strain amplitudes.

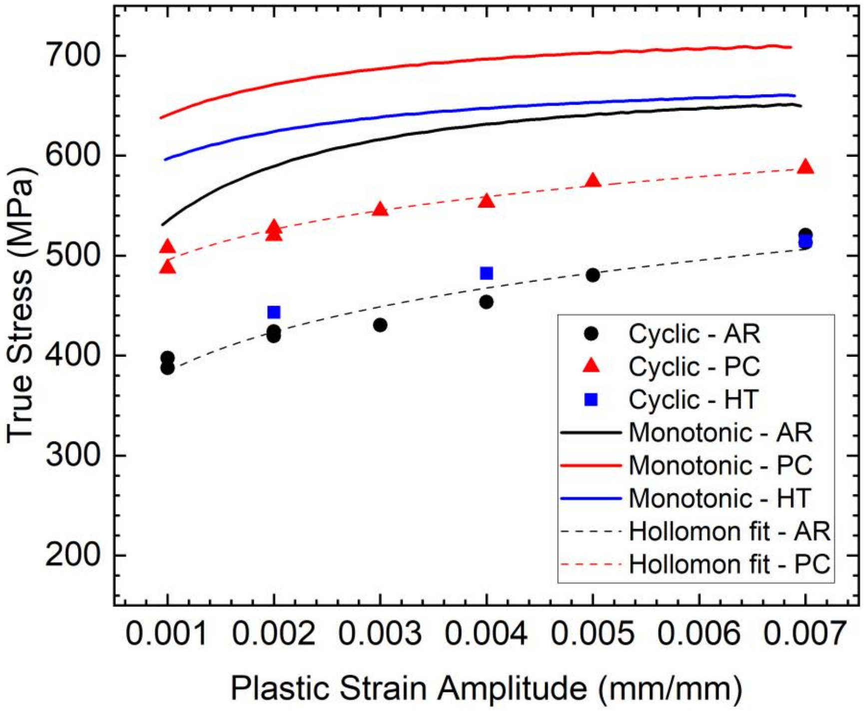

Fig. 2.5: Cyclic Stress-Strain Curves for the AR and PC 316L stainless steel specimens. Individual symbols show the cyclic half-life data, while solid and dashed lines represent monotonic data and fit of the cyclic data to the Hollomon power law, respectively.

The solid lines in Fig. 2.5 represent the monotonic stress-strain behavior for each condition, obtained from the first quarter cycle of the largest tested amplitude (0.7%). A comparison between monotonic and cyclic curves for each material condition confirms that cyclic softening occurs at all tested amplitudes.

### *2.3.4. Strain-life Behavior*

The strain-life plot containing the initiation and total fatigue life data for AR and PC 316L stainless steel is shown in Fig. 2.6; the dashed lines represent a power law fit described in the form of the standard Coffin-Manson equation [45, 46]. The focus of this plot is a comparison of the PC and AR data; HT data were not included here since the stress response curves in Fig. 2.3 suggested that the heat treatment does not alter the behavior of this condition compared to the as-received condition.

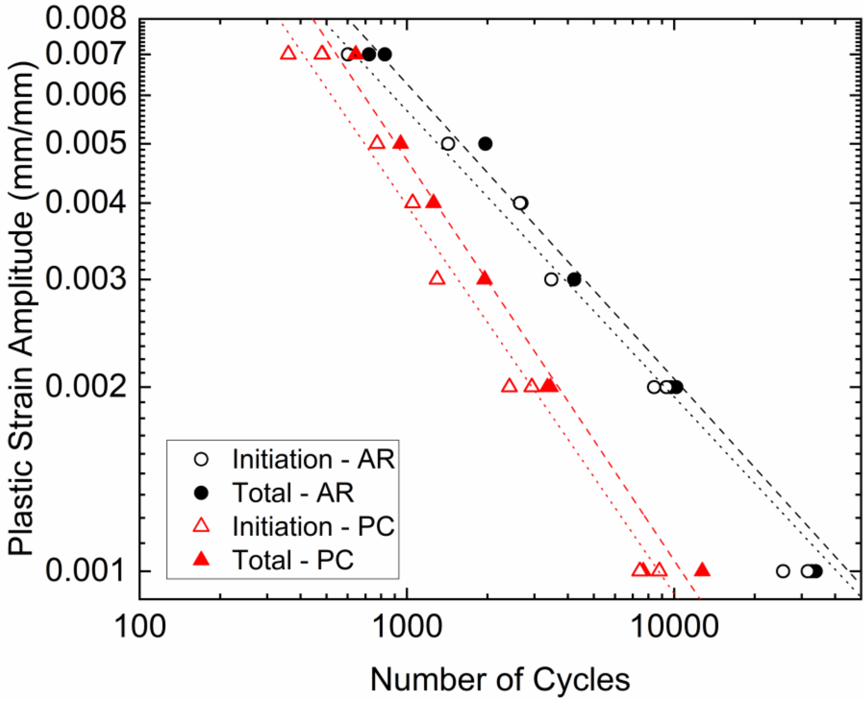

Fig. 2.6: Strain-life plot for 316L stainless steel comprising initiation (open symbols, dotted fitting line) and final (closed symbols, dashed fitting line) fatigue lives.

Fig. 2.6 reveals that fatigue crack initiation encompasses most of the fatigue life for both material conditions at all imposed plastic strain amplitudes. The power law fit parameters from Fig. 2.6 were used to estimate the fraction of the total fatigue life spent in crack initiation for each condition; those values were, on average across all amplitudes, 85% for the AR condition and 78% for the PC condition. Whereas internal hydrogen has only a modest effect on the fraction of the total life required to initiate a crack, the absolute number of cycles can be strongly influenced by internal hydrogen. At 0.1% plastic strain amplitude, the primary crack initiated at approximately 3.5 times fewer cycles in the PC than in the AR condition; this factor decreased to 1.2 at the 0.7% plastic strain amplitude. Fig. 2.6 also indicates that hydrogen degraded the total LCF life at all plastic strain amplitudes in this study, consistent with observations from the stress response curves, but the extent depends on the amplitude. As previously noted and unlike other reported results [21], the difference in number of cycles to failure between AR and PC conditions is larger at low plastic strain amplitudes, meaning that the presence of internal hydrogen causes a greater relative reduction on initiation and total life at low plastic strain amplitudes than at high plastic strain amplitudes. In addition, the Coffin-Manson slopes for initiation and total lives are similar for each tested condition, with a nearly constant offset between these fits, implying that initiation and relatively short crack growth are controlled by the same mechanism.

These clear changes in LCF lifetime in 316L steel induced by the presence of hydrogen suggest that there might be distinctively different slip and fracture morphology behaviors. Thus, microstructural observations of surface slip marks and fracture surfaces were conducted, and the results are presented in the sections below.

### *2.3.5. Surface Slip Markings*

SEM images of the AR and PC gage sections at a similar extent of applied cumulative plastic strain and at low plastic strain amplitudes are shown in Fig. 2.7. For the AR condition, the gage surface was imaged after a test at 0.3% amplitude interrupted at half-life, equivalent to an approximate cumulative plastic strain of 25.4. For the PC condition, areas were probed around the primary crack after testing at 0.2% plastic strain amplitude, or 27.2 cumulative plastic strain. Fig. 2.7 indicates fine planar slip lines for both conditions, with no detectable differences in slip step spacing. Although regions of multiple intersecting dislocation slip were present in both AR and PC surfaces, a higher density of these features was observed in the latter condition. In addition, microcracks along slip bands were detected in both material conditions.

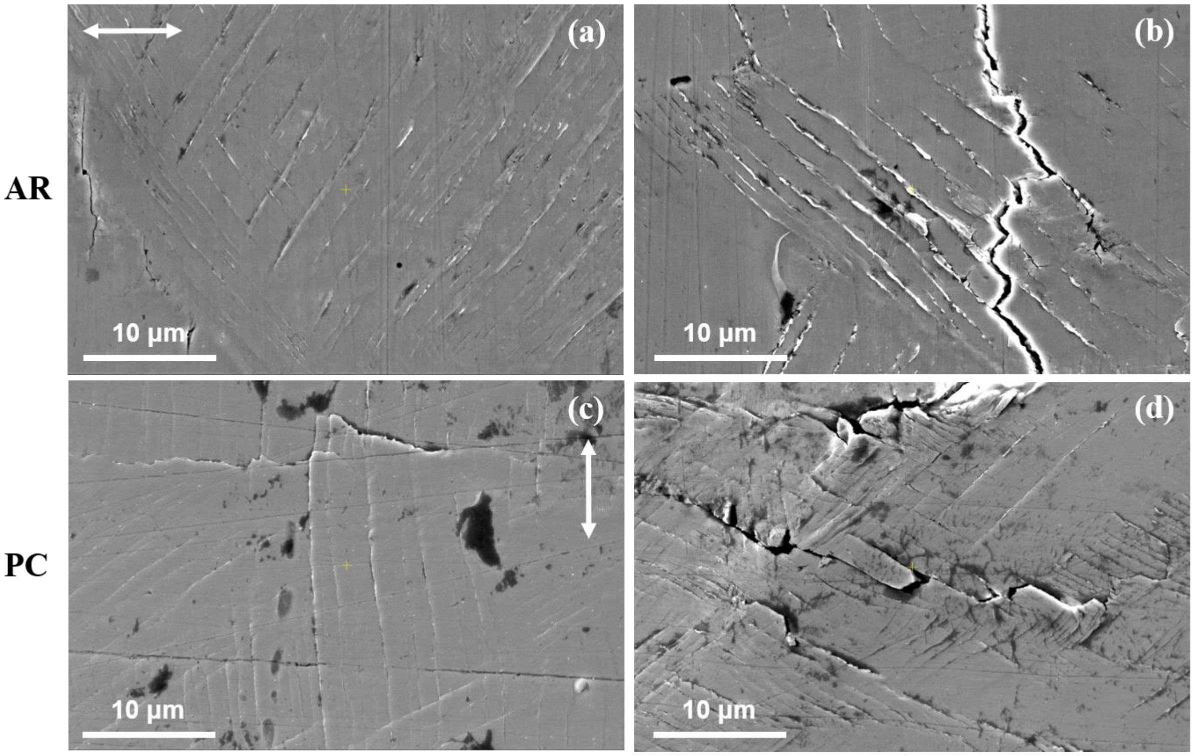

Fig. 2.7: SEM images taken at different locations around the gage section of AR and PC 316L specimens at a similar magnitude of cumulative plastic strain and at low plastic strain amplitudes. (a, b) AR tested at $\Delta\varepsilon_p/2 = 0.3\%$ up to half-life. (c, d) PC after failure at $\Delta\varepsilon_p/2 = 0.2\%$. The white arrows in (a) and (c) indicate the straining direction for AR and PC, respectively.

Fig. 2.8 shows the SEM images of the gage surfaces near the primary crack after testing (a, b) AR and (c, d) PC specimens tested at 0.7% plastic strain amplitude. The difference in cumulative plastic strain between AR and PC at this amplitude is approximately 27%. The image indicates a high density of slip traces and extensive multiple dislocation slip around the crack for both material conditions, as expected from the larger applied plastic strain amplitude (0.7%). Microcracks are observed along slip lines in Fig. 2.8 (a) and (d), and the primary crack is coincident with the planes of intense slip activity in both AR and PC conditions. Away from the primary crack, the SEM observations of the slip traces showed no obvious differences in their distribution and arrangement when comparing AR and PC at this plastic strain amplitude.

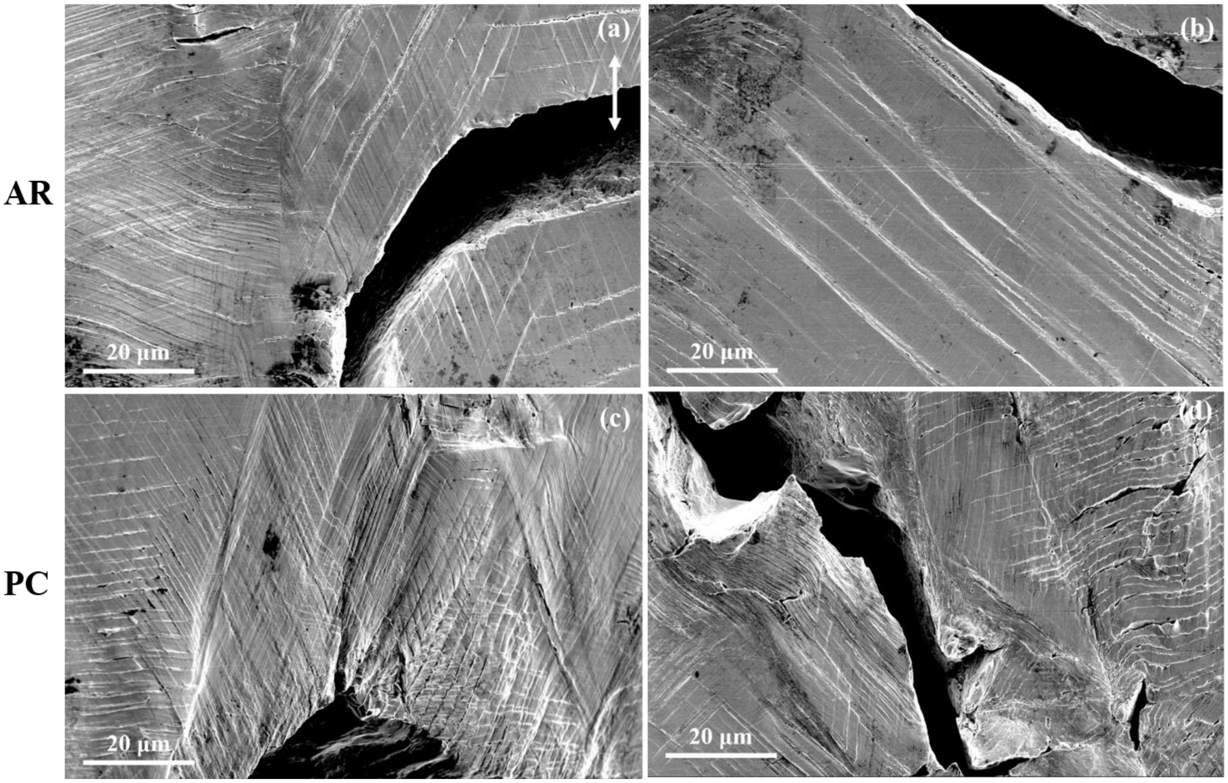

Fig. 2.8: SEM images taken at different locations around the primary crack in (a, b) AR and (c, d) PC 316L stainless steel specimens after failure at $\Delta\varepsilon_p/2 = 0.7\%$. The white arrow in (a) indicates the straining direction for all specimens.

The extent of plastic deformation on a larger scale was evaluated with confocal microscopy as shown in Fig. 2.9 representing approximately 80% of the gage length. At 0.2% plastic strain amplitude (Fig. 2.9 (a) and (b)), there are no visible differences in density and distribution of slip traces along the gage length between the AR and PC conditions at the end of the test. At 0.7% plastic strain amplitude (Fig. 2.9 (c) and (d)), a second macroscopic crack that nucleated at the indentation from one of the extensometer knife edges in the PC specimen can be observed on the left side of Fig. 2.9 (d). There is a similar density of slip traces around the crack for both conditions in Fig. 2.9 (c) and (d), but lower density of slip traces away from the crack in the PC than in the AR condition, even though their applied cumulative plastic strains were relatively similar at this high amplitude. That is, the slip activity appears to be more concentrated in the PC condition when tested at high amplitudes.

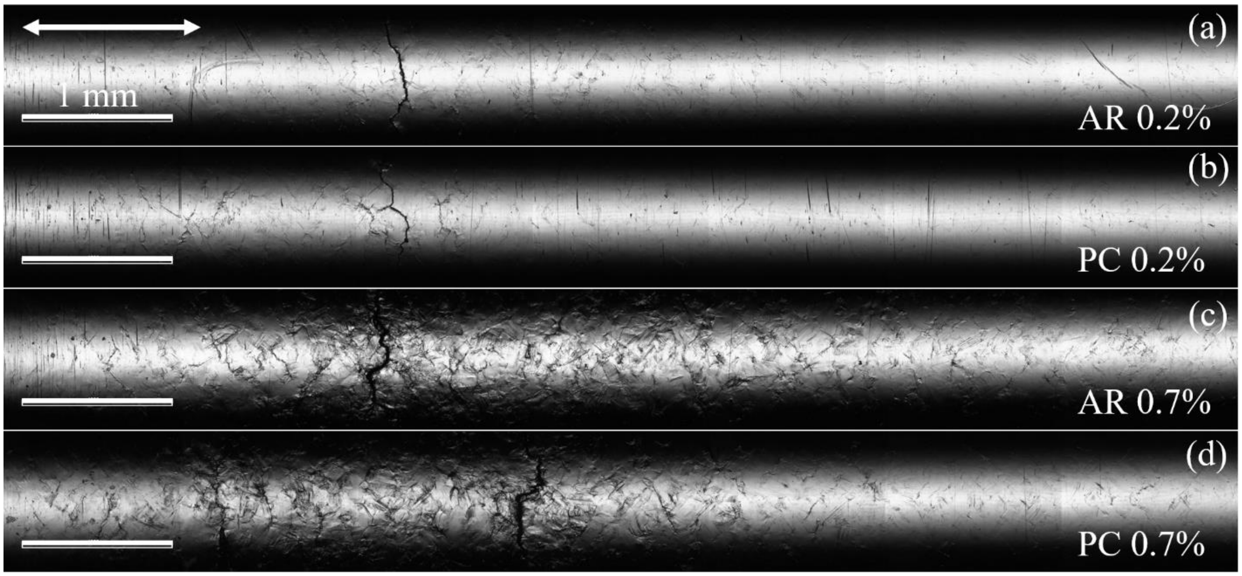

Fig. 2.9: Confocal microscopy images taken at different locations around the primary crack in (a, c) AR and (b, d) PC 316L stainless steel specimens after failure at $\Delta\varepsilon_p/2$ of (a, b) 0.2% and (c, d) 0.7%. The white arrow in (a) indicates the straining direction for all specimens. The imaged areas correspond to approximately 80% of the gage length.

### *2.3.6. Fracture Surface Observations*

Fig. 2.10 depicts a representative low magnification SEM image of the fracture surface of the AR condition tested at 0.2% plastic strain amplitude. Although the roughness of the fracture surface suggests that there is more than one crack initiation site and the crack path is tortuous, it is still possible to clearly define the crack propagation and tensile overload regions. The latter was induced by pulling the specimen in monotonic tension after the fatigue test was stopped, and it is characterized by voids and dimples typical of ductile fracture mechanisms. A similar topography was observed in the PC condition at the same plastic strain amplitude, but it is not shown here.

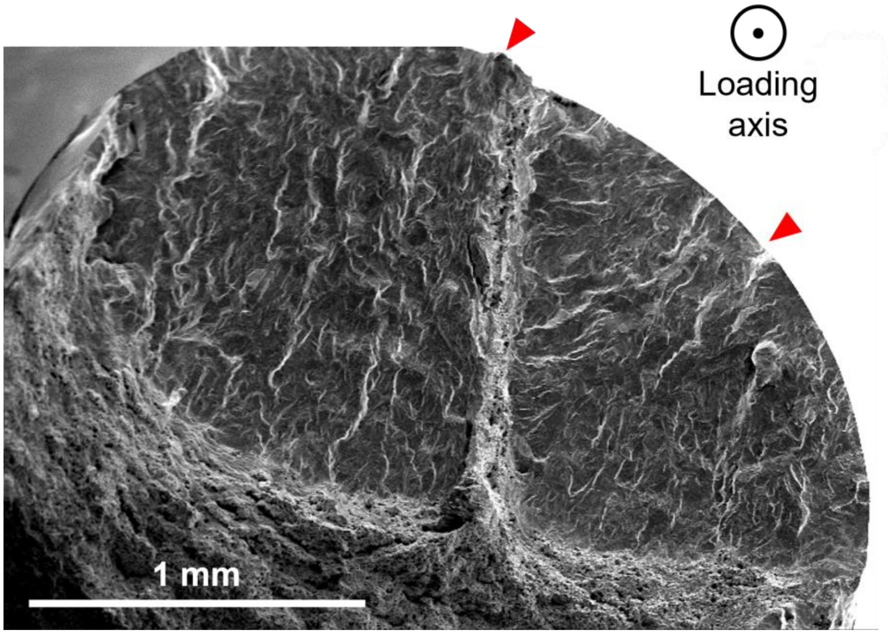

Fig. 2.10: SEM images for the AR specimen tested at $\Delta\varepsilon_p/2 = 0.2\%$ showing the fracture surface at a lower magnification. The red arrows point at the areas where the primary cracks possibly initiated.

Higher magnification SEM images of the fracture surfaces for both the AR and PC specimens are provided in Fig. 2.11. A few secondary cracks are apparent on the fracture surface in the PC condition when tested at 0.2% plastic strain amplitude (Fig. 2.11 (c)), but they are largely absent from the AR counterpart (Fig. 2.11 (a)). The observed secondary cracks on the PC fracture surface after testing at 0.2% plastic strain amplitude may be related to the microcracks apparent on the specimen surfaces (Fig. 2.7 (d)), as they appear to be associated with slip traces and planar features. In addition, parallel fatigue striations are visible in some regions for both conditions as shown in Fig. 2.11 (a) - (d), suggesting that the main mechanism of fatigue crack propagation in this alloy with and without hydrogen is through crack-tip blunting and resharpening [47, 48].

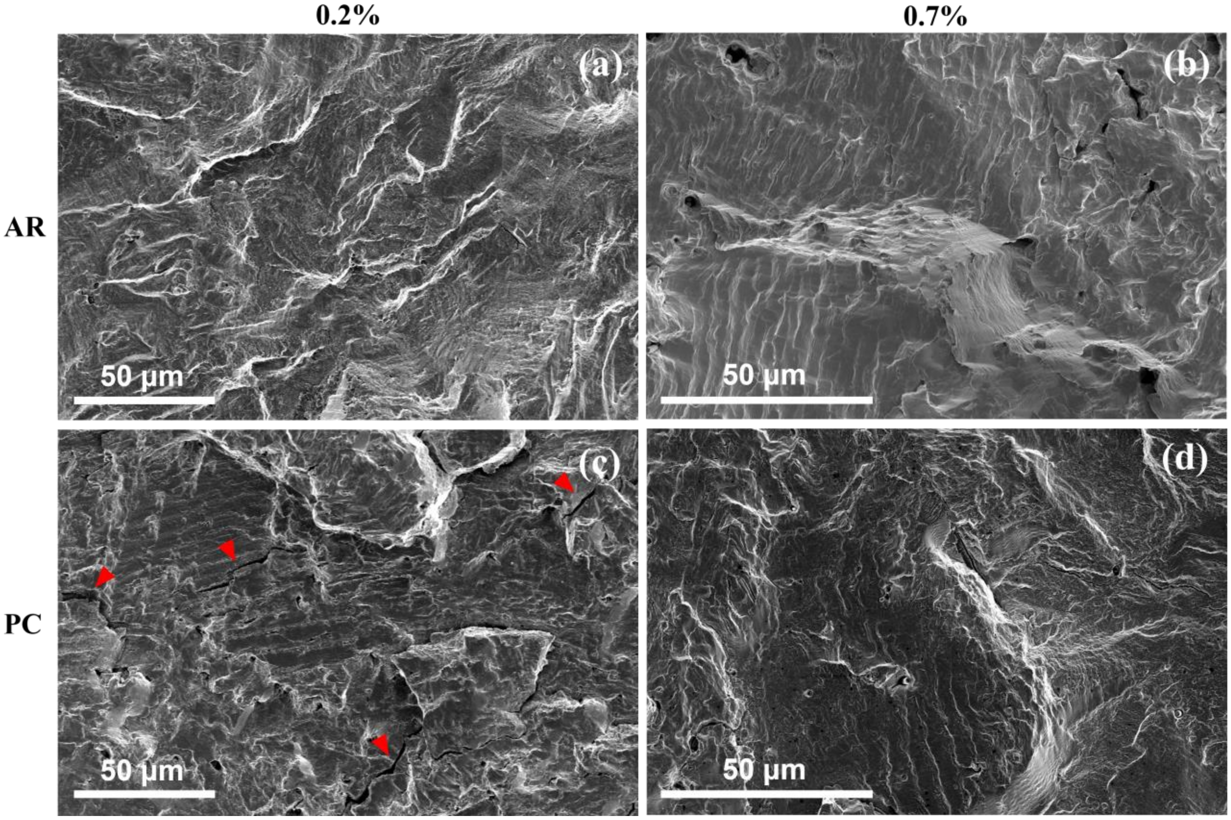

Fig. 2.11: Fracture surface SEM images for the (a, b) AR and (c, d) PC specimen tested at $\Delta\varepsilon_p/2$ of (a, c) 0.2% and (b, d) 0.7% showing the crack propagation area. Red arrows in (c) point at microcracks along the testing direction.

## 2.4. Discussion

### *2.4.1. Fatigue Deformation Damage*

The strain-hardened 316L austenitic stainless steel examined in this study exhibits continuous softening over the course of the LCF test at all plastic strain amplitudes as revealed in Figs. 2.3

and 2.5. Other researchers have attributed softening during cyclic straining in metals to the interaction of mobile dislocations and consequent changes in the strain hardened microstructure [14, 49]. In addition, tension and compression peak stresses have similar magnitudes over the majority of the lifetime for both the AR and PC conditions at all plastic strain amplitudes, as seen in the stress response curves in Fig. 2.3. Ma, *et al.* [50] analyzed the tension-compression symmetry during cyclic deformation in terms of percentage difference between the tension and compression peak stresses. They attributed the symmetric behavior to the lack of constraints that would lead to strain localization and heterogeneous plastic deformation. Since the measured peak stresses represent the flow stress averaged across the entire gage volume, the tension-compression symmetry observed throughout most of the fatigue lifetime suggests that plastic deformation occurs in a homogeneous manner on a macroscopic scale during straining for both AR and PC conditions. These observations are supported by the results of the Bauschinger analysis in Fig. 2.4; these results show that the major contribution to the stress response curves in AR and PC at all plastic strain amplitudes comes from effective stresses, which induce isotropic hardening [51]. Therefore, the tension and compression symmetry revealed in Fig. 2.3 is consistent with the non-directional strengthening suggested by the dominant presence of effective stresses.

Internal hydrogen increases the strength of austenitic stainless steels in tensile tests, typically on the order of 10-20% for 150 wt. ppm internal hydrogen [42, 52]. Consideration of the strengthening effect of internal hydrogen in stress-based fatigue has also been shown to be important [8, 9, 39, 40]. A similar hydrogen-induced strengthening effect is observed here in the stress response curves (Fig. 2.3) and for both monotonic and cyclic stress-strain curves (Fig. 2.5), although the hydrogen-induced strengthening is somewhat greater for the cyclic than for the monotonic flow curves. Furthermore, there is a greater difference in peak stress values between the AR and PC conditions at low strain amplitudes than at high amplitudes (Figs. 2.4 and 2.5). At 0.1% plastic strain amplitude, the presence of hydrogen increases the tension flow stress by approximately 18% in the first cycle (monotonic data) and 24% at half-life (cyclic data). In contrast, at 0.7% plastic strain amplitude the increase is less than 10% and 15% for the first cycle and half-life, respectively. This greater influence of internal hydrogen on flow stress at low plastic strain amplitudes is due to the difference in effective stresses between AR and PC conditions revealed by the Bauschinger analysis shown in Fig. 2.4 (a); it also correlates with the larger difference in LCF lifetime between AR and PC in the low amplitude regime (Fig. 2.6). Since effective stresses are often correlated to dislocation and solid solution strengthening mechanisms [31-34], these results indicate a higher concentration of short-range obstacles to dislocation glide at low amplitude when hydrogen is present (PC) compared to without hydrogen (AR). In contrast, for higher plastic strain amplitude, internal hydrogen has a comparatively modest influence on the effective stresses, and the flow stresses in the PC condition are attributed to hydrogen's influence on both the effective and back stresses. For both PC and AR conditions, the back stresses at high strain amplitude represent a larger fraction of the total flow stress than at low amplitude, underscoring the importance of long-range dislocation interactions at higher strain amplitudes. Therefore, this analysis demonstrates that internal hydrogen has large influence on short-range dislocation interactions (effective stress component) at low amplitudes; however, when the strain amplitudes become relatively large, the longer range interactions (back stresses) contribute more to the stress response. The latter effect is more significant in the presence of internal hydrogen.

The changes of back stresses in AR and PC conditions as the plastic strain amplitude increases correspond with the evolution of dislocation arrangements within the microstructure. Well-defined dislocation-cell structures are commonly reported in 316L stainless steel observed after exposure to cyclic loading conditions [7, 53, 54]. Our STEM observations of the AR condition also show the presence of well-defined cellular structures after interrupted tests at 0.3 and 0.8% plastic strain amplitude (Fig. 2.12 (a) and (b), respectively). In contrast, comparable well-defined cellular structures with tight walls were only observed in the PC condition at the high plastic strain amplitude (Fig. 2.12 (d)). At the lower strain amplitude (0.3%), only diffuse cells and loose tangles of dislocations are observed (Fig. 2.12 (c)). Similar diffuse cells and dense dislocation tangles were also observed in the untested as-received (strain hardened) material. Dislocation cells are a potential source of back stresses in both AR and PC conditions and the change in back stresses with amplitude correlates with the change in substructure, which is more significant when internal hydrogen is present. Because cell structures contribute to a homogeneous deformation behavior [55], such structures help explain the more similar lifetimes in both conditions at high plastic strain amplitudes.

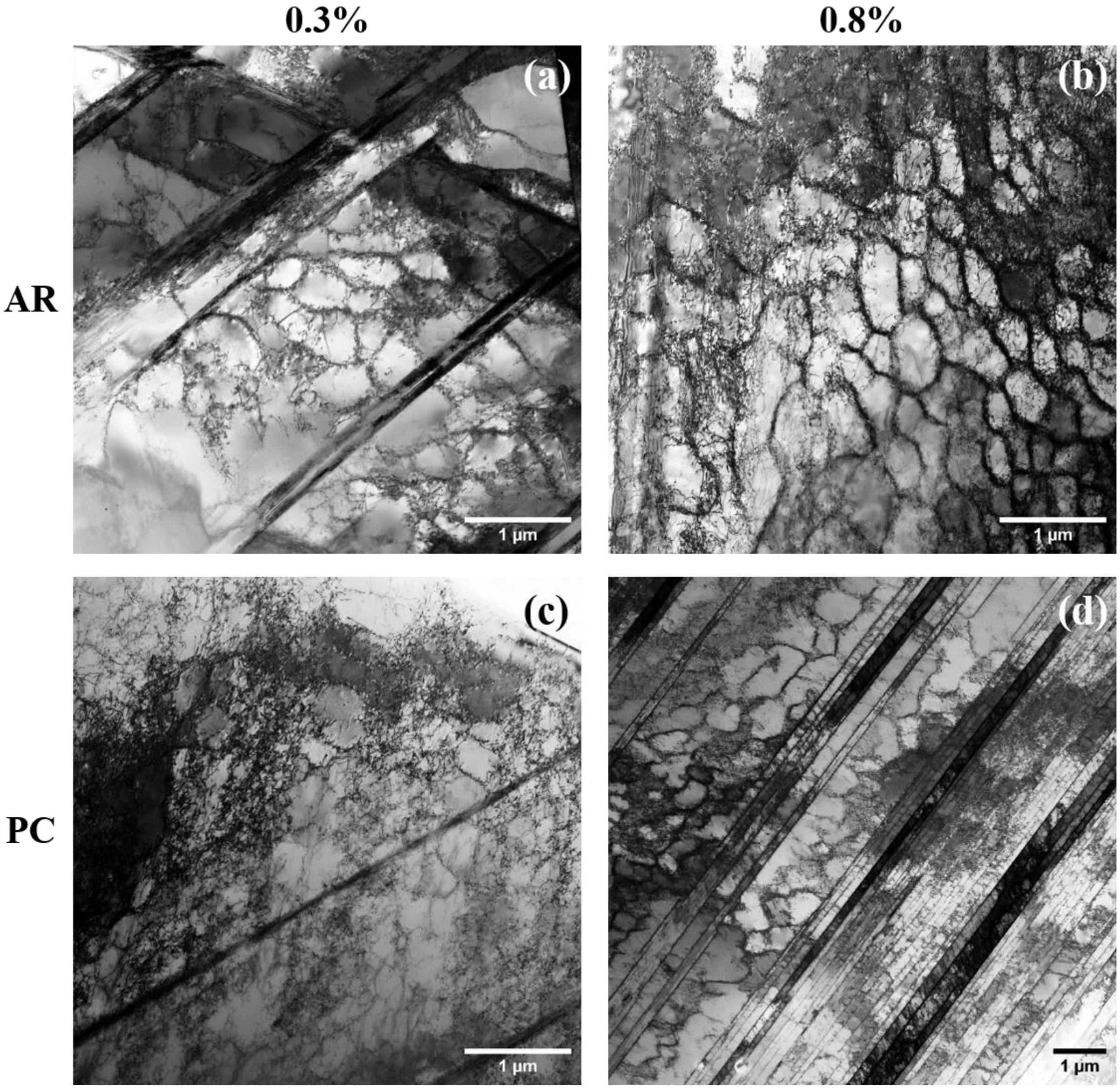

Fig. 2.12: STEM images of (a, b) AR and (c, d) PC 316L steels at (a, c) 0.3% and (b, d) 0.8% plastic strain amplitude showing dislocation cell structures. The images were obtained following LCF tests interrupted at half-life.

The planar slip structures present on the gage surface of AR and PC specimens (Figs. 2.7 and 2.8) characterize the deformation within a grain and result from dislocations gliding primarily in one family of slip planes [56]. These structures are typical in austenitic stainless steels because of their low stacking fault energy [57, 58]. Fig. 2.7 (c) and (d) show multiple slip activity in several grains around the primary crack in the PC condition after testing at 0.2% plastic strain amplitude. In contrast, in the AR condition after a similar level of cumulative plastic strain (Fig. 2.7 (a) and (b)), the gage surface revealed a much lower concentration of intersecting slip traces. Multiple slip is commonly activated in polycrystalline FCC metals at high values of local stresses [14]. Additionally, previous studies have proposed that hydrogen favors localization of slip into planar slip bands and therefore enhances the local shear strains and stresses in austenitic stainless steels [10, 59, 60]. These observations suggest that internal hydrogen plays an important role in enhancing slip planarity and promoting strain localization and hardening, which leads to the activation of multiple slip at lower values of cumulative plastic strain than in the absence of hydrogen. These planar features are also consistent with the dominant contribution of effective stresses to the flow stress, reflecting the importance of short-range dislocation interactions. In contrast, the formation of dislocation cells at high imposed strain levels, as shown in Fig. 2.12, reduces the impact of hydrogen on planar slip.

### *2.4.2. Fatigue Crack Initiation*

It is well established that accumulation of permanent cyclic damage leads to microcracking, which decreases the stiffness of the material and induces anisotropy in the stress-strain behavior [14, 61, 62]. In the context of this work, the coalescence of fatigue-induced microcracks into a propagating primary crack is assumed to coincide with the observed change in the shape of the hysteresis loops during a LCF test. The evolution of these loops with cyclic straining is illustrated in Fig. 2.A.1. Assuming that the modulus is linearly proportional to the cross-sectional area, a change of apparent elastic modulus of 1% represents a circumferentially uniform crack with a depth of about 8μm (but represents an equivalent area of about 40 grains, assuming a grain size of 50μm). In reality, cracks do not initiate uniformly around the circumference of the specimen; rather multiple cracks initiate at the surface before propagating across the gage diameter. Thus, this definition of crack initiation is characterized by crack(s) substantially larger than 8μm but assumed to represent nominally 1% of the cross-sectional area and tens of grains.

As described with respect to the strain-life results (section 2.3.4), crack initiation represented 85% of the life for the AR condition and 78% of the life for the PC condition. These numbers suggest only a small difference in average fraction of the life necessary to initiate a primary crack. However, since the number of cycles to failure is lower in the PC condition at a given strain amplitude, the formation of a crack occurs after substantially fewer cycles in the PC than the AR condition (Fig. 2.6). The initiation of the primary crack reduces the load carrying capacity of the gage section and localizes the damage around the crack(s). This process is readily observable in the PC specimen when comparing the confocal microscopy images in Fig. 2.9 (c) and (d). Furthermore, the accelerated formation of these microscopic flaws in PC specimens correlates with the higher effective stresses (generally due to dislocation interactions with solutes or other dislocations) in presence of internal hydrogen and to the activation of multiple slip systems at lower magnitudes of cumulative plastic strains than in the AR condition. Secondary slip planes can be obstacles to slip, promoting local stress concentrations and the formation of microcracks, which are processes that appear to be enhanced by hydrogen as described by Nibur, *et al.* for fracture [63]. In fatigue, the same processes are at play: hydrogen promotes strain accumulation in deformation bands (as shown by Sabisch, *et al.* [13]), thus activating multiple slip and inducing microcrack formation on intersecting planes. In short, internal hydrogen promotes interaction of slip planes and initiation of microcracks at these locations, as seen on the gage surface in Fig. 2.8 (d) and on the fracture surfaces in Fig. 2.11 (c).

### *2.4.3. Fatigue Crack Propagation and Failure*

Fatigue cracks generally propagate at a higher rate in the PC condition than in the AR condition according to the analysis presented in Fig. 2.6, consistent with observations from other studies of fatigue crack growth in austenitic stainless steels [7, 22, 64-68]. Whereas the fraction of the fatigue life associated with propagation is slightly greater in the PC condition, the absolute number of cycles to propagate a crack to failure is generally less in the PC condition. Considering the higher flow stress in the PC condition for the same strain amplitude, one would expect the cracks to propagate faster in the PC condition, since the driving force on a macroscopic crack is related to the applied stress. Additionally, the role of hydrogen in constraining deformation into planar slip bands and promoting microcracking (as discussed above) may also contribute to enhanced crack growth.

As illustrated in Fig. 2.11, fatigue cracks were transgranular in specimens both with and without hydrogen. There was no evidence that hydrogen activated grain boundary fracture or changed the cracking on the length scale of the grains. Again, internal hydrogen significantly reduces the total LCF lifetime of this material at all plastic strain amplitudes, although this effect is greatest at low plastic strain amplitudes. This detrimental effect related to its influence on deformation as observed in the stress response curves, Bauschinger analysis and strain-life plots (Figs. 2.3, 2.4 and 2.6, respectively) and is consistent with other investigations of fatigue performance in hydrogen environments [4, 6, 21, 69].

## 2.5. Conclusions

Low cycle fatigue tests were performed to investigate the influence of internal hydrogen on strain-hardened 316L austenitic stainless steel under plastic strain-control at constant plastic strain rate for as-received (AR), heat-treated (HT) and H-precharged (PC) conditions. The main findings are summarized as follows:

1. Although monotonic and cyclic strengths were greater in PC than in AR specimens, the total LCF lifetimes were significantly reduced in the PC condition at all tested amplitudes. This effect is more significant at low amplitudes than at high amplitudes. Comparisons of the stress response curves for AR, PC and HT conditions confirmed that the degradation in LCF performance is indeed induced by hydrogen, not by the thermal exposure during H-precharging.

2. The Bauschinger analysis revealed that effective stresses represent the major contribution to the flow stresses at all conditions and plastic strain amplitudes. At low amplitudes, the higher cyclic flow stress in the PC condition is attributed exclusively to the influence of internal hydrogen on the effective stresses. For high strain amplitude, internal hydrogen increases the cyclic flow stress through both effective and back stresses. This transition from hydrogen principally affecting the effective stresses at low strain amplitude to greater influence on the back stress at higher strain amplitude is consistent with a transition from short-range hydrogen dislocation interactions at low strain amplitude toward hydrogen influence on longer range interactions at higher strain amplitude.

3. The crack initiation analysis revealed that most of the fatigue lifetime is spent on the process of fatigue crack initiation at all plastic strain amplitudes and material conditions.

However, internal hydrogen accelerates crack initiation, resulting in more localized damage along the gage section. Although the percentage of the total life corresponding to crack propagation is larger in the PC condition, the absolute number of cycles to propagate a crack to failure of the specimen is smaller when internal hydrogen is present. This observation is consistent with the higher cyclic stresses found in presence of hydrogen at a given strain amplitude, which act as the driving force for crack propagation.

4. SEM observations revealed planar slip as an important deformation mode in both conditions. At low plastic strain amplitudes, internal hydrogen promotes slip planarity and multiple slip at lower cumulative plastic strains than in the AR condition. The resultant local increase in shear stresses would act as driving force for the initiation of microcracks at slip band intersections when internal hydrogen is present, resulting in crack initiation at lower number of cycles compared to specimens without hydrogen. Furthermore, hydrogen inhibits the formation of cell structures after cyclic deformation at low amplitude. At high amplitudes, the deformation induced cellular microstructures are very similar in both conditions; this similarity leads to more homogeneous deformation and is correlated with the smaller difference in LCF lifetime between the AR and PC conditions.

## Acknowledgements

We would like to thank Brian Kagay and Jay Foulk for the discussions about the LCF results, Nicholas Lundgren for the assistance with the crack initiation analysis, and Ryan Nishimoto for the assistance with the TEM specimen preparation. Partial funding for this research was provided by the University of California, Davis and by donations to the Department of Materials Science and Engineering. The Thermo Fisher Quattro S SEM was funded through the US National Science Foundation under award DMR-1725618. This work was supported by the Office of Energy

Efficiency and Renewable Energy's H-Mat Energy Materials Network funded through the Hydrogen and Fuel Cell Technologies Office at the U.S. Department of Energy. Sandia National Laboratories is a multi-mission laboratory managed and operated by National Technology & Engineering Solutions of Sandia, LLC, a wholly owned subsidiary of Honeywell International Inc., for the U.S. Department of Energy's National Nuclear Security Administration under contract DE-NA0003525. This paper describes objective technical results and analysis. Any subjective views or opinions that might be expressed in the paper do not necessarily represent the views of the U.S. Department of Energy or the United States Government.

## References

[1] C. C. Elam, C. E. G. Padró, G. Sandrock, *et al.*, Realizing the hydrogen future: the International Energy Agency's efforts to advance hydrogen energy technologies, *Int J Hydrog Energy* 28 (6) (2003) 601-607.

[2] L. M. Gandia, G. Arzamedi, P. M. Diéguez, Renewable Hydrogen Energy: An Overview, in: L. M. Gandia, G. Arzamedi, P. M. Diéguez (Eds.), Renewable Hydrogen Technologies: Production, Purification, Storage, Applications and Safety, *Newnes*, 2013, pp. 1-17.

[3] R. Singh, M. Singh, S. Gautam, Hydrogen economy, energy, and liquid organic carriers for its mobility, *Materials Today: Proceedings* 46 (2021) 5420-5427.

[4] P. J. Gibbs, K. A. Nibur, C. San Marchi, Plastic Ratcheting and Fatigue Crack Formation in Austenitic Steels with Hydrogen, in: B. P. Somerday, P. Sofronis (Eds.), International Hydrogen Conference (IHC 2016): Materials Performance in Hydrogen Environments, *ASME Press*, 2017, pp. 306-315.

[5] N. K. Kuromoto, A. S. Guimaraes, C. M. Lepienski, Superficial and internal hydrogenation effects on the fatigue life of austenitic steels, *Mat Sci Eng A* 381 (1-2) (2004) 216-222.

[6] K. E. Nygren, A. Nagao, P. Sofronis, *et al.*, The Role of Microstructure in Hydrogen-Induced Fatigue Failure of 304 Austenitic Stainless Steel, *Metall Mater Trans A* 51 (11) (2020) 5704-5714.

[7] K. E. Nygren, A. Nagao, S. Wang, *et al.*, Influence of internal hydrogen content on the evolved microstructure beneath fatigue striations in 316L austenitic stainless steel, *Acta Mater* 213 (2021).

[8] T. Iijima, H. Enoki, J. Yamabe, *et al.*, Effect of High Pressure Gaseous Hydrogen on Fatigue Properties of SUS304 and SUS316 Austenitic Stainless Steel, ASME 2018 Pressure Vessels and Piping Conference, 2018.

[9] P. J. Gibbs, C. San Marchi, K. A. Nibur, *et al.*, Comparison of Internal and External Hydrogen on Fatigue-Life of Austenitic Stainless Steels, *Proceedings of the ASME 2016 Pressure Vessels and Piping Conference* 6B (2016) 1-8.

[10] K. A. Nibur, D. F. Bahr, B. P. Somerday, Hydrogen effects on dislocation activity in austenitic stainless steel, *Acta Mater* 54 (10) (2006) 2677-2684.

[11] I. M. Robertson, P. Sofronis, A. Nagao, *et al.*, Hydrogen Embrittlement Understood, *Metall Mater Trans A* 46a (6) (2015) 2323-2341.

[12] P. J. Ferreira, I. M. Robertson, H. K. Birnbaum, Hydrogen effects on the interaction between dislocations, *Acta Mater* 46 (5) (1998) 1749-1757.

[13] J. E. C. Sabisch, J. D. Sugar, J. Ronevich, *et al.*, Interrogating the Effects of Hydrogen on the Behavior of Planar Deformation Bands in Austenitic Stainless Steel, *Metall Mater Trans A* 52 (4) (2021) 1516-1525.

[14] S. Suresh, Fatigue of materials, *Cambridge university press*, 1998.

[15] P. Lukáš, M. Klesnil, J. Polak, High cycle fatigue life of metals, *Mater Sci Eng* 15 (2-3) (1974) 239-245.

[16] J. Morrow, Cyclic plastic strain energy and fatigue of metals, Internal friction, damping, and cyclic plasticity, *ASTM International*, 1965.

[17] N. E. Dowling, Fatigue failure predictions for complicated stress strain histories, *University of Illinois at Urbana-Champaign*, 1971.

[18] C. San Marchi, J. A. Zimmerman, X. Tang, *et al.*, Fatigue Life of Austenitic Stainless Steel in Hydrogen Environments, *Proceedings of the ASME 2015 Pressure Vessels and Piping Conference* 6B (2015).

[19] C. San Marchi, P. J. Gibbs, J. W. Foulk, *et al.*, Fatigue Life of Austenitic Stainless Steels in Hydrogen Environments, 43rd MPA Seminar, Stuttgart, Germany, 2017.

[20] M. L. Martin, C. Looney, P. Bradley, *et al.*, Unification of hydrogen-enhanced damage understanding through strain-life experiments for modeling, *Eng Fract Mech* 216 (2019) 106504.

[21] T. T. Nguyen, J. Park, S. H. Nahm, *et al.*, Ductility and fatigue properties of low nickel content type 316L austenitic stainless steel after gaseous thermal pre-charging with hydrogen, *Int J Hydrog Energy* 44 (51) (2019) 28031-28043.

[22] Y. Murakami, S. Matsuoka, Effect of hydrogen on fatigue crack growth of metals, *Eng Fract Mech* 77 (11) (2010) 1926-1940.

[23] N. J. H. Holroyd, D. Hardie, Strain-Rate Effects in the Environmentally Assisted Fracture of a Commercial High-Strength Aluminum-Alloy (7049), *Corros Sci* 21 (2) (1981) 129-144.

[24] T. Kumamoto, M. Koyama, K. Sato, *et al.*, Strain-rate sensitivity of hydrogen-assisted damage evolution and failure in dual-phase steel: From vacancy to micrometer-scale void growth, *Eng Fract Mech* 216 (2019).

[25] J. K. Tien, A. W. Thompson, I. M. Bernstein, *et al.*, Hydrogen Transport by Dislocations, *Metall Trans A* 7 (6) (1976) 821-829.

[26] H. K. Birnbaum, P. Sofronis, Hydrogen-Enhanced Localized Plasticity - a Mechanism for Hydrogen-Related Fracture, *Mat Sci Eng A* 176 (1-2) (1994) 191-202.

[27] C. San Marchi, B. P. Somerday, S. L. Robinson, Permeability, solubility and diffusivity of hydrogen isotopes in stainless steels at high gas pressures, *Int J Hydrog Energy* 32 (1) (2007) 100-116.

[28] J. L. Walley, E. J. Lavernia, J. C. Gibeling, Low-Cycle Fatigue of Ultra-Fine-Grained Cryomilled 5083 Aluminum Alloy, *Metall Mater Trans A* 40 (11) (2009) 2622-2630.

[29] D. Kuhlmann-Wilsdorf, C. Laird, Dislocation behavior in fatigue II. Friction stress and back stress as inferred from an analysis of hysteresis loops, *Mater Sci Eng* 37 (2) (1979) 111-120.

[30] A. H. Cottrell, Dislocations and plastic flow in crystals, *Am J Phys* 22 (4) (1954) 242-243.

[31] G. Moan, J. Embury, A study of the bauschinger effect in Al-Cu alloys, *Acta Metall* 27 (5) (1979) 903-914.

[32] K. Lu, A. Chauhan, F. Knöpfle, *et al.*, Effective and back stresses evolution upon cycling a high-entropy alloy, *Mater Res Lett* 10 (6) (2022) 369-376.

[33] H. Mughrabi, Dislocation wall and cell structures and long-range internal stresses in deformed metal crystals, *Acta Metall* 31 (9) (1983) 1367-1379.

[34] X. Feaugas, On the origin of the tensile flow stress in the stainless steel AISI 316L at 300 K: Back stress and effective stress, *Acta Mater* 47 (13) (1999) 3617-3632.

[35] M. E. Mercer, S. L. Dickerson, J. C. Gibeling, Cyclic Deformation of Dispersion-Strengthened Aluminum Alloys, *Mat Sci Eng A* 203 (1-2) (1995) 46-58.

[36] J. M. Meininger, S. L. Dickerson, J. C. Gibeling, Observations of Tension/Compression Asymmetry in the Cyclic Deformation of Aluminum Alloy 7075, *Fatigue Fract Eng Mater Struct* 19 (1) (1996) 85-97.

[37] C. Sommer, H. J. Christ, H. Mughrabi, Nonlinear Elastic Behavior of the Roller Bearing Steel Sae 52100 during Cyclic Loading, *Acta Metall Mater* 39 (6) (1991) 1177-1187.

[38] H. Mughrabi, Cyclic Strain Rate Effects in Fatigued Face-Centred and Body-Centred Cubic Metals, *Philos Mag* 93 (28-30) (2013) 3821-3834.

[39] C. Skipper, G. Leisk, A. Saigal, *et al.*, Effect of Internal Hydrogen on Fatigue Strength of Type 316 Stainless Steel, in: B. Somerday, P. Sofronis, R. Jones (Eds.), Effects of Hydrogen on Materials: Proceedings of the 2008 International Hydrogen Conference, *ASM International*, 2009, pp. 139-146.

[40] D. M. Matson, A. Saigal, C. San Marchi, Fatigue Behavior of Austenitic Stainless Steel Alloys Thermally Pre-Charged in Gaseous Hydrogen, in: B. P. Somerday, P. Sofronis (Eds.) International Hydrogen Conference (IHC 2012): Hydrogen-Materials Interactions, 2012, pp. 375-382.

[41] A.-M. Brass, J. Chêne, Hydrogen uptake in 316L stainless steel: Consequences on the tensile properties, *Corros Sci* 48 (10) (2006) 3222-3242.

[42] C. San Marchi, B. P. Somerday, X. Tang, *et al.*, Effects of alloy composition and strain hardening on tensile fracture of hydrogen-precharged type 316 stainless steels, *Int J Hydrog Energy* 33 (2) (2008) 889-904.

[43] Y. Murakami, T. Kanezaki, Y. Mine, Hydrogen Effect against Hydrogen Embrittlement, *Metall Mater Trans A* 41a (10) (2010) 2548-2562.

[44] J. H. Hollomon, Tensile Deformation, *Trans Am Inst Min Metall* 162 (1945) 268-290.

[45] L. F. Coffin, Jr., A study of the effects of cyclic thermal stresses on a ductile metal, *Transactions of the American Society of Mechanical Engineers, New York* 76 (1954) 931-950.

[46] S. S. Manson, Behavior of Materials under Conditions of Thermal Stress, *National Advisory Committee for Aeronautics*, 1954, pp. 1-34.

[47] R. O. Ritchie, Mechanisms of fatigue-crack propagation in ductile and brittle solids, *Int J Fracture* 100 (1) (1999) 55-83.

[48] C. Laird, G. C. Smith, Crack Propagation in High Stress Fatigue, *Philos Mag* 7 (77) (1962) 847-&.

[49] H.-F. Chai, C. Laird, Mechanisms of cyclic softening and cyclic creep in low carbon steel, *Mater Sci Eng* 93 (1987) 159-174.

[50] B. T. Ma, Z. G. Wang, A. L. Radin, *et al.*, Asymmetry Behavior between Tension and Compression in the Cyclic Deformation of Copper Single-Crystals and Other Ductile Metals, *Mat Sci Eng A* 129 (2) (1990) 197-206.

[51] M. G. Stout, A. D. Rollett, Large-strain Bauschinger effects in fcc metals and alloys, *Metall Trans A* 21 (12) (1990) 3201-3213.

[52] C. San Marchi, J. A. Ronevich, J. E. C. Sabisch, *et al.*, Effect of microstructural and environmental variables on ductility of austenitic stainless steels, *Int J Hydrog Energy* 46 (23) (2021) 12338-12347.

[53] M. S. Pham, C. Solenthaler, K. G. F. Janssens, *et al.*, Dislocation structure evolution and its effects on cyclic deformation response of AISI 316L stainless steel, *Mat Sci Eng A* 528 (7-8) (2011) 3261-3269.

[54] Y. F. Li, C. Laird, Cyclic Response and Dislocation Structures of AISI 316L Stainless Steel. Part 2. Polycrystals Fatigued at Intermediate Strain Amplitude, *Mat Sci Eng A* 186 (1-2) (1994) 87-103.

[55] C. Laird, P. Charsley, H. Mughrabi, Low-Energy Dislocation-Structures Produced by Cyclic Deformation, *Mater Sci Eng* 81 (1-2) (1986) 433-450.

[56] H. Mughrabi, Cyclic Slip Irreversibilities and the Evolution of Fatigue Damage, *Metall Mater Trans B* 40 (4) (2009) 431-453.

[57] D. T. Pierce, J. A. Jiménez, J. Bentley, *et al.*, The influence of stacking fault energy on the microstructural and strain-hardening evolution of Fe–Mn–Al–Si steels during tensile deformation, *Acta Mater* 100 (2015) 178-190.

[58] I. Karaman, H. Sehitoglu, Y. I. Chumlyakov, *et al.*, The deformation of low-stacking-fault-energy austenitic steels, *JOM* 54 (7) (2002) 31-37.

[59] L. Zhang, B. An, S. Fukuyama, *et al.*, Hydrogen Effects on Localized Plasticity in SUS310S Stainless Steel Investigated by Nanoindentation and Atomic Force Microscopy, *Jpn J Appl Phys* 48 (8) (2009).

[60] D. P. Abraham, C. J. Altstetter, Hydrogen-Enhanced Localization of Plasticity in an Austenitic Stainless-Steel, *Metall Mater Trans A* 26 (11) (1995) 2859-2871.

[61] A. Litewka, On Stiffness and Strength Reduction of Solids Due to Crack Development, *Eng Fract Mech* 25 (5-6) (1986) 637-643.

[62] J. Aboudi, Stiffness Reduction of Cracked Solids, *Eng Fract Mech* 26 (5) (1987) 637-650.

[63] K. A. Nibur, B. P. Somerday, D. K. Balch, *et al.*, The role of localized deformation in hydrogen-assisted crack propagation in 21Cr-6Ni-9Mn stainless steel, *Acta Mater* 57 (13) (2009) 3795-3809.

[64] Y. Murakami, The effect of hydrogen on fatigue properties of metals used for fuel cell system, *Int J Fracture* 138 (1-4) (2006) 167-195.

[65] H. Matsunaga, H. Noda, Visualization of Hydrogen Diffusion in a Hydrogen-Enhanced Fatigue Crack Growth in Type 304 Stainless Steel, *Metall Mater Trans A* 42 (9) (2011) 2696-2705.

[66] T. Kanezaki, C. Narazaki, Y. Mine, *et al.*, Effects of hydrogen on fatigue crack growth behavior of austenitic stainless steels, *Int J Hydrog Energy* 33 (10) (2008) 2604-2619.

[67] G. Schuster, C. Altstetter, Fatigue of Stainless Steel in Hydrogen, *Metall Trans A* 14 (10) (1983) 2085-2090.

[68] Y. Oda, H. Noguchi, Observation of hydrogen effects on fatigue crack growth behaviour in an 18Cr-8Ni austenitic stainless steel, *Int J Fracture* 132 (2) (2005) 99-113.

[69] K. Rie, J. Ruge, W. Kohler, Low-cycle fatigue of Fe-Cr-Ni-austenite and Ni-base alloys in high pressure hydrogen, *Proceedings JIMIS-2, Hydrogen in Metals* 529 (1980).

# Chapter 3. The Kinetics of Dislocation Glide During Low Cycle Fatigue of 316L Stainless Steel Containing Hydrogen[2]

## Abstract

A framework of thermally activated dislocation glide is applied to investigate the effect of hydrogen on the mechanisms of cyclic deformation in strain-hardened 316L stainless steel. Non-charged and hydrogen-precharged (H-precharged) specimens were low cycle fatigue (LCF) tested under plastic strain control. A series of plastic strain rate changes was performed periodically at the peak true plastic strain from the first cycle to half-life, and at various plastic strain values around stable hysteresis loops at half-life to determine the operational activation area, $\Delta a^*$. Both material conditions experience a rapid increase in $\Delta a^*$ during the initial rapid softening, varying from 50-160 $b^2$ across different plastic strain amplitudes, followed by a region of steady values that coincide with the reduced rate of softening. At half-life, hydrogen decreases $\Delta a^*$ from 100-300 $b^2$ in non-charged to 60-200 $b^2$ in H-precharged conditions at a given true stress due to its effect on the activation distance and obstacle spacing. The magnitudes of $\Delta a^*$ and STEM observations of dislocation arrangements reveal that solutes, forest dislocations and cross slip are important thermal obstacles for dislocation glide at all plastic strain amplitudes, except that cross slip operates in the H-precharged condition only in the high amplitude regime. A Haasen plot analysis indicates that forest dislocations control the rate of deformation in both material conditions. It also reveals the presence of athermal obstacles in both non-charged and H-precharged conditions, likely to be dense dislocation tangles and cell walls. The effect of hydrogen on microstructure evolution leads to a dependence of athermal stress on plastic strain amplitude.

---

[2] To be submitted as D. M. Oliveira, C. W. San Marchi, D. L. Medlin, and J. C. Gibeling. *Acta Mater.* (2023).

**Keywords:** Low Cycle Fatigue; Plastic Strain Rate Change; Hydrogen; Activation Area; Thermally Activated Dislocation Glide.

### 3.1. Introduction

The increasing demand for hydrogen-based technologies and expected increase in hydrogen fuel usage have raised concerns about the performance of structural alloys in high hydrogen gas pressure environments. Because hydrogen used as a fuel must be stored at high pressures, systems for its distribution are subject to repeated pressurization cycles leading to fatigue damage and potential failure. Furthermore, hydrogen is well-known to interact with materials and compromise their structural integrity, a process broadly referred to as hydrogen embrittlement, which has been studied by numerous researchers for over 100 years [1-4].

Several studies of the influence of internal hydrogen on the high cycle fatigue performance of austenitic stainless steels, a class of materials commonly used in hydrogen handling systems, have been reported in literature [5-12]. Most of these were conducted under load control, which may not be the ideal approach to understanding mechanisms of damage accumulation and fatigue crack initiation [12]. Only a few strain-controlled low cycle fatigue (LCF) test results have been reported [11, 12]. Among these, Nguyen, *et al.* [11] investigated the total strain-controlled low cycle fatigue (LCF) behavior of a low nickel content 316L stainless steel with and without internal hydrogen. The authors attributed the reduction in LCF lifetime in the presence of internal hydrogen to hydrogen-induced localized deformation that led to microcrack formation in this material. Oliveira, *et al.* [12] also observed a decrease in LCF lifetime in hydrogen-precharged specimens tested under plastic strain control when compared to their non-charged counterparts; this effect was more significant at low plastic strain amplitudes. The degrading effect of hydrogen was correlated with dislocation interactions that lead to differences in effective stresses and dislocation microstructures when hydrogen is introduced. Although these studies provide an initial evaluation of the fatigue features present during and after testing at different (plastic) strain amplitudes, the fundamental nature of hydrogen interactions with dislocations that affect the macroscopic cyclic deformation behavior in austenitic stainless steel is still not fully explained.

A well-established methodology to investigate the kinetics of dislocation motion during deformation is through transient experiments, such as stress relaxation and strain rate change tests, founded on the theory of thermally activated dislocation glide [13]. In the latter test method, for example, a small and sudden perturbation of the initial deformation conditions (expressed as a change in plastic strain rate) results in an instantaneous and reversible change in the flow stress associated with thermally activated dislocation glide [14]. An important assumption for these relationships is that the microstructure remains constant at the instant of rate change [13-15], which could be achieved by changing the rate of deformation nearly instantaneously and having a very high time resolution for data acquisition. The change in stress measured during the strain rate change tests is then used to determine the activation area, a thermal activation parameter that reflects the length scale of dislocation interactions with discrete obstacles on the glide plane. The true activation area Δa is a function of the activation distance Δy and the equilibrium distance between obstacles in a uniform distribution $l_e$, as represented in Eq. (3.1) [13].

$$\Delta a = \Delta y \times l_e \qquad \text{Eq. (3.1)}$$

Experimentally, the parameter calculated during the rate change tests is the operational activation area $\Delta a^*$, which reflects the dependence of the thermal activation rate on the flow stress σ (Eq. (3.2)).

$$\Delta a^* = \frac{M k_B T}{b} \times \frac{\partial \ln \dot{\varepsilon}_p}{\partial \sigma} \qquad \text{Eq. (3.2)}$$

where M is the Taylor factor (3.06 for FCC materials), $k_B$ is the Boltzmann constant ($1.38\text{x}10^{-23}$ J/K), T is the temperature, b is the magnitude of the Burgers vector (0.254 nm for 316L stainless steel [16]) and $\dot{\varepsilon}_p$ is the true plastic strain rate. According to Conrad [15], Basinski [17], and Bonneville and Escaig [18], typical orders of magnitude of operational activation areas for dislocation glide are 10-$10^2$ $b^2$ for control by lattice friction, $10^2$-$10^4$ $b^2$ for forest dislocations (varies with dislocation density), $10^2$-$10^3$ $b^2$ for solute atoms (varies with solute concentration) and 10-$10^2$ $b^2$ for cross slip.

An additional analysis of the thermal activation results, proposed by Kocks, Argon and Ashby [13] and by Mulford [19], consists of plotting the inverse of the operational activation area as a function of the flow stresses at a given microstructural state. This analysis is based on observations of thermal activation effects on the plasticity of nickel single crystals reported by Haasen [20], and it allows for the identification of the nature of the obstacles controlling dislocation glide kinetics. A schematic representation of the resulting Haasen plot is shown in Fig. 3.1, in which the inverse activation area normalized by the square of the magnitude of the Burgers vector is shown as a function of flow stress.

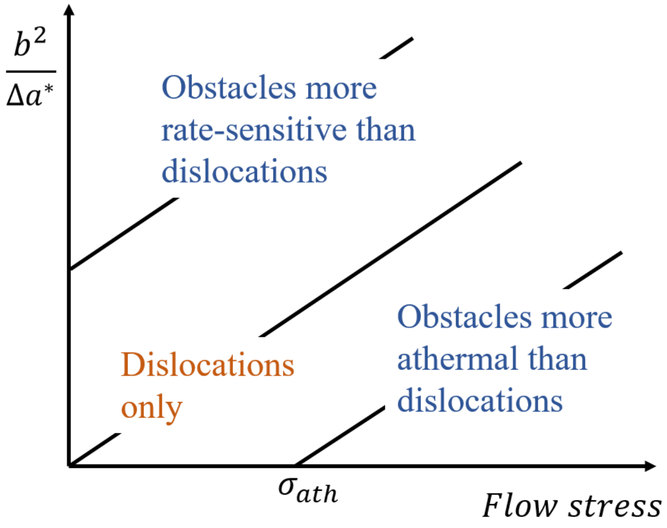

Fig. 3.1: Schematic representation of the Haasen plot and its interpretation. Adapted from [19].

If there is a single set of discrete obstacles to dislocation glide, namely forest dislocations, the data in the Haasen plot follow a linear behavior and can be extrapolated through the origin. This linear relationship indicates that the material obeys the Cottrell-Stokes law [21], i.e., the stress sensitivity of the strain rate ($\partial \ln(\dot{\varepsilon}_p)/\partial \ln(\sigma)$) at a given temperature and microstructure remains constant during strain hardening. If there are multiple sets of obstacles controlling dislocation glide, the relationship between the inverse of the activation area and the flow stress might still be linear if the Cottrell-Stokes law still holds, but an additional stress term needs to be considered [19]. Consequently, the Haasen plot data extrapolates through a positive or negative value of flow stress, indicating that the second set of obstacles is more athermal (rate-insensitive) or more thermal (rate-sensitive) than forest dislocations, respectively. The intercept on the positive stress axis is the athermal stress $\sigma_{ath}$ representing the contribution of the athermal obstacle(s) to the flow stress [19]. In addition, according to Mulford [19] and Kocks, Argon and Ashby [13], the slope of the Haasen plot is inversely proportional to the work done during thermal activation of rate-sensitive obstacles ($\Delta$W), which can be written as in Eq. (3.3) and reflects the characteristics of the thermal obstacle profile.

$$\Delta W = \sigma b \Delta a \qquad \text{Eq. (3.3)}$$

Sirois and Birnbaum [22] investigated the influence of internal hydrogen on thermally activated dislocation glide in pure Ni and Ni-C alloys using stress relaxation experiments. The authors reported a decrease in activation area in both materials in the presence of hydrogen, which was correlated to hydrogen shielding and hydrogen-enhanced dislocation mobility effects [23, 24]. Similar observations were made by Wang, *et al.* [25] after performing stress relaxation experiments in pure iron prepared by cathodic charging with hydrogen. However, to the authors' knowledge, there are no such experimental investigations comparing thermal activation parameters in hydrogen charged to those of non-charged austenitic stainless steels. Furthermore, no studies of the kinetics of dislocation glide during cyclic deformation of hydrogen-containing materials have been reported.

Within this context, the goal of the current study is to investigate the influence of hydrogen on the kinetics of dislocation glide in 316L austenitic stainless steel by applying plastic strain rate changes during cyclic deformation tests. Changes in operational activation area with increasing cumulative plastic strain are used to inform about the evolution of the dislocation interactions in a dynamic microstructure. At half-life, the analysis of the Haasen plot at a microstructural state of dynamic equilibrium provides information about the nature of the main obstacles controlling dislocation glide and strengthening of this steel. These test results, combined with scanning transmission electron microscopy (STEM) images, provide an integrated framework to characterize the effect of hydrogen on mechanisms of cyclic deformation in 316L stainless steel on the scale of dislocation glide, in addition to highlighting the fundamental interactions responsible for the strengthening in the presence of hydrogen.

## 3.2. Experimental

### ***3.2.1. Materials***

Type 316L austenitic stainless steel rods with 6.35 mm diameter were machined from a round bar commercially obtained in the strain-hardened condition into LCF test specimens with 3.2 mm gage diameters and 10.2 mm gage length. The specimen dimensions were in accordance with ASTM E606 specifications [26]. Further details of the alloy composition and specimen geometry are reported elsewhere [12]. The gage surfaces were mechanically ground and polished with SiC paper and diamond polishing compounds down to 0.25 µm. Specimens were tested in the non-charged (as-received or AR), with no intentional addition of hydrogen, and hydrogen-precharged (H-precharged or PC) conditions. The environment for H-precharging consisted of hydrogen gas at a pressure of 138 MPa and temperature of 573K. The specimens were exposed for 13 days, resulting in a hydrogen concentration of 155 wt. ppm as measured through inert gas fusion-infrared absorbance.

### *3.2.2. Low Cycle Fatigue and Plastic Strain Rate Change Methods*

A series of true plastic strain rate change experiments was performed during LCF tests using real-time calculations of true plastic strain as the controlling variable, as described previously [12]. The LCF tests were carried out in an MTS 810 servo-hydraulic testing machine running MTS TestStar and Testware-SX software codes adapted from Kaschner and Gibeling [27]. An MTS axial extensometer with gage length of 7.6 mm and an Interface force transducer with 11120 N capacity provided the total strain and load inputs, respectively, used for the calculation of true plastic strain. The system was carefully tuned to optimize response during the strain rate changes while avoiding instabilities. Furthermore, the modulus used to calculate the elastic strains was first obtained from tensile tests, then further refined to generate vertical segments at each end of the true stress-plastic strain hysteresis loops. The base cyclic command was a triangle wave with a constant plastic strain amplitude in the range of 0.3% to 0.8% for individual tests, resulting in a constant plastic strain rate of $1x10^{-3}$ $s^{-1}$ in each case. Duplicate experiments were carried out at each tested amplitude.

The plastic strain rate changes were imposed by switching test control to an external function generator (MTS 418.91 MicroProfiler) programmed via an auxiliary computer running custom software [27]. The external function generator was programmed to execute one complete cycle at the base strain rate prior to the cycle with the strain rate change, except during the first quarter cycle. Load and total strain data were collected by simultaneously triggering two Hewlett-Packard

3458A digital voltmeters at a sampling rate of 500 readings per second, and a total of 2000 readings were stored per rate change event (one second before and three seconds after the rate change). Two distinct types of experiments were conducted for each specimen. The first set of rate changes was performed periodically at the peak true plastic strain from the first cycle up to half-life to assess changes in operational activation area induced by an increase in cumulative plastic strain. The number of cycles corresponding to half-life for each plastic strain amplitude was determined based on previous LCF lifetime results in 316L stainless steel [12]. A typical testing sequence included a rate change every 3 cycles, starting in the first quarter cycle, for 8 rate changes, then every 10 cycles for 8 rate changes, every 20 cycles for 10 rate changes, every 50 cycles for 20 rate changes, and every 100 cycles until half-life was reached. At the selected peak strains, the applied plastic strain rate was changed from the nominal value of $1\text{x}10^{-3}$ $s^{-1}$ to a new value of $5\text{x}10^{-4}$ $s^{-1}$ and an additional 0.15% plastic strain was imposed at this second plastic strain rate, as illustrated in Fig. 3.2 (a). To calculate the operational activation area $\Delta a^*$ from the dependence of stress on plastic strain rate (Eq. (3.2)), the precise time of the rate change was defined based on the change in slope of the load-time data. True plastic strain rates were obtained from a linear fit of the true plastic strain-time data. Then, the load-time data at the second plastic strain rate were fitted with a weighted second order polynomial equation and back extrapolated to estimate the value of true stress immediately after the rate change. The assigned weighting factors were 1, 3 and 5, and the range of the load-time data for each value was chosen based on the extent of the oscillations (as visible in Fig. 3.2 (b)). In general, the polynomial fit in the region immediately after the rate change was weighted by a factor of 1, while the region near the end of the data (at the second rate) was weighted by a factor of 5. The variables of interest are identified in Fig. 3.2 (b). After each rate change, the specimen was cycled at the base plastic strain rate for at least two cycles to restore the base microstructure. Additional details regarding the LCF and plastic strain rate change experimental setup are described in previous publications [12, 27, 28].

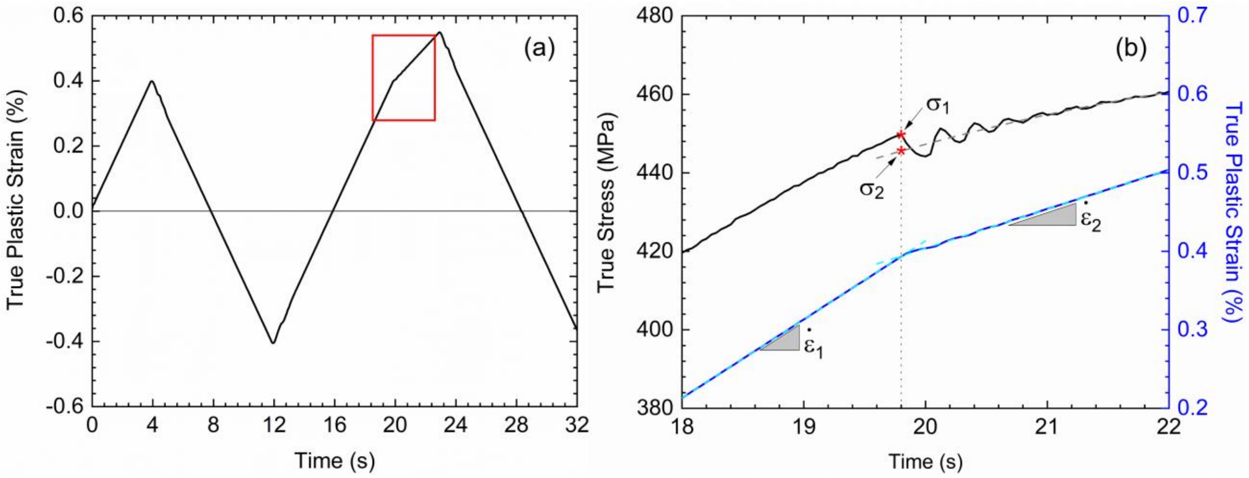

Fig. 3.2: Representative plots of (a) true plastic strain vs time, and (b) magnified true stress and true plastic strain responses at the moment of strain rate change. $\sigma_1$ and $\sigma_2$ are the true stresses immediately before and after the rate change, respectively. $\dot{\varepsilon}_1$ and $\dot{\varepsilon}_2$ are the true plastic strain rates.

In the second set of plastic strain rate change experiments, tests were conducted at several values of true plastic strain (hence also stress) around the stable hysteresis loops at half-life, with intervals of 10 cycles between each rate change event. In total, 11-16 points on the hysteresis loops were probed at each plastic strain amplitude, and the test routine was performed twice for each specimen (except at 0.8% plastic strain amplitude) to verify the consistency in operational activation area values at a given true stress. At half-life, the stress response curves from previous work [12] indicate that the microstructural changes are minimal with each cycle as the peak stresses remain essentially constant over many cycles. Thus, the relationship between operational activation area and true stress can be used to determine the nature of the dominant obstacles to dislocation motion.

### *3.2.3. Microscopic Characterization*

Although plastic strain rate change experiments themselves represent an important tool to obtain information at the level of dislocation interactions that is relevant to the macroscopic mechanical behavior, microscopic characterization was conducted to provide direct evidence of dislocation arrangements that further support the observations from thermal activation analysis parameters. Dislocation structures were investigated in the gage cross section of the untested and tested specimens, using specimens cut perpendicular to the loading direction, using a Thermo Fisher Scientific Themis Z scanning transmission electron microscope (STEM) operating at 300 kV and at a beam convergence of 3.0 mrad. Slices were mechanically thinned and polished followed by electrolytic polishing using a Struers TenuPol-5 system. The electropolishing media was a 90 vol. % ethanol and 10 vol. % perchloric acid solution, and the operating parameters were a voltage of 24.6 V, temperature of -10 ± 0.4°C, and current of 52 – 84 mA.

## 3.3. Results

### *3.3.1. Thermal Activation Parameters*

#### *3.3.1.1. Evolution of Operational Activation Areas from First Cycle to Half-Life*

Fig. 3.3 shows the inverse of the operational activation area normalized by the square of the Burgers vector ($b^2/\Delta a^*$) and plotted as a function of the cumulative plastic strain for tests at the various plastic strain amplitudes. Cumulative plastic strain is a measure to characterize the global accumulated deformation during each LCF test and is defined here as four times the plastic strain amplitude times the number of cycles [29]. The smaller cumulative plastic strain values to half-life for the PC condition reflect its shorter lifetime at all amplitudes. For all material conditions and plastic strain amplitudes, the operational activation area $\Delta a^*$ values sharply increase with increasing cumulative plastic strain during the initial cycles by a total of about 15-30 $b^2$, then maintain an approximately constant value until half-life is reached. At a given cumulative plastic strain, $\Delta a^*$ varies inversely with plastic strain amplitude; it is high at low amplitudes and low at high amplitudes. Additionally, the magnitudes of $\Delta a^*$ across all tested strain amplitudes are larger in the AR than in the PC condition, varying between 100-160 $b^2$ for AR and 50-100 $b^2$ for PC.

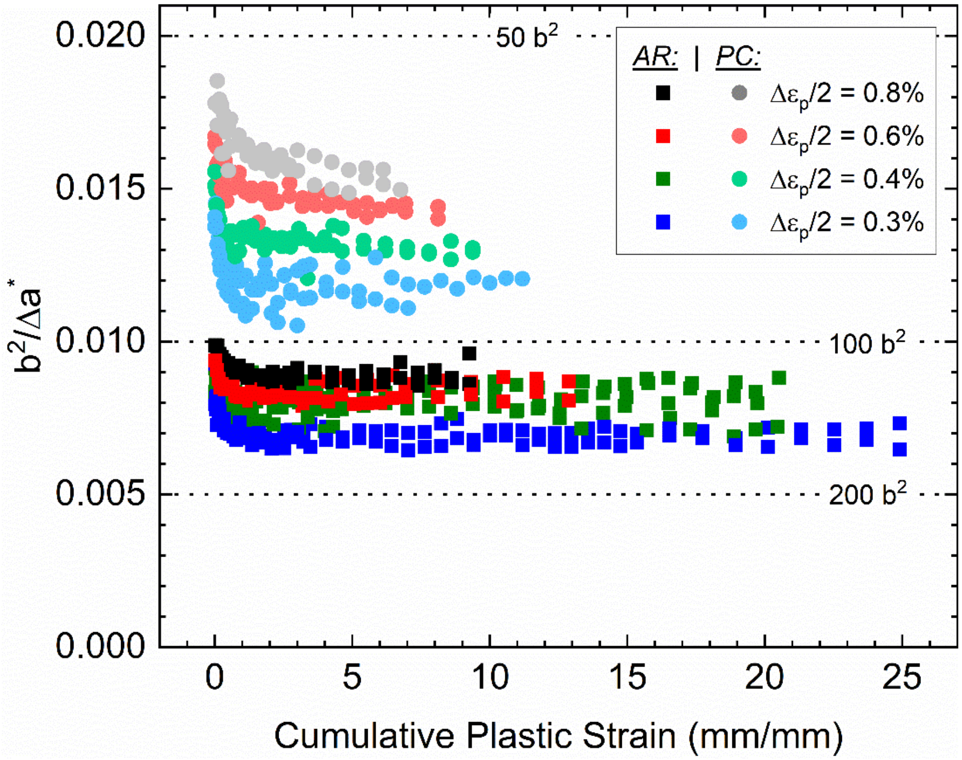

Fig. 3.3: Inverse of the operational activation area normalized by the square of the Burgers vector ($b^2/\Delta a^*$) as a function of cumulative plastic strain. Squares and circles represent AR and PC, respectively. Different colors represent different plastic strain amplitudes. The dotted lines indicate corresponding values of $\Delta a^*$ in units of $b^2$.

### 3.3.1.2. Operational Activation Areas at Half-Life

The Haasen plot obtained from the plastic strain rate change tests at half-life reveals the dependence of the operational activation area $\Delta a^*$ on the true stress at a state of dynamic equilibrium of the microstructure [30] and is shown in Fig. 3.4 (a) and (b) for AR and PC conditions, respectively. The combined data for all plastic strain amplitudes in the AR condition and the individual data for each plastic strain amplitude in the PC condition were fitted with a linear equation and extrapolated to the intercept with the axes; the fitting parameters are summarized in Table 3.1. The open symbols represent AR and PC data points that were not used in the linear fits. Inclusion of these points would lead to a curvature on the Haasen plot that deviates from the Cottrell-Stokes law. This curvature could be attributed to the presence of an additional set of thermal obstacles to dislocation glide for which the associated activation areas have a different dependence on the obstacle density than that of forest dislocations [13, 19]. In this case, separating the obstacle contributions to the flow stress is very challenging and goes beyond the scope of this paper. Alternatively, the curvature on the Haasen plot could mean that the contribution of the thermal and athermal obstacles to the flow stress cannot be added linearly [13, 19]. Last and most likely, it is difficult to resolve the small differences between $\sigma_1$ and $\sigma_2$ obtained when probing the hysteresis loops at low values of true stress, making it difficult to determine whether the curvature on the Haasen plot is meaningful in this stress regime. Therefore, the data points represented with open symbols are treated as outliers based on their corresponding stress sensitivity of the strain rate ($\partial\ln(\dot{\varepsilon}_p)/\partial\ln(\sigma)$), which lie outside the range between the 25th and 75th percentile by a factor of two times the interquartile range. Accordingly, we limit the interpretation of the data to the range of activation area values that follow the Cottrell-Stokes law and are represented by a linear dependence on the flow stress.

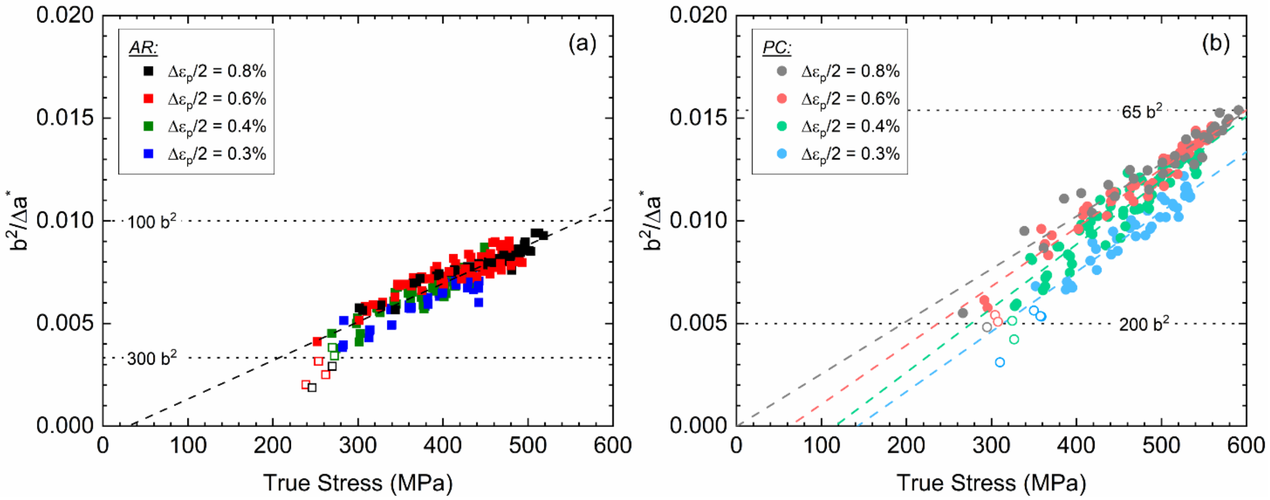

Fig. 3.4: Haasen plots for Type 316L in the (a) AR and (b) PC conditions. The data set for each plastic strain amplitude was fitted with a linear function. Open symbols indicate data points for the AR and PC conditions that were masked from the linear fit. The data selection for linear fitting was based on the evaluation of the interquartile range of the strain-rate sensitivity values for each strain rate change. The dotted lines indicate corresponding values of $\Delta a^*$ in units of $b^2$.

Table 3.1: Thermal activation parameters obtained from linear fitting of the Haasen plot data.

| **Condition** | **$\Delta\varepsilon_p/2$ (%)** | **Slope ($MPa^{-1}$)** | **$\sigma_{ath}$ (MPa)** | **R-Squared** |
|---|---|---|---|---|
| AR | all | $1.9 \times 10^{-5}$ | 41 | 0.807 |
| PC | 0.3 | $3.1 \times 10^{-5}$ | 164 | 0.929 |
| PC | 0.4 | $3.1 \times 10^{-5}$ | 116 | 0.882 |
| PC | 0.6 | $2.8 \times 10^{-5}$ | 42 | 0.950 |
| PC | 0.8 | $2.6 \times 10^{-5}$ | 1 | 0.923 |

The $\Delta a^*$ values shown in Fig. 3.4 decrease with increasing stress in both the AR and PC conditions at all plastic strain amplitudes, varying between 100-300 $b^2$ in the former and 60-200 $b^2$ in the latter. In addition, the linear fit of the Haasen plot data extrapolates to a positive stress value for all material conditions and amplitudes, indicating the presence of a second set of discrete obstacles to dislocation glide that is less responsive to thermal activation than forest dislocations. The intercept on the stress axis, or the athermal stress $\sigma_{ath}$, is approximately 40 MPa in the AR condition at all plastic strain amplitudes, as shown in Fig. 3.4 (a). In contrast, the value of $\sigma_{ath}$ strongly depends on the plastic strain amplitude in the PC condition, as seen in Fig. 3.4 (b), ranging from approximately 0 MPa at 0.8% plastic strain amplitude to 165 MPa at 0.3% plastic strain amplitude.

The fitting parameters in Table 3.1 indicate a steeper slope in the PC compared to the AR condition, suggesting that hydrogen reduces the work of thermal activation for dislocation-dislocation interactions.

### *3.3.2 Dislocation Structures at Half-Life*

To establish a microstructural baseline for comparisons of the hydrogen effects at different levels of applied plastic strain, bright field STEM images of the untested AR and PC specimens were acquired and are shown in Fig. 3.5. The initial strain-hardened microstructures are similar in AR and PC specimens, containing loose dislocation cell walls, dense dislocation tangles and several planar structures.

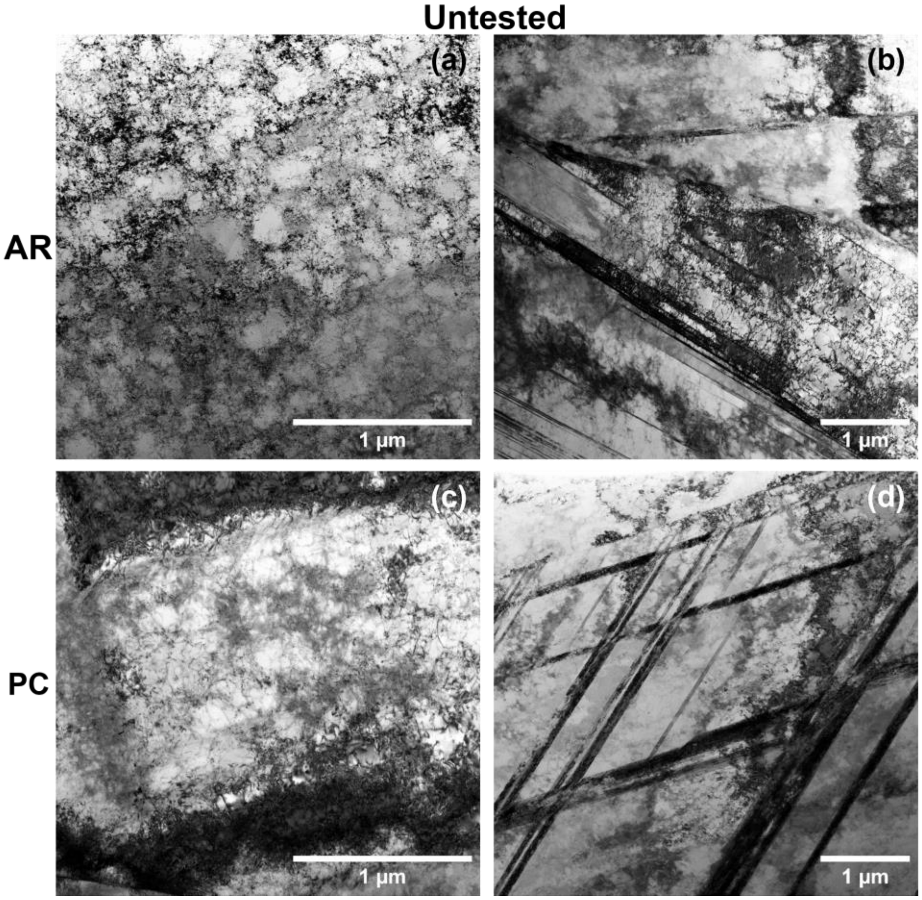

Fig. 3.5: BF-STEM images showing dislocation arrangements and planar structures in (a, b) AR and (c, d) PC specimens in the untested condition.

Figs. 3.6 and 3.7 show the microstructures developed after LCF testing at 0.3% and 0.8% plastic strain amplitudes, respectively, at half-life. In the AR condition, well-defined cells with tight dislocation walls and open interiors are observed at low (Fig. 3.6 (a)) and high (Fig. 3.7 (a, b)) plastic strain amplitudes. In contrast, well-defined dislocation cells are not present in the PC condition at the low amplitude regime (Fig. 3.6 (c)). Instead, there are loose cell walls with dense dislocation interiors and dense dislocation tangles, similar to the configurations inherited from processing (Fig. 3.5 (c)). At high plastic strain amplitude (Fig. 3.7(c)), well-defined dislocation cells are observed in the PC condition, and these are very similar to those observed in the AR condition. Several planar structures are present on both AR and PC specimens at all amplitudes, including the untested condition, as shown in Figs. 3.5-3.7. Although not identified in this work, these planar features are likely to be predominantly planar slip bands, and some stacking faults and deformation twins, reported by others to be formed in this material after cold working and under cyclic loading conditions [31-33].

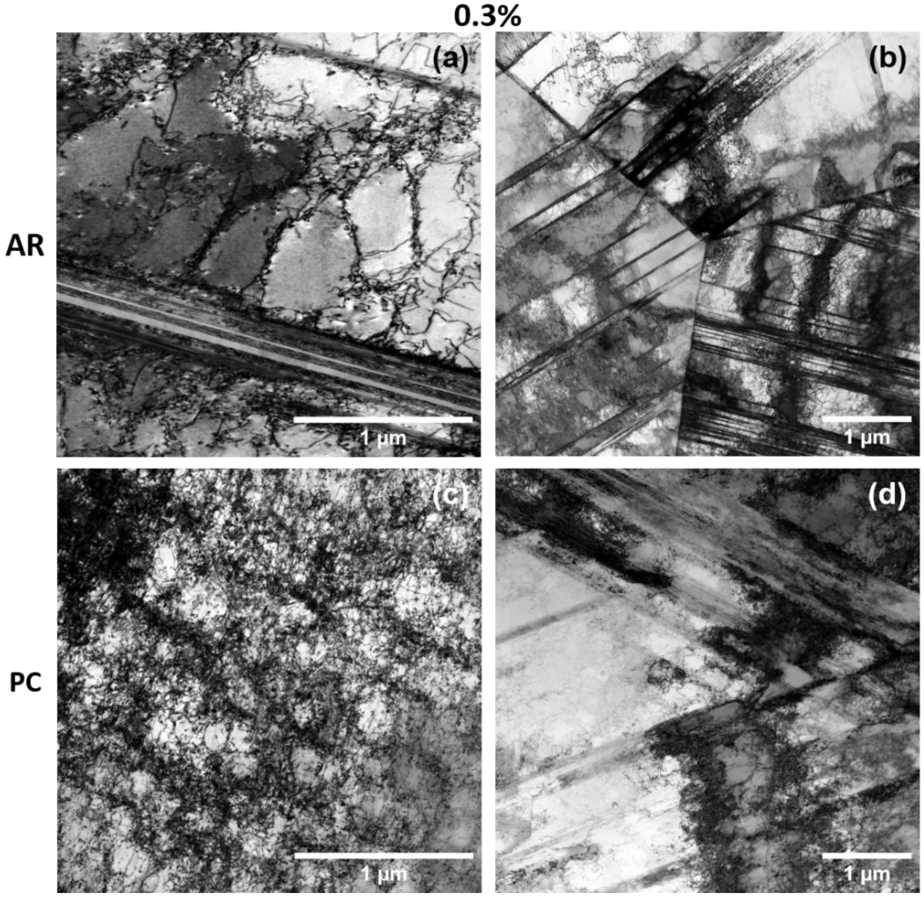

Fig. 3.6: BF-STEM images showing dislocation arrangements and planar structures in (a, b) AR and (c, d) PC specimens after LCF testing at 0.3% plastic strain amplitude.

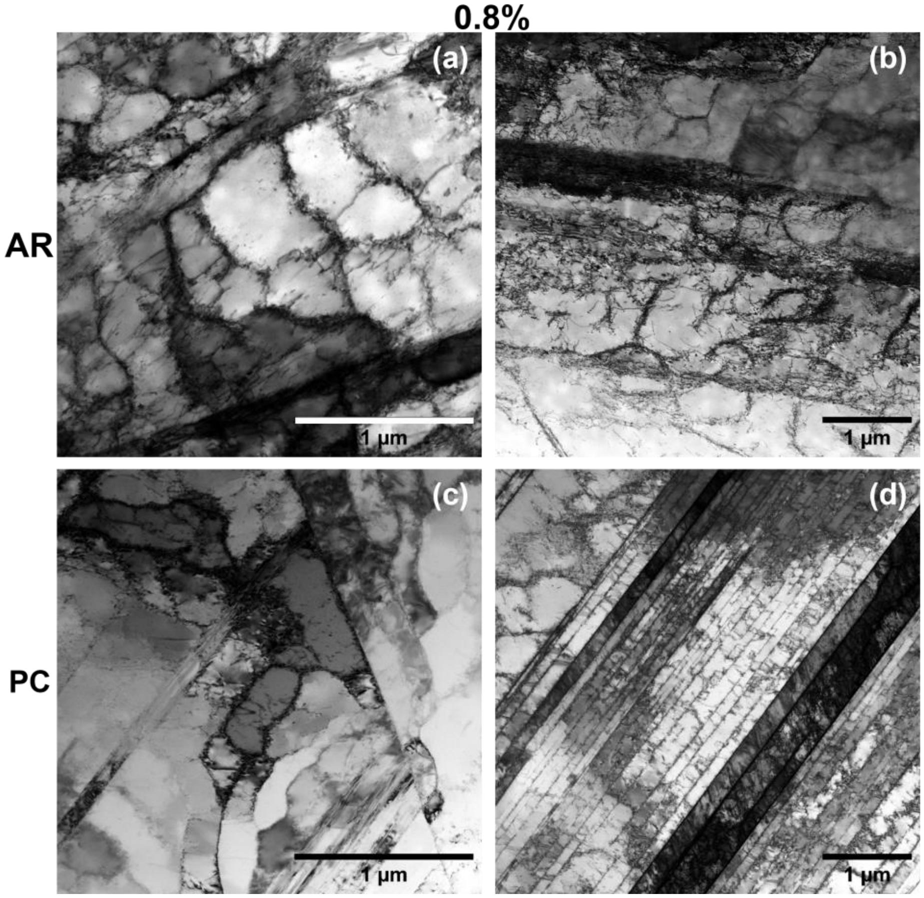

Fig. 3.7: BF-STEM images showing dislocation arrangements and planar structures in (a, b) AR and (c, d) PC specimens after LCF testing at 0.8% plastic strain amplitude.

## 3.4. Discussion

### *3.4.1. Evolution of Operational Activation Area with Cumulative Plastic Strain*

The microstructural development that occurs during cyclic straining is reflected in the changes in flow stress and operational activation area $\Delta a^*$ as the cumulative plastic strain increases. In both AR and PC material conditions and at all plastic strain amplitudes, the peak tension stresses decrease sharply from their strain hardened values during the initial LCF cycles, followed by a region of reduced softening rate that extends to the end of life [12]. The initial increase in $\Delta a^*$ as plastic strain accumulates at a given plastic strain amplitude (Fig. 3.3) correlates with the initial large softening and is attributed to changes in activation distance (obstacle type) and/or obstacle spacing (density) [13]. The constant values of $\Delta a^*$ throughout the region of more gradual softening is consistent with a constant obstacle spacing and type at state of dynamic microstructural equilibrium [30]. A comparison between the $\Delta a^*$ values in AR and PC 316L stainless steel, shown in Fig. 3.3, indicates that hydrogen clearly affects the glide resistance by decreasing $\Delta a^*$ at a given cumulative plastic strain and plastic strain amplitude. Smaller $\Delta a^*$ values in the PC condition are due to hydrogen influencing the activation distance and/or obstacle distribution. However, the changing nature of the microstructure at this stage of the lifetime does not allow for separation of these variables.

It is worth noting that, in complex alloys such as strain-hardened 316L stainless steel, multiple deformation mechanisms are likely to operate simultaneously, and distinguishing their contributions to the total $\Delta a^*$ while the microstructure is evolving is very challenging, especially since the different mechanisms can have similar activations areas. The $\Delta a^*$ values from 50 to 160 $b^2$ across different plastic strain amplitudes in both material conditions reveals that interactions of mobile dislocations with solute atoms are important for thermally activated glide in this material with and without hydrogen during cyclic deformation. This is an expected contribution since annealed stainless steels are primarily strengthened by solute atoms [34]. Kaschner and Gibeling [35] performed plastic strain rate change experiments during LCF tests in annealed 304 stainless steel and reported an increase in $\Delta a^*$ from 90 $b^2$ to 130 $b^2$ as the material was cycled to saturation, which was associated with solute-controlled dislocation glide. Type 316L stainless steel is an alloy with low stacking fault energy, known to deform by planar slip at low plastic strain levels and transition to wavy slip at higher cumulative plastic strains [36-38]. The presence of well-defined dislocation cell structures in AR and PC at half-life, as shown in Figs. 3.6 (a) and 3.7 (a-c), implies that cross slip is an important process for microstructural development in 316L, and its associated glide resistance is likely a contribution to the total $\Delta a^*$ values during the first half of the lifetime. Finally, Fig. 3.5 shows that dense dislocation arrangements were introduced to this steel during processing, making forest dislocations a significant contribution to the total $\Delta a^*$. The linearity of the Hassen plot supports this concept that dislocation-dislocation interactions are important in controlling the rate of cyclic deformation for both the AR and PC conditions.

### *3.4.2. Haasen Plot Analysis*

At half-life, the microstructure is assumed to be in a state of dynamic equilibrium as described by Essmann and Mughrabi [30], which is consistent with the quasi-steady state of the flow stresses observed by Oliveira, *et al.* [12] in the 316L cyclic stress response curves. Consequently, the dependence of flow stress and operational activation area on the obstacle density is isolated at this stage of life and the Haasen plot analysis can be employed to determine the nature of the obstacles controlling the kinetics of dislocation glide [13, 19].

As mentioned in section 3.3.1.2, the analysis of the intercepts in Fig. 3.4 indicates the presence of at least two sets of obstacles influencing the dislocation kinetics in both AR and PC 316L stainless steel. The thermal, or discrete short-range obstacles, are characterized by operational activation areas $\Delta a^*$ and activation work. The athermal, or long-range obstacles, are characterized by athermal stresses $\sigma_{ath}$. Discussions regarding these obstacles and associated dislocation interactions in the AR and PC conditions are presented in the sections below.

#### *3.4.2.1. Thermal Obstacles to Dislocation Glide*

The Haasen plots for the AR and PC conditions in Fig. 3.4 show the linear relationship between the inverse of the operational activation area normalized by the magnitude of the Burgers vector

$b^2/\Delta a^*$ and the true stress expected from the dependence on the spacing between dislocations [13, 19]. In other words, as strain hardening takes place within the stable hysteresis loops, the reduction in $\Delta a^*$ reflects the changes in dislocation spacing.

The plastic strain rate change analysis of Kaschner and Gibeling [35] in annealed 304 stainless steel resulted in $\Delta a^*$ of 300 $b^2$ for dislocation-solute interactions. Sills, Foster and Zhou [39] numerically estimated approximately 90 $b^2$ for solid solute strengthening in 304L stainless steel. The magnitudes of $\Delta a^*$ obtained at half-life for AR 316L across all tested amplitudes (100-300 $b^2$), in addition to the STEM image of the AR microstructures, suggest that the kinetics of glide in this material condition are influenced by dislocation interactions with solutes and forest dislocations on the slip plane and by cross slip. Their individual contributions to the total $\Delta a^*$ are similar in magnitude and sum inversely [19]. That is, the value of $\Delta a^*$ alone cannot be used to unequivocally identify a single mechanism that is rate controlling. The intercept analysis of the Haasen plots shown in Fig. 3.4 reveals that dislocation-dislocation interactions (forest dislocations) control the rate of dislocation glide in cyclic deformation and the rate sensitivity in this strain-hardened alloy at all plastic strain amplitudes. This result implies that the $\Delta a^*$ for overcoming forest dislocations is smaller than that associated with the other thermal obstacles in this material.

Similar to the AR condition, the range of $\Delta a^*$ at half-life in the PC 316L stainless steel (60-200 $b^2$) indicates that the thermal obstacles influencing dislocation glide kinetics at all plastic strain amplitudes are likely solute atoms and forest dislocations, with the latter being more rate sensitive than the former. However, the STEM micrographs showing cell formation (Fig. 3.7 (c)) suggest that cross slip is operative in the PC condition only at high plastic strain amplitudes. At a strain amplitude of 0.3% and at 400 MPa, for example, the presence of hydrogen decreases $\Delta a^*$ by 13% compared to the non-charged condition. At 0.8% strain amplitude and at the same stress level, $\Delta a^*$

is reduced by 32%. Although there may be differences in $\Delta a^*$ due to changes in forest dislocation spacing induced by the presence of hydrogen, the added contribution of cross slip to the total $\Delta a^*$ at high plastic strain amplitude would explain the further reduction in $\Delta a^*$ when compared to the value in the low strain amplitude regime, hence the dependence of $\Delta a^*$ on plastic strain amplitude when hydrogen is present.

Assuming that the only contribution to $\Delta a^*$ among the three identified mechanisms that varies with stress at a given plastic strain amplitude and microstructure arises from dislocation-dislocation interactions, the ratio of changes in $\Delta a^*$ in the PC to the AR condition over a fixed stress interval could be used to estimate the effect of hydrogen on the obstacle spacing. For instance, at 0.3% plastic strain amplitude, $\Delta a^*$ changes by 45 $b^2$ in the AR condition and by 60 $b^2$ in the PC condition over the stress range between 350 MPa to 450 MPa, resulting in a PC:AR ratio of 1.3. At 0.8% strain amplitude and considering the same stress interval, these values are 40 $b^2$ and 25 $b^2$ in the AR and PC material conditions, respectively, and the PC:AR ratio is 0.6. The observation that the PC:AR ratio at a given strain amplitude is different than one means that hydrogen affects the forest dislocation spacing in this stainless steel. Furthermore, if hydrogen only affected the (obstacle) spacing, the ratios between changes in $\Delta a^*$ in the PC and in the AR conditions should be similar at the two strain amplitudes. The fact that this is not the case means that hydrogen affects the activation distance ($\Delta y$) in this material as well.

Sirois and Birnbaum [22] measured operational activation areas during stress relaxation tests in pure Ni and Ni-C alloys after cathodic hydrogen charging. For a stress range between 50 and 250 MPa, they reported a decrease in $\Delta a^*$ by 35-50% in presence of hydrogen in both materials. Wang, *et al.* [25] conducted similar experiments in pure iron, Fe-8Cr alloy and F82 steel and observed a significant decrease in $\Delta a^*$ as the cathodic current density (hence hydrogen concentration) increased. In pure Fe, for example, the $\Delta a^*$ values changed from 270 $b^2$ in the non-charged condition to 30 $b^2$ in the hydrogen charged condition. Additional results led Birnbaum and Sofronis [23] to propose that, under temperature and strain rate conditions that allow for hydrogen atmospheres to form and to move with dislocations, hydrogen reduces the interaction energy between mobile dislocations and other short-range elastic obstacles. As a consequence, a decrease in spacing between dislocations in a pileup in the presence of hydrogen was experimentally observed in 310S stainless steel by Ferreira, *et al.* [24] and numerically simulated in 316L stainless steel by Chateau, *et al.* [40]. Tien, *et al*. [41] investigated hydrogen transport through dislocations in a solute atmosphere arrangement; they used a kinetic model to estimate the critical strain rate for a dislocation to break away from its hydrogen atmosphere at room temperature. Based on an interaction distance of 30 b (long-range motion), dislocation density of $1\text{x}10^{10}$ $\text{cm}^{-2}$ and diffusivity of $1\text{x}10^{-10}$ $\text{cm}^2\text{s}^{-1}$, the critical strain rate for stainless steels is about $1\text{x}10^{-1}$ $\text{s}^{-1}$, implying that hydrogen is likely to move with mobile dislocations during most laboratory testing conditions [41]. These observations support an understanding that the decrease in $\Delta a^*$ observed in the present study for the PC compared to AR conditions at a given cumulative plastic strain and strain amplitude is consistent with hydrogen reducing the stress field of dislocations, affecting the activation (or interaction) distances and decreasing the spacing between dislocation obstacles. The influence of hydrogen is also reflected in the slopes of the Haasen plots (Fig. 3.4). The steeper slope in the PC condition compared to that in the AR condition indicates that hydrogen decreases the work for thermal activation by changing both the obstacle spacing and the activation distance and enhances the rate sensitivity of this material [13].

#### *3.4.2.2. Athermal Obstacles to Dislocation Glide*

The intercept analysis of the Haasen plots in Fig. 3.4 reveals the presence of long-range obstacles to dislocation glide that are less rate sensitive (more athermal) than forest dislocations in both AR and PC conditions of 316L stainless steel. Based on the microstructural features observed in these material conditions prior to (Fig. 3.5) and after cyclic deformation (Figs. 3.6-3.7) and on the Bauschinger analysis reported by Oliveira, *et al.* [12], these athermal obstacles are likely to be dislocation cell walls and dense dislocation tangles.

In the AR condition, well-defined dislocation cells are observed at all plastic strain amplitudes, as shown in Figs. 3.6 (a) and 7 (a, b). Dislocation cells represent heterogeneous deformation structures known to be source of intragranular (local) back stresses [31]. These back stresses, which are a highly directional type of athermal stresses, develop from dislocation segments bowed from the cell walls [42]. In the PC condition, well-defined dislocation cells only develop at high plastic strain amplitudes (Fig. 3.7 (c)), where the large plastic strain levels are sufficient to trigger cross slip. As a result, the $\sigma_{ath}$ values for the PC condition shown in Table 3.1 at plastic strain amplitudes of 0.6% and 0.8% approach the values for the AR condition, reflecting the microstructural similarities between the two conditions. In contrast, $\sigma_{ath}$ for AR and PC differ significantly at low plastic strain amplitudes, consistent with the different microstructures developed at half-life in both material conditions and shown in Fig. 3.6. The stress field associated with the dense dislocation tangles inside the open areas of the (loose) cell structures in the PC condition at this strain amplitude represent an athermal barrier to dislocation glide that is too large for thermal activation. Therefore, the $\sigma_{ath}$ values obtained for the AR and PC material conditions at different plastic strain amplitudes, combined with STEM observations of the microstructures in a state of dynamic microstructural equilibrium at half-life, clearly show that hydrogen affects the microstructural development during low cycle fatigue of 316L stainless steel in addition to influencing the dislocation glide kinetics.

### 3.5. Summary

Plastic strain rate change experiments were conducted during plastic strain-controlled LCF tests in strain-hardened 316L austenitic stainless steel specimens with (PC) and without (AR) hydrogen. In addition to probing the evolution of the operational activation area with cumulative plastic strain, the analysis of the Haasen plots at a microstructural state of dynamic equilibrium provided information about the nature of the dislocation interactions that control the dislocation glide kinetics. The main observations are summarized below:

1. STEM images show the presence of loose dislocation cell walls, dense regions of dislocation tangles and several planar features in the untested (strain-hardened) AR and PC conditions. Dislocation cells with well-defined walls and open interiors are observed at half-life in the AR condition after testing at low (0.3%) and high (0.8%) plastic strain amplitudes. In contrast, the presence of hydrogen decreases the propensity for cross slip in the low strain amplitude regime, and well-defined cellular structures develop in the PC condition only at high (0.8%) plastic strain amplitudes.
2. The evolution of the operational activation area $\Delta a^*$ with cumulative plastic strain and the ranges of $\Delta a^*$ in AR and PC specimens suggest that solute atoms, forest dislocations and cross slip represent thermal obstacles to dislocation glide in the dynamic microstructure. Furthermore, hydrogen decreases the magnitude of $\Delta a^*$ at a given cumulative plastic strain at all plastic strain amplitudes.
3. At a state of dynamic microstructural equilibrium (half-life), the same thermal obstacles are likely to influence the kinetics of dislocation glide in the AR and PC conditions.

However, cross slip only contributes to the deformation of PC specimens at high plastic strain amplitudes when dislocation cell structures are observed. Additionally, the Haasen plot analysis indicates that dislocation-dislocation interactions control the rate of dislocation glide and the rate sensitivity in both AR and PC conditions.

4. Hydrogen affects the glide resistance in 316L stainless steel by decreasing the $\Delta a^*$ values at a given true stress and at all plastic strain amplitudes. This reduction in $\Delta a^*$ is associated with hydrogen decreasing the obstacle (dislocation) spacing and the activation (or interaction) distance. These effects are reflected in steeper slopes in the Haasen plot for the PC condition when compared to that in the AR condition, indicating that hydrogen also enhances the rate sensitivity of this alloy.
5. The Haasen plots reveal the presence of athermal obstacles to dislocation glide in both AR and PC material conditions, likely to be dislocation cell walls for the AR condition at all plastic strain amplitudes and for the PC condition at high strain amplitude where the athermal stress values are similar, and dense dislocation tangles in the PC condition at low plastic strain amplitude. The influence of hydrogen on the microstructural development leads to different values of athermal stress $\sigma_{ath}$ at low and high plastic strain amplitudes in the PC condition.

## Acknowledgements

We would like to thank Ryan Nishimoto for the assistance with the STEM sample preparation. Partial funding for this research was provided by the University of California, Davis and by donations to the Department of Materials Science and Engineering. This work was supported by the Office of Energy Efficiency and Renewable Energy’s H-Mat Energy Materials Network funded through the Hydrogen and Fuel Cell Technologies Office at the U.S. Department of Energy.

Sandia National Laboratories is a multi-mission laboratory managed and operated by National Technology & Engineering Solutions of Sandia, LLC, a wholly owned subsidiary of Honeywell International Inc., for the U.S. Department of Energy's National Nuclear Security Administration under contract DE-NA0003525. This paper describes objective technical results and analysis. Any subjective views or opinions that might be expressed in the paper do not necessarily represent the views of the U.S. Department of Energy or the United States Government.

## References

[1] W. H. Johnson. On Some Remarkable Changes Produced in Iron and Steel by the Action of Hydrogen and Acids. *Nature* 11 (281) (1875) 393-393.

[2] G. Sandoz. A unified theory for some effects of hydrogen source, alloying¦ elements, and potential on crack growth in martensitic AISI 4340 steel. *Metall Trans* 3 (5) (1972) 1169-1176.

[3] S. P. Lynch. Hydrogen embrittlement (HE) phenomena and mechanisms. *Stress Corrosion Cracking: Theory and Practice* (2011) 90-130.

[4] I. M. Robertson, P. Sofronis, A. Nagao, *et al.* Hydrogen Embrittlement Understood. *Metall Mater Trans B* 46 (3) (2015) 1085-1103.

[5] P. J. Gibbs, K. A. Nibur, C. San Marchi. Plastic Ratcheting and Fatigue Crack Formation in Austenitic Steels with Hydrogen. in: B. P. Somerday, P. Sofronis (Eds.), International Hydrogen Conference (IHC 2016): Materials Performance in Hydrogen Environments, *ASME Press*, 2017, pp. 306-315.

[6] N. K. Kuromoto, A. S. Guimaraes, C. M. Lepienski. Superficial and internal hydrogenation effects on the fatigue life of austenitic steels. *Mat Sci Eng A* 381 (1-2) (2004) 216-222.

[7] K. E. Nygren, A. Nagao, S. Wang, *et al.* Influence of internal hydrogen content on the evolved microstructure beneath fatigue striations in 316L austenitic stainless steel. *Acta Mater* 213 (2021).

[8] K. E. Nygren, A. Nagao, P. Sofronis, *et al.* The Role of Microstructure in Hydrogen-Induced Fatigue Failure of 304 Austenitic Stainless Steel. *Metall Mater Trans A* 51 (11) (2020) 5704-5714.

[9] T. Iijima, H. Enoki, J. Yamabe, *et al.* Effect of High Pressure Gaseous Hydrogen on Fatigue Properties of SUS304 and SUS316 Austenitic Stainless Steel. ASME 2018 Pressure Vessels and Piping Conference, 2018.

[10] P. J. Gibbs, C. San Marchi, K. A. Nibur, *et al.* Comparison of Internal and External Hydrogen on Fatigue-Life of Austenitic Stainless Steels. *Proceedings of the ASME 2016 Pressure Vessels and Piping Conference* 6B (2016) 1-8.

[11] T. T. Nguyen, J. Park, S. H. Nahm, *et al.* Ductility and fatigue properties of low nickel content type 316L austenitic stainless steel after gaseous thermal pre-charging with hydrogen. *Int J Hydrog Energy* 44 (51) (2019) 28031-28043.

[12] D. M. Oliveira, C. W. San Marchi, D. L. Medlin, *et al.* The influence of hydrogen on the low cycle fatigue behavior of strain-hardened 316L stainless steel. *Mat Sci Eng A* (2022) 143477.

[13] U. F. Kocks, A. S. Argon, M. F. Ashby. Thermodynamics and Kinetics of Slip. *Prog Mater Sci* 19 (1975) 1-281.

[14] H. Mughrabi. Cyclic Strain Rate Effects in Fatigued Face-Centred and Body-Centred Cubic Metals. *Philos Mag* 93 (28-30) (2013) 3821-3834.

[15] H. Conrad. Thermally Activated Deformation of Metals. *Jom-J Met* 16 (7) (1964) 582-&.

[16] C. Robertson, M. Fivel, A. Fissolo. Dislocation substructure in 316L stainless steel under thermal fatigue up to 650 K. *Mat Sci Eng A* 315 (1-2) (2001) 47-57.

[17] Z. S. Basinski. Thermally activated glide in face-centred cubic metals and its application to the theory of strain hardening. *The Philosophical Magazine: A Journal of Theoretical Experimental and Applied Physics* 4 (40) (1959) 393-432.

[18] J. Bonneville, B. Escaig. Cross-slipping process and the stress-orientation dependence in pure copper. *Acta Metall.* 27 (1979) 1477-1486.

[19] R. A. Mulford. Analysis of Strengthening Mechanisms in Alloys by Means of Thermal-Activation Theory. *Acta Metall* 27 (7) (1979) 1115-1124.

[20] P. Haasen. Plastic Deformation of Nickel Single Crystals at Low Temperatures. *Philos Mag* 3 (28) (1958) 384-418.

[21] A. H. Cottrell, R. J. Stokes. Effects of Temperature on the Plastic Properties of Aluminium Crystals. *Proc R Soc Lon Ser-A* 233 (1192) (1955) 17-34.

[22] E. Sirois, H. K. Birnbaum. Effects of Hydrogen and Carbon on Thermally Activated Deformation in Nickel. *Acta Metall Mater* 40 (6) (1992) 1377-1385.

[23] H. K. Birnbaum, P. Sofronis. Hydrogen-Enhanced Localized Plasticity - a Mechanism for Hydrogen-Related Fracture. *Mat Sci Eng A* 176 (1-2) (1994) 191-202.

[24] P. J. Ferreira, I. M. Robertson, H. K. Birnbaum. Hydrogen effects on the interaction between dislocations. *Acta Mater* 46 (5) (1998) 1749-1757.

[25] S. Wang, N. Hashimoto, Y. M. Wang, *et al.* Activation volume and density of mobile dislocations in hydrogen-charged iron. *Acta Mater* 61 (13) (2013) 4734-4742.

[26] ASTM International. E606-04: Standard Test Method for Strain-Controlled Fatigue Testing. *ASTM International*, West Conshohocken, PA, 2004.

[27] G. C. Kaschner, J. C. Gibeling. Strain rate change transients during cyclic deformation of copper. *Scripta Mater* 35 (12) (1996) 1397-1402.

[28] J. L. Walley, E. J. Lavernia, J. C. Gibeling. Low-Cycle Fatigue of Ultra-Fine-Grained Cryomilled 5083 Aluminum Alloy. *Metall Mater Trans A* 40 (11) (2009) 2622-2630.

[29] S. Suresh. Fatigue of materials. *Cambridge university press*, 1998.

[30] U. Essmann, H. Mughrabi. Annihilation of Dislocations during Tensile and Cyclic Deformation and Limits of Dislocation Densities. *Philos. Mag. A* 40 (6) (1979) 731-756.

[31] M. S. Pham, S. R. Holdsworth, K. G. F. Janssens, *et al.* Cyclic deformation response of AISI 316L at room temperature: Mechanical behaviour, microstructural evolution, physically-based evolutionary constitutive modelling. *Int. J. Plast.* 47 (2013) 143-164.

[32] V. Mazánová, M. Heczko, V. Škorík, *et al.* Microstructure and martensitic transformation in 316L austenitic steel during multiaxial low cycle fatigue at room temperature. *Mater. Sci. Eng., A* 767 (2019) 138407.

[33] X. F. Xie, D. Ning, J. Sun. Strain-controlled fatigue behavior of cold-drawn type 316 austenitic stainless steel at room temperature. *Mater. Charact.* 120 (2016) 195-202.

[34] U. F. Kocks, H. Mecking. Physics and phenomenology of strain hardening: the FCC case. *Prog Mater Sci* 48 (3) (2003) 171-273.

[35] G. C. Kaschner, J. C. Gibeling. A study of the mechanisms of cyclic deformation in f.c.c. metals using strain rate change tests. *Mat Sci Eng A* 336 (1-2) (2002) 170-176.

[36] X. Feaugas. On the origin of the tensile flow stress in the stainless steel AISI 316L at 300 K: Back stress and effective stress. *Acta Mater* 47 (13) (1999) 3617-3632.

[37] Y. F. Li, C. Laird. Cyclic Response and Dislocation Structures of AISI 316L Stainless Steel. Part 2. Polycrystals Fatigued at Intermediate Strain Amplitude. *Mat Sci Eng A* 186 (1-2) (1994) 87-103.

[38] M. Gerland, J. Mendez, P. Violan, *et al.* Evolution of Dislocation-Structures and Cyclic Behavior of a 316l-Type Austenitic Stainless-Steel Cycled Invacuo at Room-Temperature. *Mat Sci Eng A* 118 (1989) 83-95.

[39] R. B. Sills, M. E. Foster, X. W. Zhou. Line-length-dependent dislocation mobilities in an FCC stainless steel alloy. *Int J Plasticity* 135 (2020) 102791.

[40] J. P. Chateau, D. Delafosse, T. Magnin. Numerical simulations of hydrogen-dislocation interactions in fcc stainless steels. Part II: hydrogen effects on crack tip plasticity at a stress corrosion crack. *Acta Mater* 50 (6) (2002) 1523-1538.

[41] J. K. Tien, A. W. Thompson, I. M. Bernstein, *et al.* Hydrogen Transport by Dislocations. *Metall Trans A* 7 (6) (1976) 821-829.

[42] H. Mughrabi. The Long-Range Internal-Stress Field in the Dislocation Wall Structure of Persistent Slip Bands. *Physica Status Solidi a-Applied Research* 104 (1) (1987) 107-120.

# Chapter 4. Influence of Hydrogen on the Low Cycle Fatigue Behavior of the Equiatomic CrMnFeCoNi High Entropy Alloy[3]

## Abstract

True plastic strain-controlled low cycle fatigue (LCF) tests were performed on the CrMnFeCoNi high-entropy alloy in the non-charged and hydrogen-precharged (H-precharged) conditions. Internal hydrogen increases the cyclic strength of this alloy at all plastic strain amplitudes by enhancing the effective component of the flow stresses. These effective stresses are greater than back stresses for all tested conditions. Furthermore, the evolution of back stresses during LCF testing at different strain amplitudes is not influenced by the presence of hydrogen, suggesting that the dislocation structures are similar in non-charged and H-precharged conditions. Primary fatigue crack(s) initiate earlier in the H-precharged than in the non-charged condition, and the presence of hydrogen severely reduces the LCF lifetime of this alloy. Fracture surface observations reveal that, although plastic deformation processes are active in the H-precharged condition, hydrogen leads to intergranular failure in the CrMnFeCoNi alloy.

**Keywords**: Low Cycle Fatigue; Hydrogen; High Entropy Alloy; Bauschinger Stresses; Intergranular Failure.

---

[3] To be submitted as D. M. Oliveira, C. W. San Marchi, E. P. George, and J. C. Gibeling. *Scripta Mater.* (2023).

## 4.1. Introduction

High entropy alloys (HEAs) represent a new design concept for metallic materials where compositions toward the center of the phase diagrams are explored for potentially improved properties [1-3]. One of the most extensively studied HEA compositions is the equimolar CrMnFeCoNi alloy, also known as the Cantor alloy [4]. It has been shown to possess excellent damage tolerance at low temperature [5-8], while retaining good tensile strength and ductility at room temperature [7]. In addition, several studies of fatigue crack growth [9, 10], high cycle fatigue [11, 12] and low cycle fatigue [13-16] in the Cantor alloy at room temperature have suggested superior fatigue performance compared to that of conventional austenitic stainless steels. This good combination of tensile and fatigue properties has increased interest in investigating the performance of this alloy in extreme environments, such as in the presence of hydrogen for energy-related applications.

Luo, Li and Raabe [17] reported the tensile deformation behavior of the CrMnFeCoNi alloy after electrochemical charging to hydrogen concentrations between 8 and 33 wt. ppm. They observed that hydrogen led to an increase in strength and ductility in this material at all hydrogen concentrations due to an increase in propensity for nanotwin formation. They also noted that the improved ductility in the presence of hydrogen is unique to the Cantor alloy when compared to other conventional alloys, such as Inconel 718 and 310 stainless steel, with similar or lower hydrogen concentrations. Zhao, *et al.* [18] conducted gaseous and electrochemical hydrogen charging followed by nanoindentation and tensile testing of CrMnFeCoNi alloys with hydrogen concentrations of 76.5 wt. ppm and 45 wt. ppm, respectively. A very small reduction in ductility (~5%) in the gaseous charged condition compared to the non-charged condition was observed, with no significant change in strength. In contrast, absorbed hydrogen substantially increased the hardness and decreased the plasticity in electrochemically charged specimens when compared to the non-charged condition. The authors [18] ascribed these differences to the different hydrogen distributions (gradients from the surface to the interior) produced by the two charging methods and their influence on the activation of hydrogen-induced changes in plasticity mechanisms. Zhou, Tehranchi and Curtin [19] performed theoretical predictions of the ductile-to-brittle transition in different families of stainless steels and HEAs as a function of hydrogen concentrations, based on the idea that hydrogen induces changes in dislocation emission and blunting processes at crack tips. These authors showed that the CrMnFeCoNi alloy is less susceptible to hydrogen embrittlement than 304 austenitic stainless steel but more than 316L, indicating that the compositional complexity of HEAs does not necessarily result in superior performance in hydrogen environments compared to austenitic stainless steels. Instead, the embrittlement phenomenon is more closely related to the hydrogen concentration and distribution in the material. In fact, other papers have reported a severe decrease in ductility and brittle failure in the CrMnFeCoNi alloy under tensile experiments with higher hydrogen concentrations [20-23].

The studies mentioned above reveal some conflicting results and suggest that further research is necessary to understand the effect(s) of hydrogen on the mechanical behavior of the Cantor alloy at different hydrogen concentrations and testing conditions. Although hydrogen energy systems are often subjected to repeated pressurization and depressurization cycles, there are limited studies of the fatigue (crack growth) behavior of this material in the presence of hydrogen [24], and none under strain-controlled low cycle fatigue (LCF) testing conditions. Because plastic strain is known to correlate with damage accumulation and failure under cyclic loading [25], strain-controlled LCF tests would help elucidate the influence of hydrogen on these processes. Therefore, the goal of the current study is to explore the fatigue deformation and failure of the CrMnFeCoNi alloy, with and without internal hydrogen, measured through true plastic strain-controlled LCF tests.

## 4.2. Materials and Methods

The CrMnFeCoNi alloy investigated in this work was arc melted, drop cast and homogenized in vacuum at 1473 K for 24h, using procedures roughly similar to those described by Otto, *et al.* [7]. After homogenization, the 25.4 mm diameter × 127 mm long cylindrical ingots were inserted into tight-fitting holes drilled in stainless steel cans, their back faces welded shut with stainless steel plates, and the combination extruded at 1273 K at an (area) extrusion ratio of 9:1, resulting in an extrusion ratio for the CrMnFeCoNi alloy in the range of 6:1 to 7:1. Cylindrical LCF specimens with 3.2 mm of gage diameter and 10.2 mm of gage length were machined from the extruded rod using a CNC lathe, following the design specified by the ASTM E606 standard [26]. The gage sections were mechanically ground using SiC paper, then diamond compound was used for fine polishing down to 0.25 µm. Each polishing step started along the circumferential direction, and the resulting marks on the surface were eliminated by repeating the same grade of SiC or diamond along the longitudinal direction. The polished specimens were vacuum annealed at 1173 K for 1h, followed by furnace cooling. The resulting microstructure is shown in Fig. 4.1 and consists of recrystallized equiaxed grains with an average grain size of 31 µm and a relatively high density of annealing twins. Additionally, a low concentration of Cr and Mn-rich particles (black spots in Fig. 4.1) approximately 4 µm in diameter was identified using energy dispersive x-ray spectroscopy (EDS).

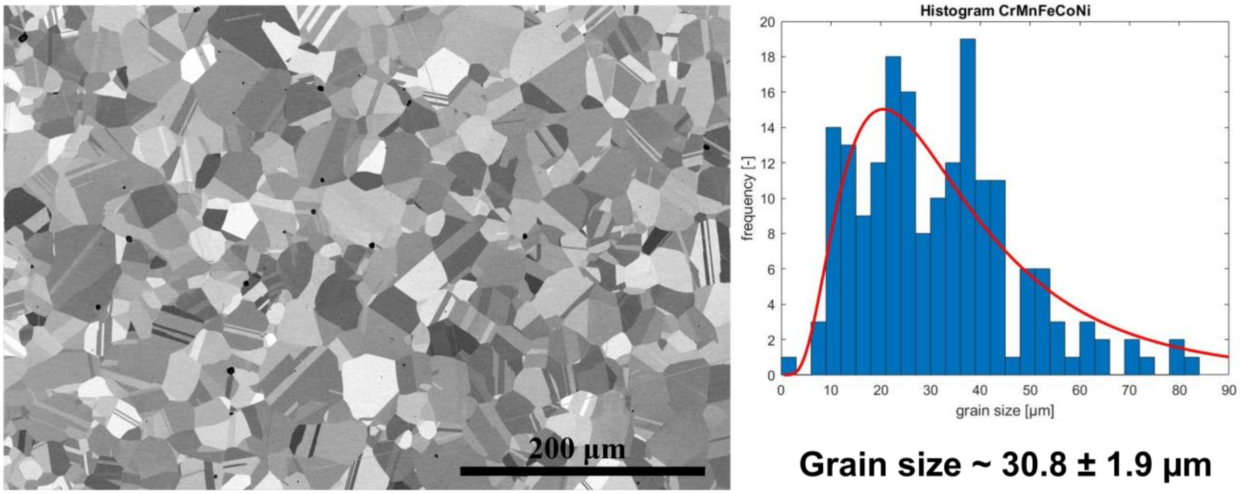

Fig. 4.1: Backscattered electron micrograph of the initial grain morphology obtained after recrystallization. The grain size distribution is shown inset.

Hydrogen-precharging of annealed CrMnFeCoNi specimens was conducted in a chamber containing gaseous hydrogen at a pressure of 138 MPa and at a temperature of 573 K for 13 days. The final concentration of hydrogen in the precharged (H-precharged) specimens was 87 wt. ppm, measured through inert gas fusion-infrared absorbance. The non-charged and H-precharged specimens are referred to here as HEA and H-HEA, respectively. While other studies suggest that this alloy is able to accommodate a higher concentration of hydrogen than conventional austenitic stainless steels [18, 21], the opposite was found here. The hydrogen concentration in strain-hardened 316L stainless steel after gaseous charging at the same thermal environment as described above was 155 wt. ppm [25], almost twice the value measured in the CrMnFeCoNi alloy. This difference may be due to the different initial dislocation densities of these two materials.

True plastic strain-controlled LCF tests were conducted under fully reversed mode (ratio of minimum to maximum plastic strain R = -1) on an MTS 810 servo-hydraulic testing machine running MTS TestStar and Testware-SX software codes adapted from Walley, *et al.* [27]. The control variable, true plastic strain ($\varepsilon_p$), was calculated in real time (Eq. (4.1)) using the measured load ($L$), the total strain ($e_t$) determined from an extensometer attached to the specimen, the initial cross sectional area ($A_o$) and the elastic modulus ($E$).

$$\varepsilon_p = \ln(1 + \mathrm{e}_t) - (1 + \mathrm{e}_t) \times \frac{L}{A_o \times E} \qquad \text{Eq. (4.1)}$$

The LCF tests were performed at room temperature and at a constant plastic strain rate of 1x10$^{-3}$ s$^{-1}$, probing plastic strain amplitudes of 0.3, 0.4, 0.6 and 0.8%. To increase statistical significance, two tests were conducted at each plastic strain amplitude. Failure was defined here as the number of cycles necessary to fracture the specimens or to induce a 20% drop in peak tension stress compared to peak compression stress, whichever was reached first. More details on the LCF test configuration are reported elsewhere [25]. The collected stress-plastic strain data were used to calculate the Bauschinger stresses considering the reverse yield strength as the stress at a true plastic strain offset of 0.1%. In addition, the changes in the slope of the tensile elastic unloading throughout the test were used to estimate the fatigue crack initiation lifetime. Details on these procedures are also reported elsewhere [25]. To evaluate the effect of hydrogen on the crack path and fracture mode, fracture surfaces were characterized using a Thermo Fisher Quattro S scanning electron microscope (SEM) operating at an accelerating voltage of 10-15 kV in the secondary electron imaging mode.

### 4.3. Results and Discussion

Fig. 4.2 shows representative hysteresis loops obtained for the alloy with and without hydrogen (H-HEA and HEA, respectively) at plastic strain amplitudes of (a) 0.3% and (b) 0.8% during the first cycle. These loops illustrate typical changes in stress as the plastic strain increases within a cycle. For the HEA alloy, loops are well formed and symmetric along the plastic strain axis at all plastic strain amplitudes. In contrast, the stress-strain response in H-HEA is characterized by serrated flow during the initial cycle. This effect is especially dramatic under plastic strain control as the machine attempts to maintain the constant true plastic strain rate in the presence of rapid changes in load (as represented in Eq. (4.1)). Serrated flow is often observed in ranges of temperature and strain rate in which mobile dislocations are pinned by solute atoms [28]. When the dislocations break away, the solute mobilities are high enough to allow them to catch up with and re-pin the dislocations, suggesting that this serrated behavior likely arises from periodic dislocation pinning by hydrogen atoms in the H-HEA condition. Serrated flow was present at all plastic strain amplitudes in the forward and reverse direction, although less severe at 0.8% (Fig. 4.2 (b)) due to the larger driving forces for dislocation motion at this amplitude. Furthermore, the serrations disappeared after the first cycle, as shown in the hysteresis loops for the third cycle in Fig. 4.2 (c-d), and this change is most likely a consequence of an increase in dislocation density as the material hardens during the early stages of cyclic deformation (i.e., the available solutes are insufficient to pin all the mobile dislocations).

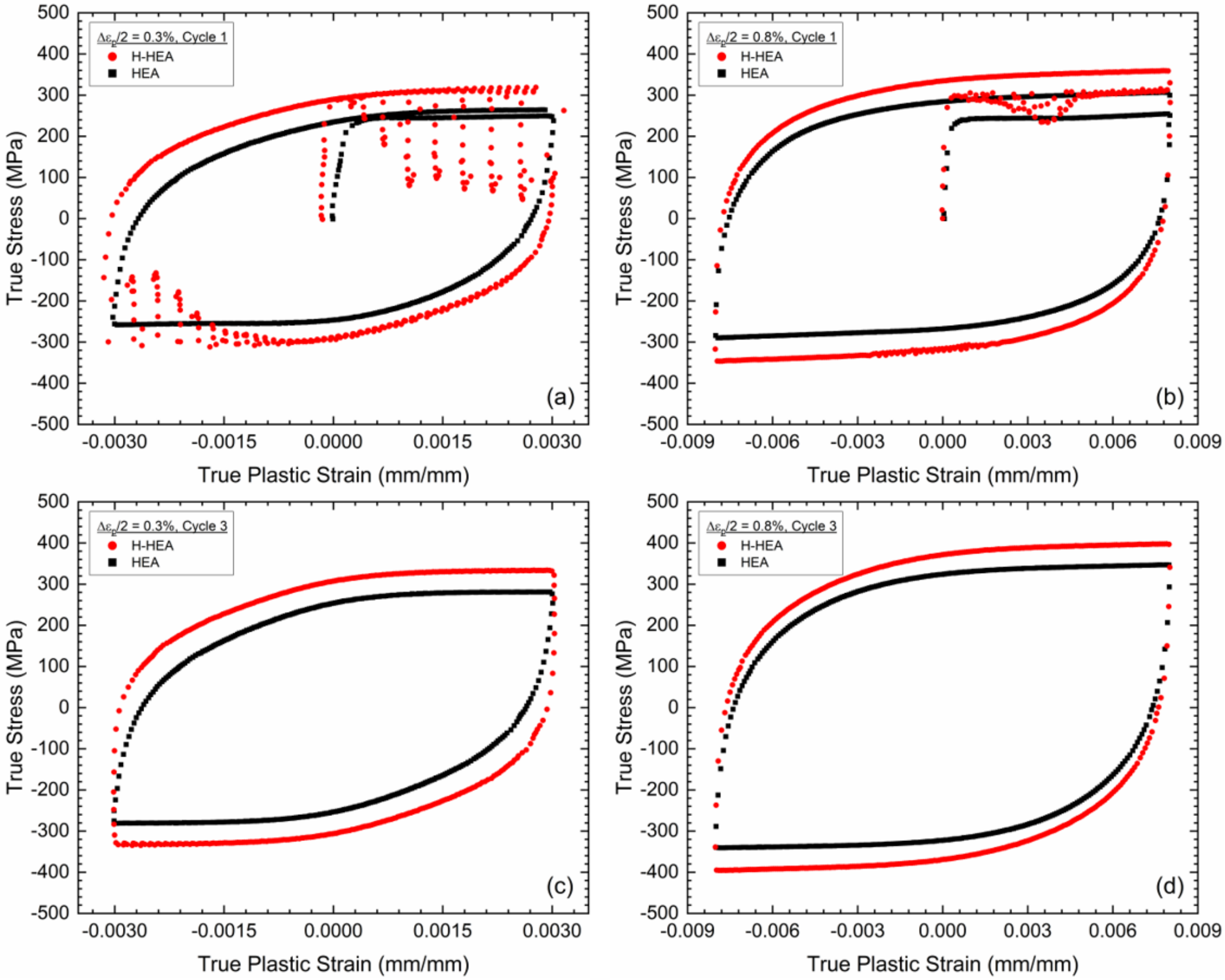

Fig. 4.2: True stress-true strain hysteresis loops for the HEA and H-HEA material conditions at the (a, b) first and (c, d) third cycles obtained during LCF tests at (a, c) 0.3% and (b, d) 0.8% plastic strain amplitudes.

Fig. 4.3 (a) shows the cyclic tension stress response curves for the HEA and H-HEA specimens tested at plastic strain amplitudes between 0.3% and 0.8%. For both material conditions, there is an initial hardening during the first cycles, commonly attributed to dislocation multiplication events in the annealed microstructure [29]. After reaching a peak value of cyclic stress, softening takes place in both the HEA and H-HEA, followed by a region of stress saturation in the HEA. The softening and saturation stages encompass most of the lifetimes for both conditions. It is clear that hydrogen increases the strength of this alloy at all plastic strain amplitudes; peak stresses are 10-20% larger in H-HEA compared to HEA specimens.

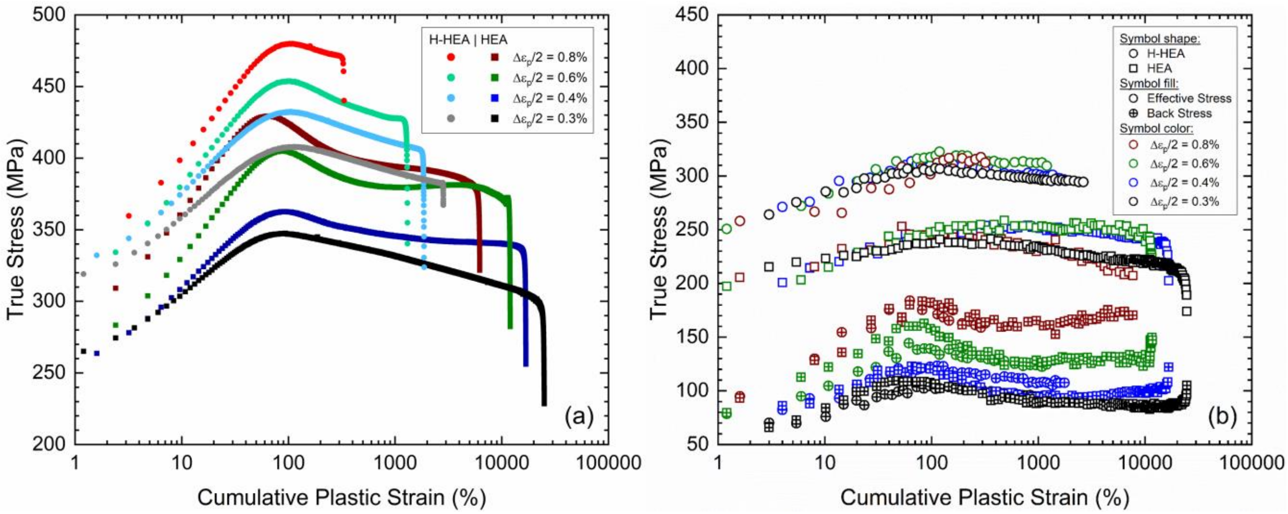

Fig. 4.3: (a) Cyclic tension stress response curves and (b) Bauschinger stresses as a function of cumulative plastic strain for the HEA (squares) and H-HEA (circles) conditions. Different colors represent different plastic strain amplitudes. Only one test for each condition is shown for clarity.

The effective and back stress components of the peak tension stresses were determined as a function of cumulative plastic strain for both the H-precharged and non-charged material conditions. Fig. 4.3 (b) shows that the effective stresses are greater than the back stresses in both material conditions and at all strain amplitudes. This result differs from that reported by Lu, *et al.* [30] at similar plastic strain amplitudes, most likely due to difference in testing mode (total strain vs plastic strain control), which may influence the evolution of these quantities as well as determination of reverse yield strength, and slight differences in grain sizes, which influence yield strength. The high values of peak stresses observed in both material conditions at high strain amplitudes are attributed primarily to the increase in back stresses with plastic strain amplitude, consistent with findings of Lu, *et al.* [30] for total strain-controlled tests. However, there are no differences in back stresses between the HEA and H-HEA conditions at a given plastic strain amplitude, implying that hydrogen does not affect the microstructure that develops during the course of the test.

In addition, this analysis suggests that the hydrogen-induced strengthening (Fig. 4.3 (a)) is represented by the increasing magnitude of the effective component of the flow stress in H-HEA. In other words, hydrogen introduces short-range interactions between dislocations and solutes, which provides additional glide resistance reflected in the effective stresses. The difference in effective stresses between HEA and H-HEA at different plastic strain amplitudes remains approximately constant at about 50 MPa as illustrated in Fig. 4.3 (b), implying that the effect of hydrogen on the evolution of the effective stresses is independent of the plastic strain amplitude and the contribution of hydrogen to strengthening is the same for all plastic strain amplitudes.

Shams, *et al.* [14] conducted total strain-controlled LCF tests in the CrMnFeCoNi alloy and characterized the deformation structures developed at different stages of the lifetime under a plastic strain amplitude of 0.7%. The authors observed stacking faults and traces of planar slip in this alloy during the early stage of cyclic deformation. As the tests progressed, dislocation cells and mechanical twins evolved in the microstructure. Lu, *et al.* [13] reported the presence of well-developed substructures in the CrMnFeCoNi alloy after LCF testing at a total strain amplitude of 0.7%, such as dislocation walls, veins and labyrinths. At a strain amplitude of 0.3%, planar slip bands were the predominant deformation structures observed after failure in this material [13]. Based on these reported fatigue microstructures and recognizing that the back stresses characterize the evolution of the dislocation microstructure, the back stresses measured in the present study reflect well-defined dislocation walls and cell structures that develop similarly with and without internal hydrogen.

Despite strengthening the CrMnFeCoNi alloy, hydrogen severely degrades its LCF lifetime at all plastic strain amplitudes, as observed from the strain-life plots for the HEA and H-HEA specimens shown in Fig. 4. On average, the presence of hydrogen decreases the number of cycles to failure by factors of approximately 5 and 15 at plastic strain amplitudes of 0.3% and 0.8%, respectively. The strain-life data were fitted to a power law in the form of the Coffin-Manson equation [31, 32] shown in Eq. (4.2) and represented by the dashed lines in Fig. 4.4.

$$\frac{\Delta\varepsilon_p}{2} = \varepsilon_f' \left(2N_f\right)^c \qquad \text{Eq. (4.2)}$$

The values of the fatigue ductility coefficient ($\varepsilon_f'$) and fatigue ductility exponent ($c$) for each material condition are also given in Fig. 4.4 near the respective data. The fitting parameters obtained in this study for the CrMnFeCoNi alloy are consistent with those reported by Shams, *et al.* [14]. Since $\varepsilon_f'$ is often approximately equal to the monotonic true fracture ductility [29], these strain-life data suggest that the monotonic tensile ductility of the H-precharged alloy is greatly reduced when compared to that of its non-charged counterpart. This observation is consistent with the results of the tensile behavior of H-precharged CrMnFeCoNi alloy showing a reduction in monotonic strain to failure of 35-60% when similar or larger hydrogen concentrations are added [20-23]. In contrast, lower concentrations of hydrogen have led to a very small decrease (~ 5%) or even a slight increase (~1% to 6%) in ductility in the CrMnFeCoNi alloy when compared to the non-charged condition [17, 18]. Fig. 4.4 also shows estimations of fatigue crack initiation lifetime based on changes in the elastic unloading slope throughout the LCF test [25]. On average across the tested plastic strain amplitudes, crack initiation takes approximately 93% and 73% of total lifetime in HEA and H-HEA, respectively. This result indicates that primary fatigue cracks are initiated much earlier in presence of internal hydrogen, consistent with the loss of ductility in the

H-HEA condition affecting its ability to accommodate plastic deformation. Furthermore, although the fraction of lifetime corresponding to crack growth to failure is larger in the H-HEA condition, the absolute number of cycles is still much smaller than in the HEA material. Finally, we note that the different slopes of the fatigue life plots (Fig. 4.4) suggest that the data may converge at low plastic strain amplitudes; in other words, if the trend continues, internal hydrogen may have little effect in the high cycle regime.

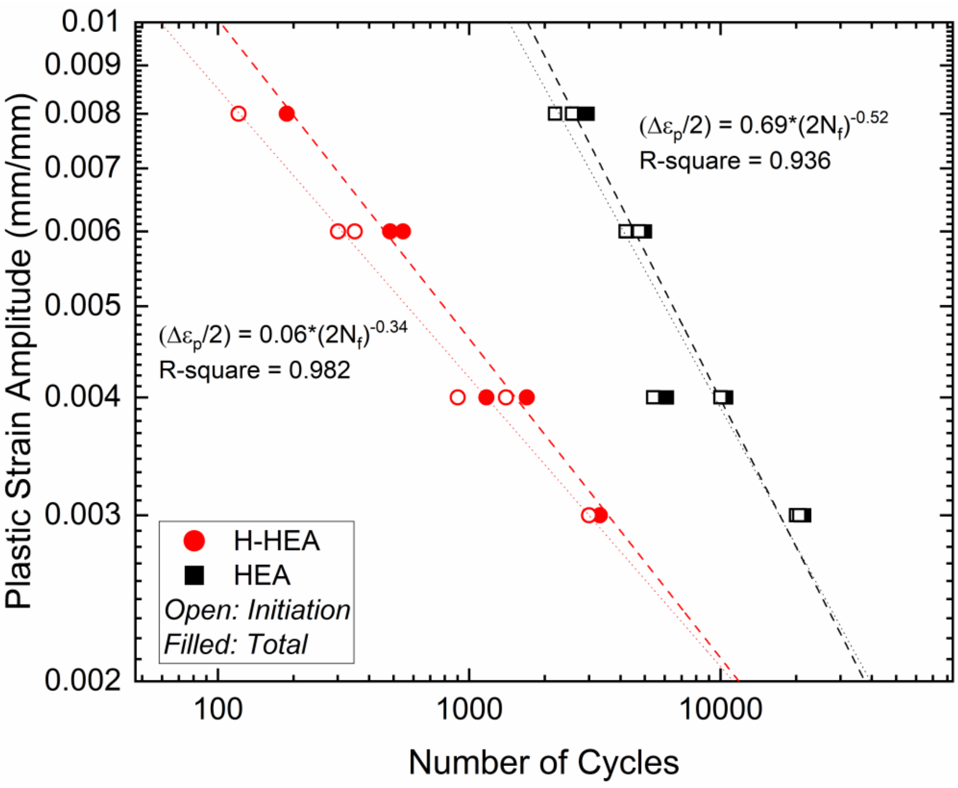

Fig. 4.4: Strain-life plots containing initiation (open symbols) and total (filled symbols) lifetime data for HEA and H-HEA material conditions.

SEM characterization of the fracture surfaces was conducted to probe the changes in fracture mode and crack path induced by the presence of internal hydrogen; these surfaces are depicted in Fig. 4.5. In the HEA specimens, fracture was mainly transgranular and fatigue striations can be seen in the crack propagation area at both (a) 0.3% and (b) 0.8% plastic strain amplitudes, which are characteristic of fatigue crack growth in ductile materials [29, 33]. On the other hand, the failure mode in the H-HEA condition at both (c) 0.3% and (d) 0.8% plastic strain amplitudes transitions to intergranular, as commonly observed in brittle solids [29, 33]. This is a clear indication that hydrogen severely embrittles the CrMnFeCoNi alloy under the current fatigue testing conditions and hydrogen concentration. Despite the brittle fracture features, Fig. 4.5 shows fine slip traces on the grain boundary surfaces of H-HEA after LCF testing at (e) 0.3 and (f) 0.8% plastic strain amplitudes, demonstrating that cyclic plastic deformation is active in the presence of hydrogen, presumably by dislocation glide on primary slip systems.

Bertsch *et al.* [21] systematically investigated the influence of hydrogen on the microstructural development in the CrMnFeCoNi alloy during slow strain rate tensile tests and the relationship between plasticity-mediated processes and intergranular failure observed in the H-precharged condition. Electron backscattered diffraction (EBSD) orientation maps revealed large orientation deviations in the center of the grains and along grain boundaries in the H-precharged specimens. In contrast, more uniform orientation deviations were found inside the grains in the non-charged condition. Combining these results with scanning transmission electron microscopy (STEM) observations of deformation structures formed underneath the fracture surfaces, the authors concluded that hydrogen limits the ability of the CrMnFeCoNi alloy to accommodate plastic deformation, leading to strain incompatibilities across the grain boundaries. Hydrogen-enhanced accumulation of strain at grain boundaries provides an explanation for the intergranular fracture mode observed in H-HEA in the present study and shown in Fig. 4.5 (c-f). The importance of plasticity in the hydrogen-enhanced intergranular fracture process is supported by the slip traces observed on grain boundary surfaces as shown in Fig. 4.5 (e-f).

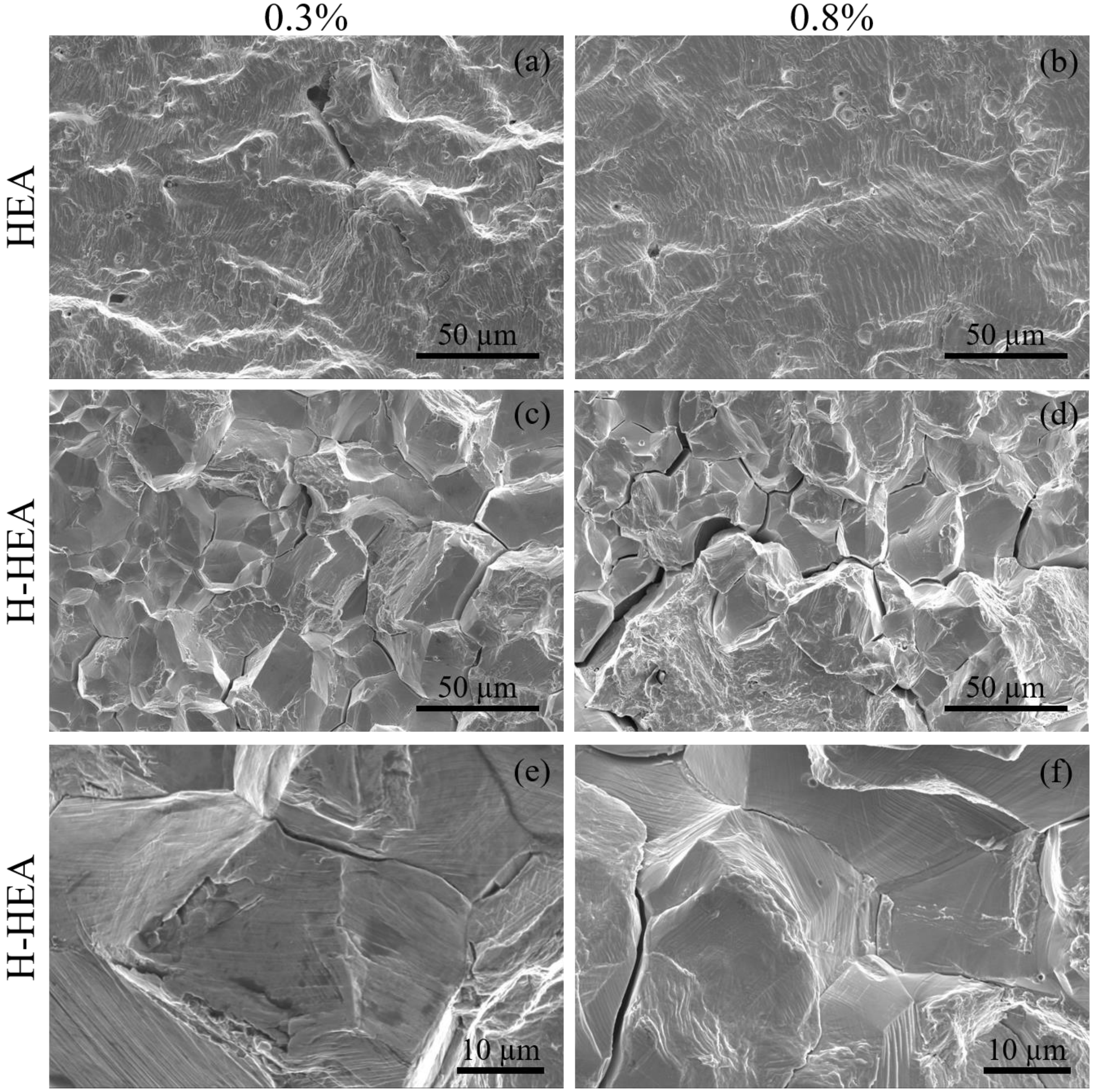

Fig. 4.5: SEM micrographs of the fracture surfaces in (a, b) HEA and (c-f) H-HEA after LCF testing at (a, c, e) 0.3 % and (b, d, f) 0.8% plastic strain amplitudes.

## 4.4. Summary

In summary, the fatigue behavior of the CrMnFeCoNi high entropy alloy in the H-precharged and non-charged conditions was investigated through true plastic strain-controlled LCF tests at plastic strain amplitudes between 0.3% and 0.8%. Serrated flow was observed in the presence of internal hydrogen in the first cycle, likely due to hydrogen pinning the mobile dislocations. Internal hydrogen increases the cyclic strength of the CrMnFeCoNi alloy at all plastic strain amplitudes. This strengthening is attributed to greater effective stresses in the H-precharged condition compared to the non-charged condition, suggesting that dislocation glide in this alloy is affected by hydrogen. In addition, back stresses are similar in both material conditions for each tested amplitude, implying that hydrogen does not alter microstructural development in the CrMnFeCoNi alloy. Hydrogen accelerates the formation of a primary crack(s) and severely decreases the LCF resistance of this alloy under the current testing conditions and hydrogen concentration. Furthermore, hydrogen leads to a transition from ductile fatigue crack growth to more brittle, plasticity-mediated intergranular fracture in the material. The observation of intergranular cracks and slip traces on exposed grain boundaries in the H-precharged condition is consistent with the view that hydrogen enhances strain incompatibility between neighboring grains.

## Acknowledgments

Partial funding for this research was provided by the University of California, Davis and by donations to the Department of Materials Science and Engineering. The Thermo Fisher Quattro S SEM was funded through the US National Science Foundation under award DMR-1725618. This work was supported by the U.S. Department of Energy, Office of Science, Basic Energy Sciences, Materials Sciences and Engineering Division (E.P.G.) and the Office of Energy Efficiency and Renewable Energy's H-Mat Energy Materials Network funded through the Hydrogen and Fuel Cell Technologies Office at the U.S. Department of Energy (C.W.S.M.). Sandia National Laboratories is a multi-mission laboratory managed and operated by National Technology & Engineering Solutions of Sandia, LLC, a wholly owned subsidiary of Honeywell International Inc., for the U.S. Department of Energy's National Nuclear Security Administration under contract DE-NA0003525. This paper describes objective technical results and analysis. Any subjective views or opinions that might be expressed in the paper do not necessarily represent the views of the U.S. Department of Energy or the United States Government. Research at Oak Ridge National Laboratory (materials synthesis and processing) was supported by the U.S. Department of Energy, Office of Science, Basic Energy Sciences, Materials Sciences and Engineering Division.

## References

[1] D. B. Miracle, O. N. Senkov. A critical review of high entropy alloys and related concepts. *Acta Mater.* 122 (2017) 448-511.
[2] E. P. George, D. Raabe, R. O. Ritchie. High-entropy alloys. *Nat. Rev. Mater.* 4 (8) (2019) 515-534.
[3] E. P. George, W. A. Curtin, C. C. Tasan. High entropy alloys: A focused review of mechanical properties and deformation mechanisms. *Acta Mater.* 188 (2020) 435-474.
[4] B. Cantor, I. T. H. Chang, P. Knight, *et al.* Microstructural development in equiatomic multicomponent alloys. *Mater. Sci. Eng., A* 375-377 (2004) 213-218.
[5] B. Gludovatz, A. Hohenwarter, D. Catoor, *et al.* A fracture-resistant high-entropy alloy for cryogenic applications. *Science* 345 (6201) (2014) 1153-1158.
[6] A. Gali, E. P. George. Tensile properties of high- and medium-entropy alloys. *Intermetallics* 39 (2013) 74-78.
[7] F. Otto, A. Dlouhy, C. Somsen, *et al.* The influences of temperature and microstructure on the tensile properties of a CoCrFeMnNi high-entropy alloy. *Acta Mater.* 61 (15) (2013) 5743-5755.
[8] G. Laplanche, A. Kostka, O. M. Horst, *et al.* Microstructure evolution and critical stress for twinning in the CrMnFeCoNi high-entropy alloy. *Acta Mater.* 118 (2016) 152-163.
[9] K. V. S. Thurston, B. Gludovatz, A. Hohenwarter, *et al.* Effect of temperature on the fatigue-crack growth behavior of the high-entropy alloy CrMnFeCoNi. *Intermetallics* 88 (2017) 65-72.
[10] K. V. S. Thurston, B. Gludovatz, Q. Yu, *et al.* Temperature and load-ratio dependent fatigue-crack growth in the CrMnFeCoNi high-entropy alloy. *J. Alloys Compd.* 794 (2019) 525-533.
[11] Y. K. Kim, G. S. Ham, H. S. Kim, *et al.* High-cycle fatigue and tensile deformation behaviors of coarse-grained equiatomic CoCrFeMnNi high entropy alloy and unexpected hardening behavior during cyclic loading. *Intermetallics* 111 (2019).
[12] Y. Z. Tian, S. J. Sun, H. R. Lin, *et al.* Fatigue behavior of CoCrFeMnNi high-entropy alloy under fully reversed cyclic deformation. *J. Mater. Sci. Technol.* 35 (3) (2019) 334-340.
[13] K. J. Lu, A. Chauhan, A. S. Tirunilai, *et al.* Deformation mechanisms of CoCrFeMnNi high-entropy alloy under low-cycle-fatigue loading. *Acta Mater.* 215 (2021).

[14] S. A. A. Shams, G. Jang, J. W. Won, *et al.* Low-cycle fatigue properties of CoCrFeMnNi high-entropy alloy compared with its conventional counterparts. *Mater. Sci. Eng., A* 792 (2020).

[15] S. Picak, T. Wegener, S. V. Sajadifar, *et al.* On the low-cycle fatigue response of CoCrNiFeMn high entropy alloy with ultra-fine grain structure. *Acta Mater.* 205 (2021).

[16] A. G. Wang, X. H. An, J. Gu, *et al.* Effect of grain size on fatigue cracking at twin boundaries in a CoCrFeMnNi high-entropy alloy. *J. Mater. Sci. Technol.* 39 (2020) 1-6.

[17] H. Luo, Z. M. Li, D. Raabe. Hydrogen enhances strength and ductility of an equiatomic high-entropy alloy. *Sci. Rep.* 7 (2017).

[18] Y. Zhao, D. H. Lee, M. Y. Seok, *et al.* Resistance of CoCrFeMnNi high-entropy alloy to gaseous hydrogen embrittlement. *Scr. Mater.* 135 (2017) 54-58.

[19] X. Zhou, A. Tehranchi, W. A. Curtin. Mechanism and Prediction of Hydrogen Embrittlement in fcc Stainless Steels and High Entropy Alloys. *Phys. Rev. Lett.* 127 (17) (2021).

[20] K. Ichii, M. Koyama, C. C. Tasan, *et al.* Comparative study of hydrogen embrittlement in stable and metastable high-entropy alloys. *Scr. Mater.* 150 (2018) 74-77.

[21] K. M. Bertsch, K. E. Nygren, S. Wang, *et al.* Hydrogen-enhanced compatibility constraint for intergranular failure in FCC FeNiCoCrMn high-entropy alloy. *Corros. Sci.* 184 (2021).

[22] K. E. Nygren, K. M. Bertsch, S. Wang, *et al.* Hydrogen embrittlement in compositionally complex FeNiCoCrMn FCC solid solution alloy. *Curr Opin Solid St M* 22 (1) (2018) 1-7.

[23] M. Koyama, K. Ichii, K. Tsuzaki. Grain refinement effect on hydrogen embrittlement resistance of an equiatomic CoCrFeMnNi high-entropy alloy. *Int. J. Hydrogen Energy* 44 (31) (2019) 17163-17167.

[24] M. Koyama, S. Mizumachi, E. Akiyama, *et al.* Hydrogen-accelerated fatigue crack growth of equiatomic Fe–Cr–Ni–Mn–Co high-entropy alloy evaluated by compact tension testing. *Mater. Sci. Eng., A* (2022) 143394.

[25] D. M. Oliveira, C. W. San Marchi, D. L. Medlin, *et al.* The influence of hydrogen on the low cycle fatigue behavior of strain-hardened 316L stainless steel. *Mater. Sci. Eng., A* (2022) 143477.

[26] ASTM International. E606-04: Standard Test Method for Strain-Controlled Fatigue Testing, *ASTM International*, West Conshohocken, PA, 2004.

[27] J. L. Walley, E. J. Lavernia, J. C. Gibeling. Low-Cycle Fatigue of Ultra-Fine-Grained Cryomilled 5083 Aluminum Alloy. *Metall. Mater. Trans. A* 40 (11) (2009) 2622-2630.

[28] M. A. Meyers, K. K. Chawla. Mechanical behavior of materials. *Cambridge university press*, 2008.

[29] S. Suresh. Fatigue of Materials. *Cambridge University Press*, Cambridge, 1998.

[30] K. J. Lu, A. Chauhan, F. Knopfle, *et al.* Effective and back stresses evolution upon cycling a high-entropy alloy. *Mater. Res. Lett.* 10 (6) (2022) 369-376.

[31] L. F. Coffin, Jr. A study of the effects of cyclic thermal stresses on a ductile metal. *Trans ASME* 76 (1954) 931-950.

[32] S. S. Manson. Behavior of Materials under Conditions of Thermal Stress. *National Advisory Committee for Aeronautics*, 1954, pp. 1-34.

[33] R. O. Ritchie. Mechanisms of fatigue-crack propagation in ductile and brittle solids. *Int. J. Fracture* 100 (1) (1999) 55-83.

# Chapter 5. The Kinetics of Dislocation Glide During Low Cycle Fatigue of the Equiatomic CrMnFeCoNi High Entropy Alloy[4]

## Abstract

Plastic strain rate change experiments are used to assess thermal activation parameters that describe the length scale of dislocation interactions on the glide plane during low cycle fatigue (LCF) tests in an annealed CrMnFeCoNi alloy. An initial evaluation of the hysteresis loops obtained from conventional LCF tests at plastic strain amplitudes from 0.3% to 0.6% reveals a yield point in the first cycle at all amplitudes. In addition, unusually low work hardening rates are observed during the initial cycles in this alloy. Operational activation areas are calculated using the theory of thermally activated dislocation glide at both the evolving and the dynamic equilibrium microstructural states. Changes in operational activation area during the initial cycles (250 $b^2$ to 170 $b^2$ across all plastic strain amplitudes) reflect the dynamic nature of the microstructure, and the magnitudes are consistent with dislocation glide controlled by forest dislocations and the solution-strengthened matrix. Additionally, Haasen plots are used to differentiate the contributions of these rate-controlling obstacles to the total operational activation area at the microstructural state of dynamic equilibrium. Dislocation interactions with the solid solution matrix are characterized by an activation area of 285 $b^2$. For forest dislocations, the activation area varies inversely with stress, reaching a finite value 365 $b^2$ at an offset flow stress of 150 MPa. Although cross slip contributes to microstructural development during cyclic deformation, it does not control the dislocation glide kinetics in the CrMnFeCoNi alloy, meaning

---

[4] To be submitted as D. M. Oliveira, E. P. George, and J. C. Gibeling. *Acta Mater.* (2023).

that the types of obstacles controlling cyclic deformation in this complex alloy are the same as those observed in conventional solution strengthened alloys under similar deformation conditions.

**Keywords:** Low Cycle Fatigue; Plastic Strain Rate Change; High Entropy Alloy; Activation Area; Thermally Activated Dislocation Glide.

## 5.1. Introduction

The CrMnFeCoNi alloy, also known as the Cantor alloy [1], is one of the most extensively studied compositions of face-centered cubic high entropy alloys (HEAs) both because it was one of the first such alloy compositions to be developed and due to its favorable mechanical behavior when compared to that of conventional alloys, such as austenitic stainless steels, especially at cryogenic temperatures [2-5]. Despite the number of studies describing its monotonic behavior as summarized recently by George, *et al.* [6] and Li, *et al.* [7], there are still relatively few reported studies of the performance of high entropy alloys, particularly the Cantor alloy, under cyclic loading. Since structural applications often require adequate fatigue resistance, there remains a need to further explore this important area.

Among the different approaches to analyzing fatigue behavior and determining fatigue lifetime, the strain-based approach provides a unique insight into the processes of damage accumulation that lead to crack nucleation in applications where stresses exceed the yield strength of the material at least locally [8, 9]. Interest in exploring the strain-controlled low cycle fatigue (LCF) behavior of the CrMnFeCoNi alloy and its derivatives has been increasing in the last few years [10-21]. Wang, *et al*. [10] characterized the LCF cracking behavior of this alloy with different grain sizes. They observed a transition from slip band cracking to twin band cracking when the difference in Schmid factors between the matrix and the twin increased, with the grain size influencing the critical difference required for this transition. Shams, *et al.* [12] compared the evolution of cyclic stresses and the lifetime of the CrMnFeCoNi alloy with that in conventional alloys. While they found that the CrMnFeCoNi alloy is more LCF resistant than 304 stainless steels, it failed in a fewer number of cycles than TWIP steels. The authors attributed these differences in fatigue performance to the deformation structures formed in each material after cyclic straining. Picak, *et* *al.* [11] focused on microstructural evolution in ultrafine grained CrMnFeCoNi alloy obtained by a severe plastic deformation method. The low and high angle grain boundaries formed after processing enhanced the cyclic strength compared to that of the coarse-grained counterpart, leading to improved LCF resistance at low strain amplitudes. Luo, et al. [13] investigated the effect of the grain size on the cyclic stress response and microstructural development at high total strain amplitude (± 1%). While deformation twins were observed in both coarse- and fine-grained CrMnFeCoNi alloy, dislocation substructures were reported to form in the latter condition and to induce a secondary hardening behavior near the end of the LCF lifetime. According to the authors, the twinning-dominated deformation mode was beneficial for the LCF lifetime in the coarse-grained condition in the high strain amplitude regime. Lu, *et al.* [14-17, 19] published an extensive set of studies exploring different aspects of the LCF behavior of the CrMnFeCoNi alloy, including its microstructural evolution at room temperature compared to that at 550°C [14, 15], the effect of the grain size on LCF behavior [16], development of Bauschinger stresses during cycling [19] and comparisons with the LCF behavior of the ternary CoCrNi HEA [17]. Oliveira, *et al.* [21] studied the effect of internal hydrogen on the cyclic stress response and LCF lifetime in the CrMnFeCoNi alloy. They found that hydrogen enhances the magnitude of effective stresses but does not influence the evolution of back stresses in this alloy. In addition, the presence of hydrogen severely degraded the LCF resistance of the CrMnFeCoNi alloy by inducing intergranular failure.

The studies described above highlight the performance of the CrMnFeCoNi alloy and its derivatives under cyclic straining and the microstructural features that characterize their cyclic deformation behavior. However, a detailed investigation of how dislocations move under cyclic loading conditions and the obstacles controlling the rate of cyclic deformation has not been published yet. To address this shortcoming, we adopt a well-founded framework to study cyclic plasticity using a kinetic law in the form of Eq. (5.1) to describe the dependence of the plastic strain rate ($\dot{\varepsilon}_p$) on the applied (true) stress (σ), the temperature (T) and the current microstructural state represented by the strength in the absence of thermal activation ($\hat{\sigma}$) [22]:

$$\dot{\varepsilon}_p = \dot{\varepsilon}_p(\sigma, T, \hat{\sigma}) \qquad \text{Eq. (5.1)}$$

Transient experiments such as stress relaxation and strain rate change tests are commonly used to probe the kinetics of dislocation motion in terms of the relationship between $\dot{\varepsilon}_p$ and σ at an instantaneous condition of constant microstructure, i.e., constant $\hat{\sigma}$ at a given temperature [23, 24]. In strain rate change experiments, for instance, an abrupt change in deformation rate (increase or decrease) is imposed during a short strain interval, and the resulting change in stress is measured. This change, which corresponds to the difference in stress necessary to maintain thermally activated dislocation glide at the new plastic strain rate, is then used to calculate the activation area. Physically, the activation area, Δa, characterizes dislocation motion through a field of discrete obstacles in the glide plane, and it is a function of the activation distance, Δy, and the equilibrium separation between obstacles for a uniform distribution, $l_e$, [22]:

$$\Delta a = \Delta y \times l_e \qquad \text{Eq. (5.2)}$$

The thermal activation parameter determined experimentally is the operational activation area, $\Delta a^*$. It is related (but not equal) to the true activation area and is given by the stress sensitivity of the strain rate through Eq. (5.3) [22]:

$$\Delta a^* = \frac{M k_B T}{b} \times \frac{\partial \ln \dot{\varepsilon}_p}{\partial \sigma} \qquad \text{Eq. (5.3)}$$

where M is the Taylor factor (3.06 for FCC materials), $k_B$ is the Boltzmann constant ($1.38x10^{-23}$ J/K), T is the temperature (298 K in this work), b is the magnitude of the Burgers vector (0.255 nm for CrMnFeCoNi alloy [25]) and $\dot{\varepsilon}_p$ is the true plastic strain rate.

The magnitude of the operational activation area $\Delta a^*$ can be used to identify the type of discrete, short-range thermal obstacles that control the kinetics of dislocation glide. For example, mobile dislocations overcoming solute atoms have characteristic $\Delta a^*$ values on the order of $10^1$-$10^2$ $b^2$, depending on the solute concentration [26-28]. For dislocations intersecting forest dislocations, $\Delta a^*$ ranges between $10^2$-$10^4$ $b^2$, depending on the dislocation density [26, 28, 29]. When cross slip controls the glide kinetics, $\Delta a^*$ values in the order of $10^1$-$10^2$ $b^2$ have been reported [26, 28, 30]. One challenge inherent in using these values is the difficulty of separating contributions from multiple mechanisms that simultaneously control the glide kinetics.

When the strain rate change tests are performed at a state of dynamic microstructural equilibrium, the inverse of the operational activation area varies linearly with the flow stresses. This linear behavior reflects the validity of the Cottrell-Stokes law [31], meaning that the relationship between the plastic strain rate and the flow stress is maintained constant during strain hardening. In this case, the plot of $1/\Delta a^*$ vs $\sigma$, also known as the Haasen plot, can be used to determine the nature of the obstacles controlling the rate of deformation [22, 32, 33]. If the data extrapolate through the origin, the only set of discrete obstacles to dislocation glide is forest dislocations. If the intercept is a positive value of $1/\Delta a^*$ or $\sigma$, there is at least a second set of obstacles to dislocation glide, which is more rate sensitive (thermal) or less rate sensitive (athermal) than forest dislocations, respectively. Furthermore, the slope of the Haasen plot is inversely proportional to the work of thermal activation associated with the obstacle whose density varies during strain hardening, and provides information regarding the characteristics of the obstacle profile [22, 32].

A few studies have been published reporting the thermal activation parameters and operative mechanisms of monotonic plastic deformation in the CrMnFeCoNi alloy at cryogenic [34-36], room [34-37] and high temperatures [38]. Overall, these studies suggest that the kinetics of dislocation motion in the CrMnFeCoNi alloy are controlled by processes that are similar to those observed in conventional solute strengthened FCC alloys, also implying that the current models of monotonic strengthening and plasticity can be extended to this compositionally complex class of materials. However, there are no such investigations under cyclic loading conditions, and the remaining question is whether the same conclusion can be drawn.

The goal of the current work is to use a framework of thermally activated dislocation glide to investigate how dislocations move in the CrMnFeCoNi high entropy alloy under cyclic loading conditions. In addition to the promising fatigue behavior, the stability of the FCC matrix in the CrMnFeCoNi alloy makes it a good representative material to understand plastic deformation in this new compositionally complex class of materials. Plastic strain rate change experiments were conducted during LCF tests at two different regions of the lifetime, probing operational activation area values that represent the evolving and dynamic equilibrium states of the microstructure. In addition to the rate change results, the work hardening behavior observed during the LCF tests is explored since it is also relevant to our understanding of the deformation mechanisms and the data analysis that enables the operational activation areas $\Delta a^*$ to be determined. The magnitudes of $\Delta a^*$ are compared to values reported in the literature in order to identify dislocation interactions that influence the cyclic deformation behavior in this HEA. In addition, the Haasen plot analysis is used to reveal the thermal obstacle(s) controlling the glide kinetics operating in the stable fatigue microstructure near saturation.

## 5.2. Materials and Methods

### *5.2.1. Material*

The CrMnFeCoNi alloy under investigation was prepared using procedures described in an earlier paper [21]. Briefly, the alloy was arc melted, drop cast and homogenized in vacuum at 1473 K for 24 h [4] and extruded in stainless steel cans at 1273 K at a total extrusion ratio of 9:1, resulting in an extrusion ratio of the HEA between 6:1 and 7:1. Cylindrical LCF specimens with gage dimensions of 3.2 mm in diameter and 10.2 mm in length, in compliance with ASTM E606 specifications [39], were machined from the extruded rods and their gage sections polished with SiC paper and diamond paste down to 0.25 μm. Lastly, the polished LCF specimens were vacuum annealed at 1173 K for 1h and furnace cooled, resulting in recrystallized and equiaxed grains with an average grain size of 31 ± 2 μm. In addition to a small number of Mn and Cr-rich particles, a relatively high density of annealing twins was found in the annealed microstructure [21].

### *5.2.2. Low Cycle Fatigue (LCF) and Plastic Strain Rate Change*

Fully reversed LCF tests were performed under true plastic strain control on an MTS 810 servo-hydraulic load frame running MTS TestStar and Testware-SX codes adapted from Kaschner and Gibeling [40]. Plastic strain amplitudes of 0.3%, 0.4% and 0.6% were probed at a base constant true plastic strain rate of $1 \mathrm{x} 10^{-3}\ \mathrm{s}^{-1}$, and two specimens were tested at each amplitude to improve the statistical significance of the results.

True plastic strain is a computed variable that is provided as a feedback signal in the closed loop control system, and it is calculated from measured true total strain and calculated elastic strains (using the measured load), as described in previous work [41]. Mughrabi and colleagues first developed plastic strain-controlled LCF tests, as summarized in reference [42]. By controlling (true) plastic strains, a constant plastic strain amplitude and plastic strain rate can be maintained throughout the test. Plastic strain is a deformation variable directly associated with damage accumulation processes that lead to fatigue failure, as described by the Coffin-Manson relationship [43, 44]. Plastic strain rate is also a fundamental variable that controls the stress response and microstructure development [22, 24]. Therefore, by controlling plastic strain, a systematic study of cyclic deformation can be conducted.

For the series of plastic strain rate changes during the LCF tests, an auxiliary computer running custom codes [40] to program an MTS 418.91 MicroProfiler was used as an external command source to impose rate changes within 50 ms. Two Hewlett-Packard 3458A digital voltmeters collected load and strain data at a sampling rate of 500 readings per second for a total of 4 seconds (2000 readings). The combination of a virtually instantaneous change in plastic strain rate and fast data acquisition means that each data set collected represents a constant microstructure experiment [24, 45, 46]. The external command source was programmed to run one complete cycle at the base plastic strain rate ($1x10^{-3}$ $s^{-1}$) prior to the cycle with the rate change. Both internal (TestStar) and external (MTS MicroProfiler) control channels were carefully tuned to provide an abrupt rate change with minimal load oscillations after the rate change, which was near the point of control instability.

The first type of the rate change experiment consisted of changing the base plastic strain rate of $1x10^{-3}$ $s^{-1}$ to a reduced rate of $5x10^{-4}$ $s^{-1}$, as shown schematically in Fig. 5.1 (a). This was repeated periodically at the peak tension plastic strain from the end of the third cycle to cumulative plastic strains of 15, which was defined here as a state of dynamic microstructural equilibrium based on the stress response curves shown in previous LCF work [21] and on studies of dislocation generation and annihilation processes during cyclic deformation by Essmann and Mughrabi [47]. The goal of this first set of rate changes was to use the evolution of the operational activation area with cumulative plastic strain to probe the microstructure that develops during cyclic deformation. We initially chose to impose an additional 0.15% plastic strain at the second plastic strain rate, consistent with our prior work on Type 316L stainless steel [48], but less than that used by Kaschner and Gibeling [49] in similar studies. However, the first tests at an amplitude of 0.3% plastic strain revealed that the mechanical response did not stabilize early in the test when an additional strain of 0.15% was imposed. Hence, this quantity was reduced to 0.10% for all subsequent tests. Hysteresis loops stabilized and $\Delta a^*$ values were consistent at large cumulative plastic strains using this value. After each rate change event, the specimen was cycled at the base plastic strain rate for at least two complete cycles to restore the base microstructure and minimize the effects of the prior change in deformation conditions [24].

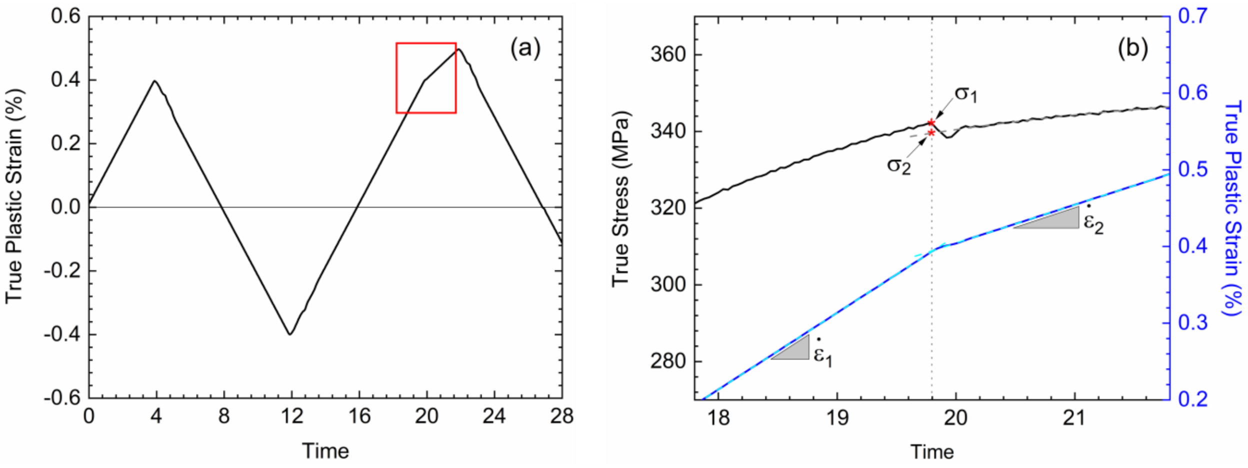

Fig. 5.1: Representative plots of (a) true plastic strain vs time, and (b) magnified true stress and true plastic strain responses at the instant of strain rate change. $\sigma_1$ and $\sigma_2$ are the true stresses immediately before and after the rate change, respectively. $\dot{\varepsilon}_1$ and $\dot{\varepsilon}_2$ are the corresponding true plastic strain rates. Here, the time scale was normalized by the time at which data acquisition was triggered, meaning the values on the x-axis are relative to that time.

After reaching the number of cycles corresponding to cumulative plastic strains of 15, the test was interrupted, and a similar protocol was then carried out. For this second set of experiments, rate changes were imposed at different values of plastic strain (and true stress) within the stable hysteresis loops during the portion of a cycle corresponding to unloading from compression (that is, reloading towards tension at stresses greater than zero). The additional plastic strain at the second rate was either that necessary to reach the peak plastic strain at a given strain amplitude or, if near the peak strain, 0.1% plastic strain as in the first set of experiments. The condition of dynamic microstructural equilibrium achieved at this stage of the lifetime allows for use of the Haasen plot analysis to assess the relationship between the operational activation area and the true stress as the obstacle spacing varies. Additional details regarding these two testing protocols are available in previous work [48].

For the calculation of the operational activation area, $\Delta a^*$, using Eq. (5.3), the true stress immediately before and after the rate change as well as the true plastic strain rates must be determined. In this work, the derivative of the true stress versus time data was used to identify the exact time of rate change and the true stress of interest at the base (nominal) strain rate. Then, the portion of the true stress versus time data at the second nominal strain rate was fitted with a weighted second order polynomial equation (up to an additional 0.1% plastic strain) and back extrapolated to determine the stress value at the reduced rate corresponding to the time of rate change. Finally, the slopes of the plastic strain-time data at each nominal plastic strain rate were taken as the true values of plastic strain rate. The variables of interest for the calculation of $\Delta a^*$ are illustrated in Fig. 5.1 (b). Additional details on the rate change protocol were published previously [40, 48].

## 5.3. Results and Discussion

### *5.3.1. Hardening Behavior During Low Cycle Fatigue*

Fig. 5.2 (a, c and e) shows typical hysteresis loops that characterize the cyclic stress response of the CrMnFeCoNi alloy at different stages of the lifetime (initial loading and first full cycle, at peak strength and at half-life) for each of the tested plastic strain amplitudes (0.3% to 0.6%). These results were obtained from companion (uninterrupted) LCF tests at a constant plastic strain rate of $1x10^{-3}$ $s^{-1}$ [21]; the hysteresis loops reveal important information regarding the strain hardening behavior of this alloy, especially during the early cycles, which directly influences the stress response and the back extrapolation of stress at the second strain rate after the rate change events. There is substantial hardening from the first cycle (black symbols) to the peak strength (red symbols), followed by softening until half-life (green symbols) was reached. Such evolution of the cyclic stresses is more fully illustrated in the stress response curve shown in an earlier study [21]. The hysteresis loops in Fig. 5.2 (a, c and e) also reveal a small yield point in this annealed CrMnFeCoNi alloy at all plastic strain amplitudes, which is evident in the first loading cycle and after the first reversal (the latter only in some tests). The yield point effect was not detected after the first cycle.

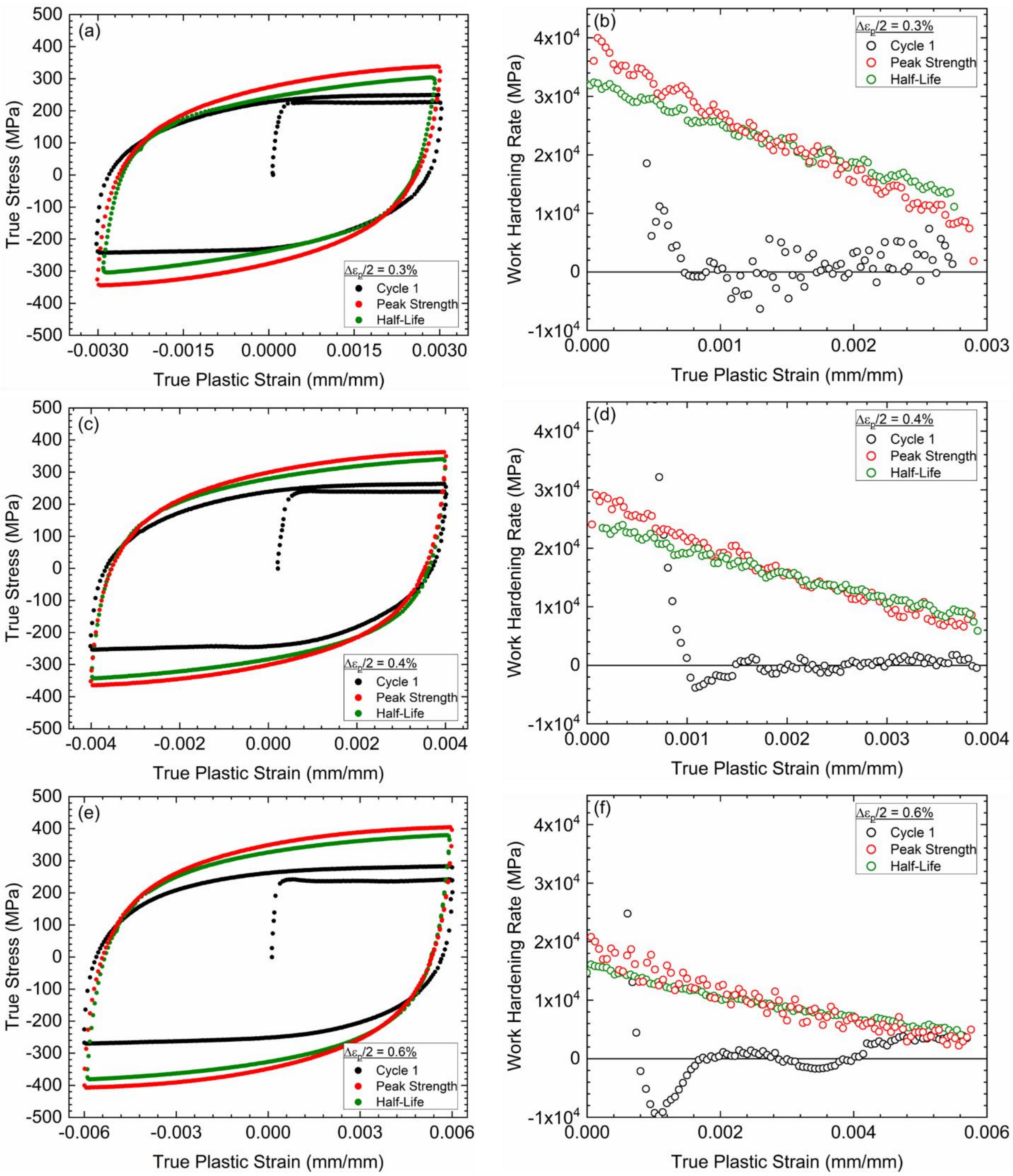

Fig. 5.2: Hysteresis loops obtained during LCF tests at a constant plastic strain rate and plastic strain amplitudes of (a) 0.3%, (c) 0.4% and (e) 0.6%. Black circles correspond to the loop for the first cycle. Red and green circles correspond to the loops at peak strength and half-life, respectively, at a given plastic strain amplitude. In addition, the work hardening rates in the tension segment (zero to peak plastic strain) in each one of these hysteresis loops are plotted as a function of the true plastic strain and are shown in (b, d and f).

Fig. 5.2 (b, d and f) shows the work hardening behavior during the tension segment of the hysteresis loops (Fig. 5.2 (a, c and e)) as a function of the true plastic strain. These work hardening rates were determined by taking the first derivative of the corresponding true stress vs. true plastic strain data. The yield point phenomenon is characterized by negative work hardening rates in the first cycle. Sun, *et al.* [50] observed a similar yield point in the CrMnFeCoNi alloy during tensile tests. They attributed this behavior to the high stress necessary to nucleate dislocations in the well-annealed initial microstructure compared to that necessary for dislocation glide, as seen in other materials. Otto, *et al.* [4] and Jang, *et al.* [51] also reported a similar phenomenon during monotonic deformation of the same HEA. Although the role of grain size and temperature is unclear, these authors mentioned the possibility of the yield point reflecting dislocations being pinned and breaking away from solute atoms or regions of short-range order. In the current work, we hypothesize that the compositional complexity of the high entropy alloys yields a rough energy landscape that may require higher stresses for dislocations to move during the first cycle when their initial density is very low [4, 52].

The CrMnFeCoNi alloy shows unusually low hardening rates during the initial cycles at all plastic strain amplitudes, which are manifested through relatively horizontal stress-strain segments (Fig. 5.2 (a, c and e)) and work hardening rates near zero (Fig. 5.2 (b, d and f)). This behavior extends to observations of the stress-strain response and work hardening rates during plastic strain rate change experiments, as illustrated in Fig. 5.3. Based on quantitative analysis of the initial microstructure reported by Otto, *et al.* [4] and Heckzo, *et al.* [52] after annealing at similar temperature and time conditions, the initial dislocation density is very low in this alloy (on the order of $10^{12}$ $m^{-2}$). Therefore, the low work hardening rates observed in Figs. 5.2 and 5.3 for the initial cycles arise from a weak initial microstructure, without enough dislocation interactions to increase the strength. As cyclic straining continues, the increase in work hardening rate reflects an increase in dislocation density and in interactions between dislocations.

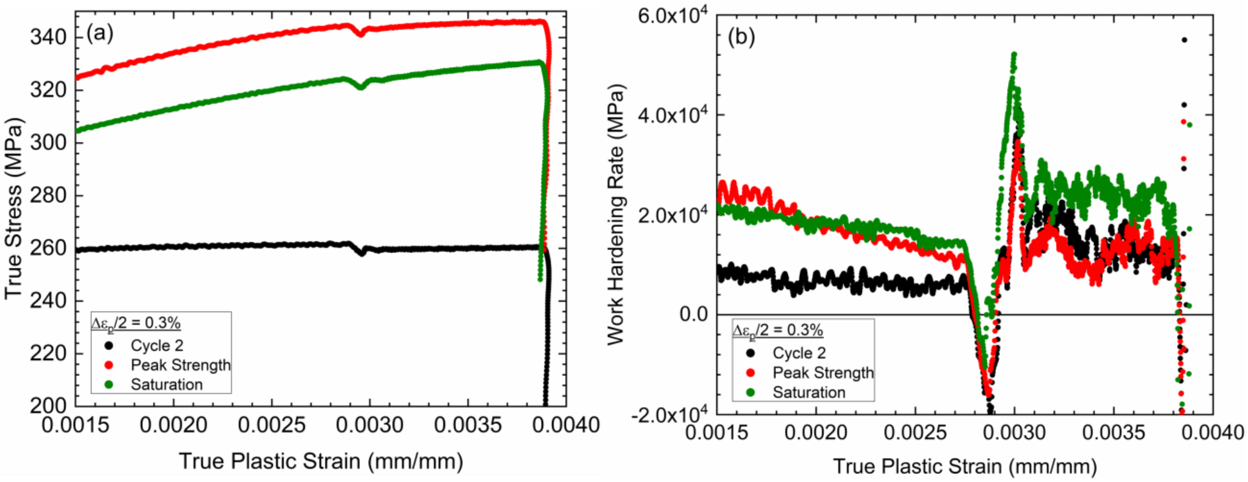

Fig. 5.3: (a) Hysteresis loops around the plastic strain rate change event and (b) corresponding work hardening rates at 0.3% plastic strain amplitude. Black circles represent the data for the second cycle (first rate change). Red and green circles correspond to the loops at peak strength and saturation state of the stress response, respectively.

The yield point and low initial work hardening rates in this alloy also complicated the testing protocol for the strain rate change tests. In previous work on FCC metals [40, 48, 49, 53], the first strain rate change was conducted at the end of the first quarter cycle. Attempting to follow that procedure for the CrMnFeCoNi alloy resulted in machine instability due to the unusual yielding and hardening response. For that reason, the tests were started in internal control (TestStar), then control was transferred to the external controller (MicroProfiler) at zero plastic strain on the compression side of the hysteresis loop during the second cycle and one complete cycle was run before initiating the strain rate change at the end of the third complete cycle. The constraints imposed by the material response mean that the activation areas could not be measured as early in the tests as was desired.

### *5.3.2. Activation Areas from Initial Cycles to Saturation*

Fig. 5.4 shows the inverse of the operational activation area normalized by the square of the Burgers vector ($b^2/\Delta a^*$) and plotted as a function of the cumulative plastic strain, defined here as four times the plastic strain amplitude times the number of cycles [9]. It also shows the evolution of the peak stresses for the same interval of cumulative plastic strain on the righthand y-axis. During the initial cycles, the rapid decrease in $\Delta a^*$ at a given plastic strain amplitude (by 50-60 $b^2$) correlates with the hardening and softening observed in the stress response curves with increasing cumulative plastic strain. As the microstructure achieves a state of dynamic equilibrium consisting of well-defined wall and cell formation [12, 16] characterized by a plateau in peak stresses, $\Delta a^*$ remains constant throughout the remainder of the tests.

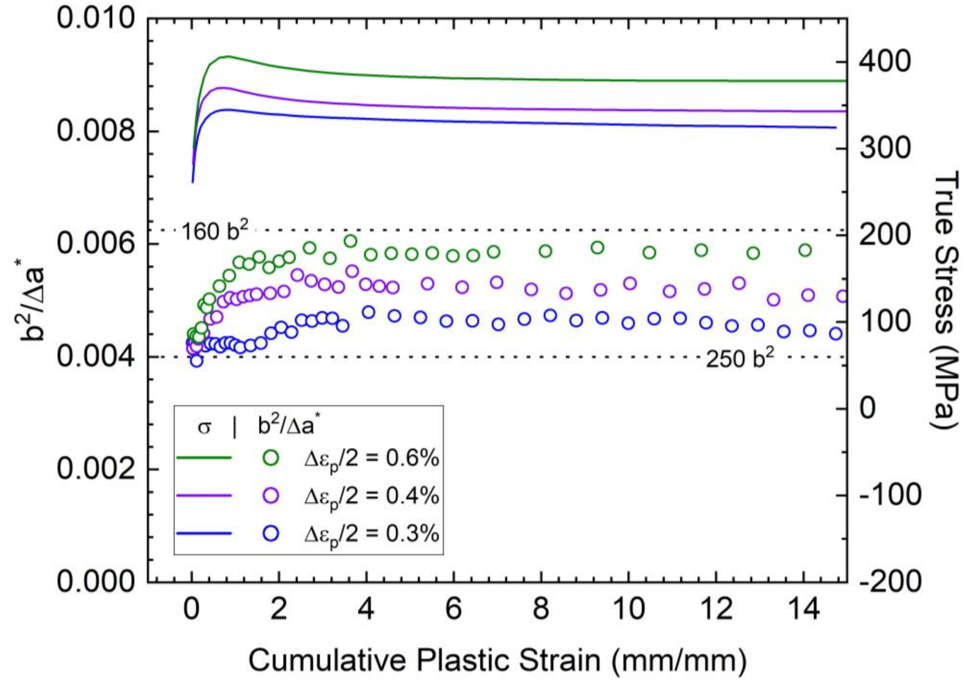

Fig. 5.4: Inverse of the operational activation area normalized by the square of the Burgers vector ($b^2/\Delta a^*$) (left y-axis) and true stress (right y-axis) as a function of cumulative plastic strain. Blue, violet and green symbols represent plastic strain amplitudes of 0.3%, 0.4% and 0.6%, respectively. The dashed lines indicate corresponding values of $\Delta a^*$ in units of $b^2$. Only one data set at each amplitude is shown for clarity.

Across all plastic strain amplitudes, $\Delta a^*$ ranges from 170 $b^2$ to 250 $b^2$. At saturation, there is a dependence of $\Delta a^*$ on plastic strain amplitude, from 170 $b^2$ at 0.3% to 220 $b^2$ at 0.6%. These values are within the range expected for alloys in which the discrete obstacles to the thermally activated glide of dislocations are solute atoms and forest dislocations [26-29]. Their individual contributions add to the total $\Delta a^*$ in reciprocal form as shown in Eq. (5.4) [22, 32]:

$$\frac{1}{\Delta a^*} = \frac{1}{\Delta a_S^*} + \frac{1}{\Delta a_F^*} \qquad \text{Eq. (5.4)}$$

where $\Delta a_S^*$ and $\Delta a_F^*$ represent the operational activation areas associated with dislocation interactions with the solid solution matrix and with forest dislocations, respectively. In addition, except for the very first cycles, $b^2/\Delta a^*$ scales with the plastic strain amplitude, indicating that $\Delta a^*$ is larger at low amplitude than at high amplitude at a given cumulative plastic strain. This result reflects the influence of the dislocation arrangements developed at different plastic strain amplitudes on the activation area. The forest dislocation spacing at low amplitudes is larger than at high amplitudes, as reflected in the stress.

The $\Delta a^*$ value obtained during the first rate change event at all plastic strain amplitudes (cycle number three) is 250 $b^2$. Although substantial hardening is observed during the initial cycles, the predominant contribution to this value is from $\Delta a_S^*$, and the remaining fraction of $\Delta a^*$ likely arises from $\Delta a_F^*$. As the plastic strain accumulates and the spacing between dislocations decreases, forest dislocations become more significant to the kinetics of dislocation glide, and changes in $\Delta a_F^*$ lead to a decrease in the total $\Delta a^*$. This interpretation assumes the solutes can be treated as discrete obstacles in this compositionally complex alloy. We base this assumption on the approach of Varvenne, *et al.* [54] in which they model the CrMnFeCoNi alloy as an average FCC matrix with discrete solutes that can be overcome by thermal activation. This approach has been shown to adequately describe the mechanical behavior of the Cantor alloy [36, 38, 54], but is certainly an approximation of this alloy in which the full details of the rough potential energy landscape that affect the rate of glide of a dislocation from one thermal obstacle to the next are simplified. For example, the model does not include a full consideration of local variations in the Burgers vector and the shear modulus, which may also affect dislocation motion, probably manifesting as a distributed, athermal glide resistance.

In addition to the interaction of gliding dislocations with solutes and forest dislocations, the importance of cross slip processes to the microstructural development that takes place during cyclic deformation in the CrMnFeCoNi alloy is highlighted by detailed reports of transmission electron microscopy (TEM) results. Lu, *et al.* [16] observed substructures resulting from wavy-slip at *total* strain amplitudes of 0.5% and 0.7%, corresponding to *plastic* strain amplitudes of approximately 0.3% and 0.5%, respectively. These dislocation substructures formed during the cyclic softening stage of lifetime (at relatively small cumulative plastic strains) and consisted of veins, walls, labyrinth and well-defined cells. Shams, *et al.* [12] also reported the formation of wall structures in this alloy during an early stage of lifetime at amplitudes corresponding to plastic strains above 0.5%, which further developed into well-defined dislocation cells with subsequent cyclic straining.

Despite the important role of cross slip in the development of a stable fatigue microstructure in the CrMnFeCoNi alloy, the magnitude of $\Delta a^*$ suggests that it does not control the rate of dislocation glide. If cross slip is included as a possible rate-controlling mechanism, then Eq. (5.4) becomes:

$$\frac{1}{\Delta a^*} = \frac{1}{\Delta a_S^*} + \frac{1}{\Delta a_F^*} + \frac{1}{\Delta a_{CS}^*} \qquad \text{Eq. (5.5)}$$

where $\Delta a^*_{CS}$ is the activation area for cross slip. At 0.6% plastic strain amplitude, for example, the value of $\Delta a^*$ at a cumulative plastic strain of 15 is about 170 $b^2$. Assuming that $\Delta a^*_S$ equals 250 $b^2$ (as an approximation from the data for the first rate change), the values of $\Delta a^*_F$ and $\Delta a^*_{CS}$ must each be larger than 530 $b^2$ for Eq. (5.5) to be satisfied. This is a reasonable magnitude for forest dislocations, but much larger than that reported by Bonneville and Escaig [30] for cross slip (300 $b^2$). Furthermore, if the $\Delta a^*$ contribution from cross slip is equal to the smallest possible value of 530 $b^2$, $\Delta a^*_F$ would approach an infinite value, meaning that forest dislocations would not be operative thermal obstacles. This is certainly not reasonable under these deformation conditions. We conclude that cross slip processes do not control the kinetics of dislocation glide in CrMnFeCoNi, although they are important in developing the cell structures that have been observed in this alloy at saturation.

### *5.3.3. Thermal Activation Parameters at Saturation*

At saturation, the activation area results can be represented using a Haasen plot of the inverse of the operational activation area normalized by the Burgers vector ($b^2/\Delta a^*$) as a function of stress. Traditionally, such a plot is based on the total applied stress [22, 32]. However, an alternative approach is to offset the applied stress by the yield strength ($\sigma_Y$) so that the stress-dependence of the activation areas in the Haasen plot characterizes only dislocation interactions associated with forest hardening [36]. In other words, the stresses on the Haasen plot are predominantly from forest dislocation strengthening, since contributions from solid solution strengthening ($\sigma_S$, which represents a thermally activated mechanism), the intrinsic lattice resistance ($\sigma_{LATT}$, an athermal contribution), and grain size strengthening ($\sigma_{GS}$, an athermal contribution) are accounted for in $\sigma_Y$, as expressed in Eq. (5.6):

$$\sigma_Y = \sigma_S + \sigma_{LATT} + \sigma_{GS} = \sigma_S + \sigma_{LATT} + kd^{-1/2} \qquad \text{Eq. (5.6)}$$

Here *k* is a material constant and *d* is the average grain size. In this work, $\sigma_Y$ is equal to 240 MPa, and it was obtained at 0.1% plastic strain offset using the first quarter cycle data at 0.6% plastic strain amplitude. This value of plastic strain offset was chosen to be consistent with the Bauschinger analysis performed in related work [21]. Furthermore, the lack of work hardening observed during the first LCF cycle (Fig. 5.2) implies that the $\sigma_Y$ would have the same value if taken at a 0.2% plastic strain offset. Finally, we note that Eq. (5.6) reduces to the familiar Hall-Petch relationship with $\sigma_0 = \sigma_S + \sigma_{LATT}$ consistent with the work of Laplanche, *et al*. [36].

Fig. 5.5 depicts the Haasen plot for the CrMnFeCoNi alloy, in which the offset flow stress is $\sigma$ - $\sigma_Y$. At a given offset flow stress, there is no clear dependence of $\Delta a^*$ on the plastic strain amplitude, and all the data were fitted with a single linear equation in the current work. This behavior was also observed by Kaschner and Gibeling [49] during plastic strain rate change experiments in cyclic deformation of 304 stainless steel, and it was attributed to the predominant influence of solutes on the kinetics of dislocation glide at the saturation state. Furthermore, the linearity of the data is confirmation that the Cottrell-Stokes law [31] holds, and that different data points in the Haasen plot probe the same stable microstructure but with different obstacle densities. The obstacles giving rise to this linear behavior are the forest dislocations.

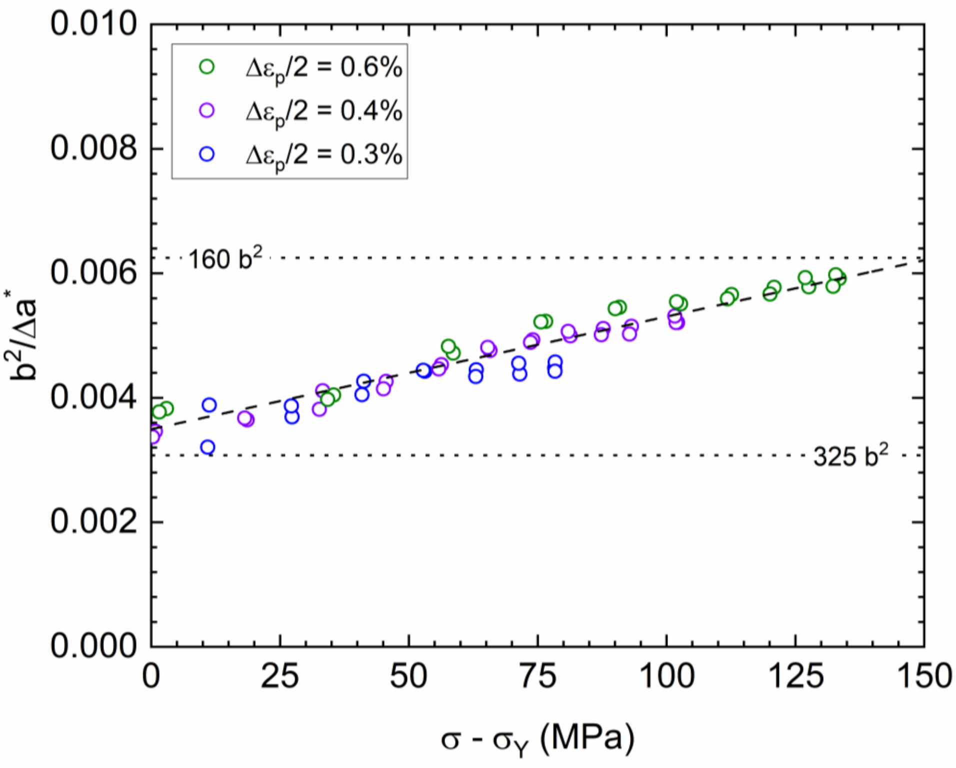

Fig. 5.5: Inverse of the operational activation area normalized by the square of the Burgers vector ($b^2/\Delta a^*$) as a function of the offset flow stress ($\sigma$-$\sigma_Y$), also known as the Haasen plot. Blue, violet and green symbols represent plastic strain amplitudes of 0.3%, 0.4% and 0.6%, respectively. All the data sets corresponding to different plastic strain amplitudes were fitted with a linear function. Only one data set at each amplitude is shown for clarity.

The Haasen plot data extrapolates to a positive value of $b^2/\Delta a^*$, indicating that there is at least one other set of thermal obstacles controlling the rate of cyclic deformation in the CrMnFeCoNi alloy besides forest dislocations [22, 32], which was identified in section 5.3.2 as solid solution strengthening. The magnitude of $\Delta a_S^*$ estimated from the intercept of the Haasen plot is 285 $b^2$, in good agreement with the 340 $b^2$ reported by Laplanche, *et al.* [36] in annealed CrMnFeCoNi alloy determined from stress relaxation experiments following monotonic deformation at room temperature.

The $\Delta a^*$ values in the Haasen plot (Fig. 5.5) vary from 285 $b^2$ at zero offset flow stress ($\sigma = \sigma_Y =$ 240 MPa) to 160 $b^2$ at an offset flow stress of 150 MPa ($\sigma =$ 390 MPa). The former value reflects the contribution of solution strengthening alone while the latter reflects the increasing contribution of forest dislocation strengthening as the stress increases and dislocation spacing decreases. Mulford [32] found similar orders of magnitude of $\Delta a^*$ after strain rate change experiments in monotonic deformation of aluminum alloys (~350 $b^2$ at 30 MPa and 240 $b^2$ at 120 MPa) and solution-hardened Inconel 600 (~130 $b^2$ at 150 MPa and 105 $b^2$ at 600 MPa). Kaschner and Gibeling [49] calculated ~140 $b^2$ at 200 MPa and 95 $b^2$ at 350 MPa in 304 stainless steel during cyclic deformation at saturation.

In addition, an analysis similar to that conducted in section 5.3.2 (Eq. (5.5)) can be performed to confirm that cross slip is not a rate-controlling obstacle influencing the kinetics of dislocation glide. At an offset stress of 150 MPa, if both $\Delta a_F^*$ and $\Delta a_{CS}^*$ contribute to the total $\Delta a^*$ of 160 $b^2$, their magnitudes must be larger than 365 $b^2$ (each). Taking $\Delta a_S^*$ as 285 $b^2$ from above and $\Delta a_{CS}^*$ as 400 $b^2$ (close to the 300 $b^2$ value estimated by Bonneville and Escaig [30]), $\Delta a_F^*$ would need to be greater than 4,000 $b^2$. Although this value is still reasonable for dislocation-dislocation interactions, it would imply that, at lower levels of stress, the magnitude of $\Delta a_{CS}^*$ and $\Delta a_F^*$ would need to be very large for both obstacles to be rate controlling. For example, at an offset flow stress of 100 MPa, $\Delta a^*$ is approximately 190 $b^2$, requiring $\Delta a_{CS}^*$ and $\Delta a_F^*$ to be greater than 570 $b^2$. If $\Delta a_{CS}^*$ is assumed to be an extreme value of 600 $b^2$, the value of $\Delta a_F^*$ suggests that forest dislocations are not operative ($\Delta a_F^*$ greater than 11,000 $b^2$). Therefore, the calculations of thermal activation parameters in the microstructural state of dynamic equilibrium also indicate that, despite occurring during cyclic deformation, cross slip processes do not control the kinetics of dislocation motion in the CrMnFeCoNi alloy. In the absence of cross slip as a thermally activated obstacle, $\Delta a_F^*$ can be estimated at a given offset flow stress value using Eq. (5.4). For an offset stress of 150 MPa, $\Delta a_F^*$ equals 365 $b^2$, within the range normally associated with forest dislocations [26, 28, 29, 38]. As the offset stress approaches zero, $\Delta a_F^*$ approaches an infinite value, reflecting the decreasing importance of forest dislocations as a rate-controlling obstacle at stress values near the yield stress.

Finally, we note that the value of $\Delta a_S^*$ obtained from the tests of cycling to saturation (250 $b^2$) differs from that obtained at saturation (285 $b^2$). We attributed this difference to the fact that in the tests to saturation, the first measurement of activation area was obtained at the end of the third cycle. As a consequence, it most likely includes a contribution from forest dislocations (which decreases the total $\Delta a^*$ as additional dislocations are generated) since this alloy hardens rapidly during the first several cycles. As such, we treat the estimate obtained from the strain rate change tests at a state of dynamic equilibrium of the microstructure (saturation) as the more reliable measure of $\Delta a_S^*$.

### 5.4. Conclusions

Plastic strain rate change experiments were conducted during plastic strain-controlled low cycle fatigue (LCF) tests in the annealed CrMnFeCoNi high entropy alloy, and operational activation areas $\Delta a^*$ were calculated at both the evolving and the dynamic equilibrium microstructural states. In addition, the work hardening behavior of this alloy during the LCF tests was reported, as it directly influences the stress response before and after the rate change event. The main findings are summarized below:

1. A small yield point is observed in the hysteresis loops for the first cycle in the CrMnFeCoNi alloy at all plastic strain amplitudes. This phenomenon is possibly due to the rough energy landscape that characterizes the compositional complexity in the high entropy alloys, especially in a well-annealed microstructure where the initial dislocation

density is very low. Furthermore, unusually low work hardening rates are observed within the hysteresis loops during the initial cycles.

2. The changes in $\Delta a^*$ from the initial cycles to a state of dynamic microstructural equilibrium (saturation) correlate with the evolution of peak cyclic stresses in this alloy. Across all plastic strain amplitudes, $\Delta a^*$ rapidly decreases from 250 $b^2$ (independent of amplitude) to a range of 170 $b^2$ to 220 $b^2$ (depending on amplitude) during the initial cycles, maintaining a constant value at large cumulative plastic strains. The magnitudes of $\Delta a^*$ are consistent with dislocation motion controlled by interactions with forest dislocations and the solid solution matrix.

3. The results of plastic strain rate change tests under conditions of dynamic microstructural equilibrium (saturation) demonstrate linearity on the Haasen plot and exhibit no dependence on plastic strain amplitude. These results confirm that the kinetics of dislocation glide are controlled by interactions with the solution-strengthened matrix and forest dislocations. The activation areas for these obstacles are 285 $b^2$ (independent of flow stress) and 365 $b^2$ (at an offset flow stress of 150 MPa), respectively. The activation area for forest dislocations varies inversely with the offset flow stress, reflecting its decreasing importance as a rate-controlling obstacle when the flow stress approaches the yield stress.

4. Although cross slip processes are important for microstructure development during cyclic straining in the CrMnFeCoNi alloy, the activation area analysis shows they do not represent rate-controlling obstacles to dislocation glide. This result further supports the idea that thermally activated dislocation glide during cyclic deformation in this compositionally complex alloy occurs by mechanisms that are the same as those observed

in this alloy under monotonic loading conditions and in conventional solution-strengthened alloys.

## Acknowledgments

Partial funding for this research was provided by the University of California, Davis and by donations to the Department of Materials Science and Engineering. Research at Oak Ridge National Laboratory (E.P.G.) was supported by the U.S. Department of Energy, Office of Science, Basic Energy Sciences, Materials Sciences and Engineering Division.

## References

[1] B. Cantor, I. T. H. Chang, P. Knight, *et al.* Microstructural development in equiatomic multicomponent alloys. *Mater. Sci. Eng., A* 375-377 (2004) 213-218.

[2] B. Gludovatz, A. Hohenwarter, D. Catoor, *et al.* A fracture-resistant high-entropy alloy for cryogenic applications. *Science* 345 (6201) (2014) 1153-1158.

[3] A. Gali, E. P. George. Tensile properties of high- and medium-entropy alloys. *Intermetallics* 39 (2013) 74-78.

[4] F. Otto, A. Dlouhy, C. Somsen, *et al.* The influences of temperature and microstructure on the tensile properties of a CoCrFeMnNi high-entropy alloy. *Acta Mater.* 61 (15) (2013) 5743-5755.

[5] G. Laplanche, A. Kostka, O. M. Horst, *et al.* Microstructure evolution and critical stress for twinning in the CrMnFeCoNi high-entropy alloy. *Acta Mater.* 118 (2016) 152-163.

[6] E. P. George, W. A. Curtin, C. C. Tasan. High entropy alloys: A focused review of mechanical properties and deformation mechanisms. *Acta Mater.* 188 (2020) 435-474.

[7] Z. Z. Li, S. T. Zhao, R. O. Ritchie, *et al.* Mechanical properties of high-entropy alloys with emphasis on face-centered cubic alloys. *Prog Mater Sci* 102 (2019) 296-345.

[8] N. E. Dowling. Mechanical Behavior of Materials: Engineering Methods for Deformation, Fracture and Fatigue. Third ed., *Pearson Prentive Hall,* Upper Saddle River, New Jersey, 2007.

[9] S. Suresh. Fatigue of Materials. *Cambridge University Press,* Cambridge, 1998.

[10] A. G. Wang, X. H. An, J. Gu, *et al.* Effect of grain size on fatigue cracking at twin boundaries in a CoCrFeMnNi high-entropy alloy. *J Mater Sci Technol* 39 (2020) 1-6.

[11] S. Picak, T. Wegener, S. V. Sajadifar, *et al.* On the low-cycle fatigue response of CoCrNiFeMn high entropy alloy with ultra-fine grain structure. *Acta Mater.* 205 (2021).

[12] S. A. A. Shams, G. Jang, J. W. Won, *et al.* Low-cycle fatigue properties of CoCrFeMnNi high-entropy alloy compared with its conventional counterparts. *Mater. Sci. Eng., A* 792 (2020).

[13] M. Y. Luo, T. N. Lam, P. T. Wang, *et al.* Grain-size-dependent microstructure effects on cyclic deformation mechanisms in CoCrFeMnNi high-entropy-alloys. *Scr. Mater.* 210 (2022).

[14] K. J. Lu, A. Chauhan, D. Litvinov, *et al.* Temperature-dependent cyclic deformation behavior of CoCrFeMnNi high-entropy alloy. *Int. J. Fatigue* 160 (2022).

[15] K. J. Lu, A. Chauhan, D. Litvinov, *et al.* High-temperature low cycle fatigue behavior of an equiatomic CoCrFeMnNi high-entropy alloy. *Mater. Sci. Eng., A* 791 (2020).

[16] K. J. Lu, A. Chauhan, A. S. Tirunilai, *et al.* Deformation mechanisms of CoCrFeMnNi high-entropy alloy under low-cycle-fatigue loading. *Acta Mater.* 215 (2021).

[17] K. J. Lu, A. Chauhan, M. Walter, *et al.* Superior low-cycle fatigue properties of CoCrNi compared to CoCrFeMnNi. *Scr. Mater.* 194 (2021).

[18] M. Jin, E. Hosseini, S. R. Holdsworth, *et al.* Thermally activated dependence of fatigue behaviour of CrMnFeCoNi high entropy alloy fabricated by laser powder-bed fusion. *Additive Manufacturing* 51 (2022).

[19] K. J. Lu, A. Chauhan, F. Knopfle, *et al.* Effective and back stresses evolution upon cycling a high-entropy alloy. *Mater. Res. Lett.* 10 (6) (2022) 369-376.

[20] M. Heczko, V. Mazanova, C. E. Slone, *et al.* Role of deformation twinning in fatigue of CrCoNi medium-entropy alloy at room temperature. *Scr. Mater.* 202 (2021).

[21] D. M. Oliveira, C. W. San Marchi, E. P. George, *et al.* Influence of Hydrogen on the Low Cycle Fatigue Behavior of the Equiatomic CrMnFeCoNi High Entropy Alloy. *Scr. Mater.* (2023). To be submitted.

[22] U. F. Kocks, A. S. Argon, M. F. Ashby. Thermodynamics and Kinetics of Slip. *Prog. Mater Sci.* 19 (1975) 1-281.

[23] J. L. Martin, B. Lo Piccolo, T. Kruml, *et al.* Characterization of thermally activated dislocation mechanisms using transient tests. *Mater. Sci. Eng., A* 322 (1-2) (2002) 118-125.

[24] H. Mughrabi. Cyclic Strain Rate Effects in Fatigued Face-Centred and Body-Centred Cubic Metals. *Philos Mag* 93 (28-30) (2013) 3821-3834.

[25] G. Laplanche, P. Gadaud, O. Horst, *et al.* Temperature dependencies of the elastic moduli and thermal expansion coefficient of an equiatomic, single-phase CoCrFeMnNi high-entropy alloy. *J Alloy Compd* 623 (2015) 348-353.

[26] H. Conrad. Thermally Activated Deformation of Metals. *Jom-J Met* 16 (7) (1964) 582-&.

[27] A. Argon. Strengthening mechanisms in crystal plasticity. *OUP Oxford*, 2007.

[28] A. Evans, R. Rawlings. The thermally activated deformation of crystalline materials. *physica status solidi (b)* 34 (1) (1969) 9-31.

[29] Z. S. Basinski. Thermally activated glide in face-centred cubic metals and its application to the theory of strain hardening. *The Philosophical Magazine: A Journal of Theoretical Experimental and Applied Physics* 4 (40) (1959) 393-432.

[30] J. Bonneville, B. Escaig. Cross-slipping process and the stress-orientation dependence in pure copper. *Acta Metall.* 27 (1979) 1477-1486.

[31] A. H. Cottrell, R. J. Stokes. Effects of Temperature on the Plastic Properties of Aluminium Crystals. *Proc R Soc Lon Ser-A* 233 (1192) (1955) 17-34.

[32] R. A. Mulford. Analysis of Strengthening Mechanisms in Alloys by Means of Thermal-Activation Theory. *Acta Metall.* 27 (1979) 1115-1124.

[33] P. Haasen. Plastic deformation of nickel single crystals at low temperatures. *Philosophical Magazine* 3 (28) (1958) 384-418.

[34] Z. Wu, Y. Gao, H. Bei. Thermal activation mechanisms and Labusch-type strengthening analysis for a family of high-entropy and equiatomic solid-solution alloys. *Acta Mater.* 120 (2016) 108-119.

[35] S. I. Hong, J. Moon, S. K. Hong, *et al.* Thermally activated deformation and the rate controlling mechanism in CoCrFeMnNi high entropy alloy. *Materials Science & Engineering A* 682 (2017) 569-576.

[36] G. Laplanche, J. Bonneville, C. Varvenne, *et al.* Thermal activation parameters of plastic flow reveal deformation mechanisms in the CrMnFeCoNi high-entropy alloy. *Acta Mater* 143 (2018) 257-264.

[37] Z. H. Han, W. N. Ren, J. Yang, *et al.* The deformation behavior and strain rate sensitivity of ultra-fine grained CoNiFeCrMn high-entropy alloys at temperatures ranging from 77 K to 573 K. *J Alloy Compd* 791 (2019) 962-970.

[38] M. Zhang, E. P. George, J. C. Gibeling. Elevated-temperature Deformation Mechanisms in a CrMnFeCoNi High-Entropy Alloy. *Acta Mater.* 218 (2021).

[39] ASTM International. E606-04: Standard Test Method for Strain-Controlled Fatigue Testing, *ASTM International*, West Conshohocken, PA, 2004.

[40] G. C. Kaschner, J. C. Gibeling. Strain Rate Change Transients During Cyclic Deformation of Copper. *Scr. Mater.* 35 (12) (1996) 1397-1402.

[41] D. M. Oliveira, C. W. San Marchi, D. L. Medlin, *et al.* The influence of hydrogen on the low cycle fatigue behavior of strain-hardened 316L stainless steel. *Mat Sci Eng A* (2022) 143477.

[42] H. Mughrabi. Microstructural fatigue mechanisms: Cyclic slip irreversibility, crack initiation, non-linear elastic damage analysis. *Int. J. Fatigue* 57 (2013) 2-8.

[43] L. F. Coffin, Jr. A study of the effects of cyclic thermal stresses on a ductile metal. *Trans ASME* 76 (1954) 931-950.

[44] S. S. Manson. Behavior of Materials under Conditions of Thermal Stress. *National Advisory Committee for Aeronautics*, 1954, pp. 1-34.

[45] U. F. Kocks, H. Mecking. Dislocation Kinetics at Not-So-Constant Structure. in: M. F. Ashby, R. Bullough, C. S. Hartley, *et al.* (Eds.), Dislocation Modeling of Physical Systems, *Pergamon*, Oxford, 1981, pp. 173-192.

[46] U. F. Kocks, S. R. Chen. On the Two Distinct Effects of Thermal Activation on Plasticity: Application to Nickel. *Physica Status Solidi A - Applied Research* 131 (1992) 403-413.

[47] U. Essmann, H. Mughrabi. Annihilation of Dislocations during Tensile and Cyclic Deformation and Limits of Dislocation Densities. *Philos. Mag.* A 40 (6) (1979) 731-756

[48] D. M. Oliveira, C. W. San Marchi, D. L. Medlin, *et al.* The Kinetics of Dislocation Glide During Low Cycle Fatigue of 316L Stainless Steel Containing Hydrogen. *Acta Mater.* (2023). To be submitted.

[49] G. C. Kaschner, J. C. Gibeling. A study of the mechanisms of cyclic deformation in f.c.c. metals using strain rate change tests. *Mater. Sci. Eng., A* 336 (1-2) (2002) 170-176.

[50] S. J. Sun, Y. Z. Tian, H. R. Lin, *et al.* Modulating the prestrain history to optimize strength and ductility in CoCrFeMnNi high-entropy alloy. *Scr. Mater.* 163 (2019) 111-115.

[51] M. J. Jang, S. Praveen, H. J. Sung, *et al.* High-temperature tensile deformation behavior of hot rolled CrMnFeCoNi high-entropy alloy. *J. Alloys Compd.* 730 (2018) 242-248.

[52] M. Heczko, V. Mazanova, R. Groger, *et al.* Elemental segregation to lattice defects in the CrMnFeCoNi high-entropy alloy during high temperature exposures. *Acta Mater.* 208 (2021).

[53] G. C. Kaschner, J. C. Gibeling. Evolution of dislocation glide kinetics during cyclic deformation of copper. *Acta Mater.* 50 (3) (2002) 653-662.

[54] C. Varvenne, A. Luque, W. A. Curtin. Theory of strengthening in fcc high entropy alloys. *Acta Mater.* 118 (C) (2016) 164-176.

[55] E. O. Hall. The Deformation and Ageing of Mild Steel .3. Discussion of Results. *P Phys Soc Lond B* 64 (381) (1951) 747-753.

[56] N. J. Petch. The Cleavage Strength of Polycrystals. *J Iron Steel I* 174 (1) (1953) 25-28.

# Chapter 6. Summary of Results and Future Research Opportunities

This dissertation study has investigated the low cycle fatigue (LCF) response and mechanisms of cyclic deformation in strain-hardened Type 316L stainless steel and annealed CrMnFeCoNi high entropy alloy (HEA) for structural and hydrogen energy-related applications. Plastic strain-controlled LCF tests were used to characterize the influence of internal hydrogen on the cyclic peak stress response and on the lifetimes associated with crack initiation and final failure processes. In addition, plastic strain rate change experiments during LCF provided detailed information about the dislocation interactions with discrete obstacles that control the kinetics of cyclic deformation. The main findings are summarized below:

1. Both the hydrogen-precharged and non-charged 316L stainless steel exhibit continuous softening during cyclic straining due to dislocation interactions in the strain-hardened microstructure. Internal hydrogen increases the cyclic strength of this alloy but significantly decreases the crack initiation and total lifetimes, especially at low plastic strain amplitudes. The effect of hydrogen on LCF performance is correlated with the reduced propensity for cross slip (more slip planarity), observed in scanning transmission electron microscopy (STEM) images of dislocation arrangements, and with the enhancement of effective stresses in the low strain amplitude regime.
2. The presence of hydrogen in Type 316L stainless steel leads to a decrease in operational activation area at a given true stress at all plastic strain amplitudes. Although hydrogen clearly influences the glide resistance, separating the contributions from dislocation interactions with solute atoms, forest dislocations and cross slip (when active) in this complex alloy is very challenging. Dislocation cells with tight walls and open interiors are observed in the non-charged condition at all plastic strain amplitudes. In contrast, dense

dislocation tangles dominate the microstructure in the hydrogen-precharged condition at low strain amplitudes, and well-defined cellular structures form only at high strain amplitude, implying that hydrogen influences the microstructure development in this alloy. The plastic strain amplitude dependence of the fatigue microstructure in the hydrogen-precharged condition is reflected in the magnitudes of athermal stresses. At low amplitudes, the athermal stresses are much larger in the hydrogen-precharged than in the non-charged condition, mainly attributed to dense dislocation tangles. As the microstructures become more similar in both material conditions at higher strain amplitudes, the magnitudes of athermal stresses converge.

3. Observations of serrated flow in hydrogen-precharged CrMnFeCoNi alloy during the first LCF cycle suggest that internal hydrogen pins mobile dislocations in the well-annealed initial microstructure. During cyclic straining, tension peak stresses rapidly increase to a peak strength, followed by softening to a plateau that characterizes stress saturation in the material with and without hydrogen. Despite increasing the cyclic stresses, hydrogen drastically decreases the number of cycles necessary to initiate a primary crack and cause final fatigue failure, and this effect on the lifetime is correlated with the enhancement of effective stresses. Furthermore, the addition of hydrogen in this alloy leads to a transition from ductile to brittle intergranular failure, consistent with the model of hydrogen-enhanced compatibility constraint across grain boundaries.
4. The well-annealed CrMnFeCoNi alloy exhibits a small yield point during the first LCF cycle, attributed to dislocation glide through the rough energy landscape in this complex alloy, which is intensified by a very low initial dislocation density. Detailed investigation of the kinetics of dislocation glide in this HEA during cyclic deformation reveals that the

operational activation area rapidly decreases as plastic strain accumulates in the initial cycles and then maintains a constant magnitude throughout the stress saturation region. The range of operational activation areas obtained both in the evolving and dynamic equilibrium microstructures indicates that the solution-strengthened matrix and forest dislocations are the discrete thermal obstacles controlling cyclic deformation in the CrMnFeCoNi alloy. Although dislocation cell structures have been shown to develop during LCF, cross slip does not contribute to the rate of thermally activated dislocation glide. The implication is that the compositional complexity of this alloy does not affect the mechanisms of dislocation motion when compared to conventional solid solution-strengthened alloys.

Overall, the findings of this dissertation research reveal important information about the LCF performance of Type of 316L stainless steel and CrMnFeCoNi high entropy alloy, which determine the applicability of these metallic materials in the structural and hydrogen energy sectors. They also provide fundamental information towards the understanding of cyclic plasticity, especially where the effect of hydrogen on deformation processes that lead to fatigue failure is not well understood. In addition, this research highlights the use of plastic strain rate change experiments during plastic strain-controlled LCF tests as a “mechanical microscopy” tool, providing quantitative information about rate-controlling obstacles that influence the macroscopic behavior and cannot be identified using conventional microscopy or mechanical testing techniques. Finally, the data generated in this study can be used as input in computational models of cyclic deformation behavior in FCC materials.

Some opportunities for future work that complement this dissertation research are listed below.

1. The magnitudes of the operational activation areas obtained in Type 316L stainless steel were used to identify the rate-controlling obstacles to dislocation glide in different material conditions. However, separating the contributions from each one of these thermal obstacles is very challenging, especially in a strain-hardened microstructure. Therefore, robust models of strengthening that account for processing history in complex alloys would provide a more quantitative analysis of thermal activation parameters and would further clarify the effect of hydrogen on dislocation interactions.
2. This research project used fatigue experiments in hydrogen-precharged specimens as a surrogate for tests in high pressure gaseous hydrogen environments, based on reports of good agreement between fatigue lifetimes obtained in *load-controlled* tests. However, our results suggest that *strain-control* represents a better tool to probe mechanistic information during fatigue tests. Despite the experimental challenges, it would be interesting to perform *strain-controlled* LCF tests in gaseous hydrogen environments and to evaluate whether the cyclic deformation behavior in stainless steel is similar with internal and external hydrogen.
3. The ternary CoCrNi HEA has been shown to possess superior monotonic and fatigue performance when compared to the CoCrFeMnNi alloy. However, its mechanical behavior in hydrogen environments has not been explored yet. Therefore, LCF tests in hydrogen-precharged CoCrNi would be helpful in determining its feasibility for hydrogen handling systems. In addition, the influence of hydrogen on the dislocation glide kinetics in both the CoCrNi and the CoCrFeMnNi alloys could be revealed by plastic strain rate change experiments.
4. Lastly, refractory BCC high entropy alloys are being extensively studied for potential applications in the aerospace industry. Since components in such applications are often

subjected to cyclic mechanical stresses (and cyclic thermal loadings), there is a need for a thorough characterization of the fatigue (and thermomechanical fatigue) behavior and mechanisms of cyclic deformation in these HEA compositions.

# Appendices

## A.1. Methodology to estimate LCF crack initiation lifetime from stress-strain hysteresis loops

The hysteresis loops obtained from a LCF test can be used to reveal the process of crack initiation (surface crack opening and closure processes) as the loop shape changes. Fig. A.1.1 shows the progression of the true stress and true plastic strain response in a PC specimen tested at a plastic strain amplitude of 0.1%, which clearly demonstrates cyclic softening. In addition, the apparent modulus for the cycles near end of life changes, which implies an additional effect of crack initiation and propagation.

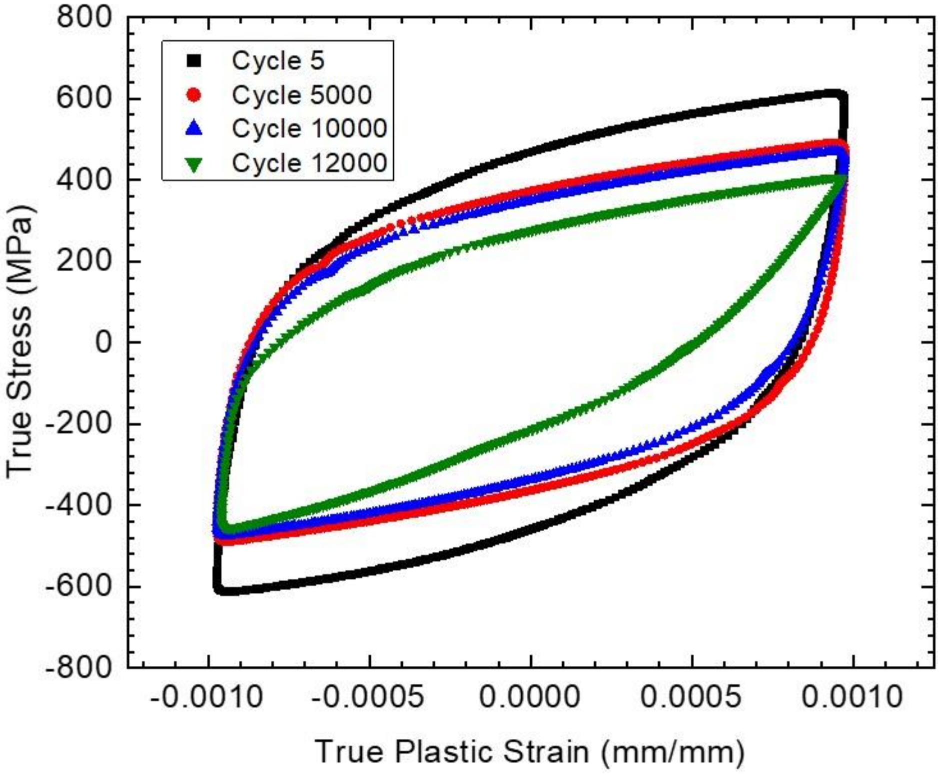

Fig. A.1.1: Hysteresis loops for PC 316L stainless steel tested at $\Delta\varepsilon_p/2 = 0.1\%$. The black (square), red (circle), blue (up-pointing triangle) and green (down-pointing triangle) loops represent the stress-strain response for cycles number 5, 5000, 10000 and 12000, respectively.

The analysis to estimate the crack initiation cycle is based on detecting a change in the apparent elastic response of the specimen and was conducted in MATLAB® following the steps that are summarized in Fig. A.1.2. A similar methodology was incorporated by Sheridan, *et al*. [1] to estimate fatigue crack initiation lifetime in additively manufactured alloy 718. These authors used applied load and axial displacement to calculate the compliance of each load cycle, and the number of cycles corresponding to a 0.3% change in compliance was defined as the initiation cycle. Even though the theoretical foundation for estimating fatigue crack initiation is analogous, the smoothing and fitting procedures as well as the testing variables used for the calculations and definition of initiation cycle differ in the current study.

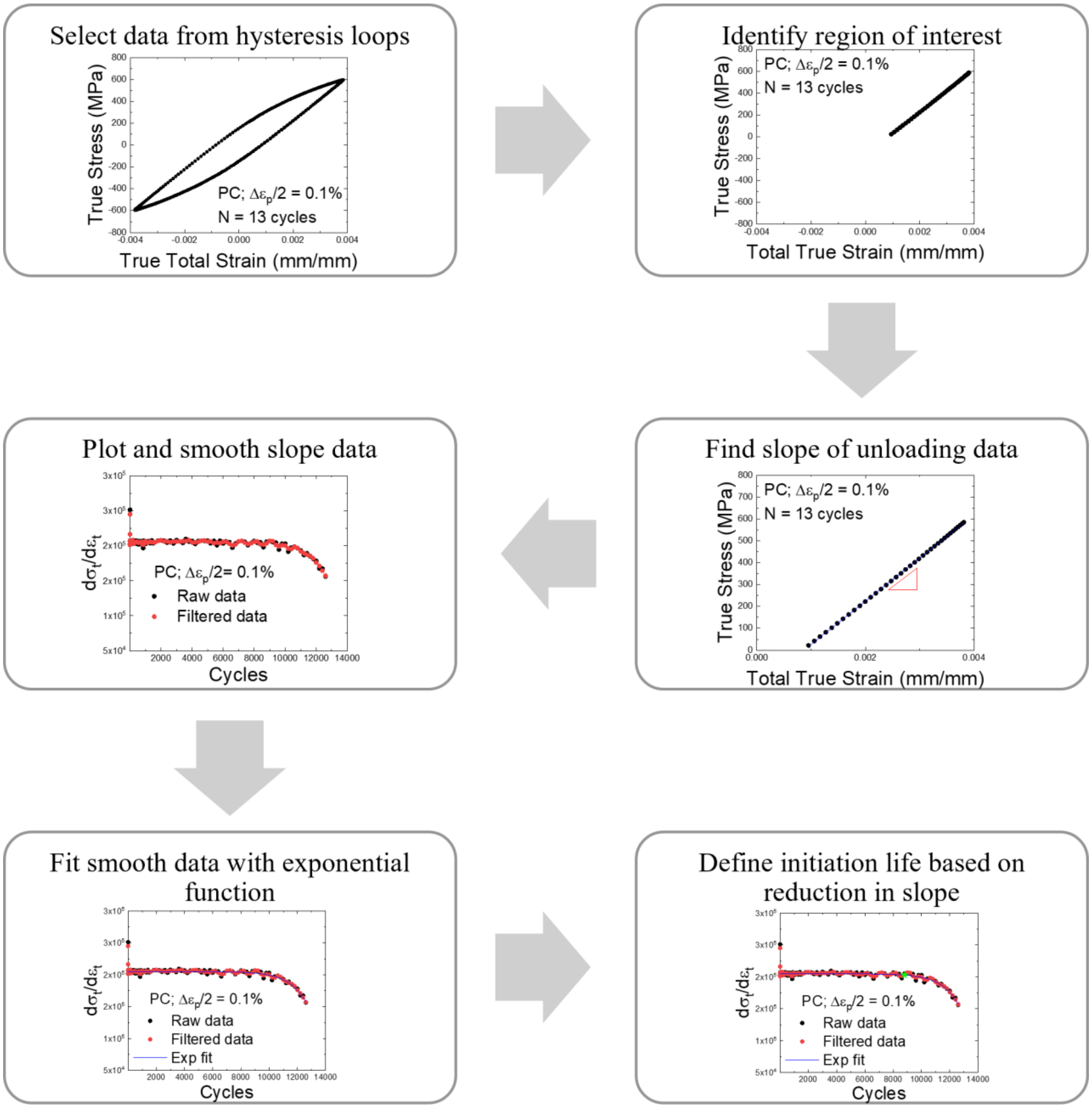

Fig. A.1.2: Schematic representation of the steps involved in the crack initiation analysis. All data processing was done using MATLAB®.

The first part of the analysis consists in identifying the points of interest in the hysteresis loops, shown in the second box of Fig. A.1.2, which are the tension unloading data, or the true values of stress and total strain from the tension peak to zero load. Once the range of interest is identified, the program uses a scoring system to identify the region within the selected strain-stress data providing the best combination of correlation and size of data set. The scoring system considers linear fits of all possible series of consecutive points; the initial point could be the tension peak or lower values of stress in the unloading stress-strain data array. Series with fewer than five points are excluded from consideration. The linear fits are then mapped on a two dimensional vector space where one axis is the correlation coefficient, $R^2$, and the other axis is the length (size) of the data set used to calculate the fit, divided by 100. The series of stress-strain values offering the largest vector in this constructed space is then selected as the range of interest for the calculation of the slope of the elastic unloading, using the method of least squares. After repeating this analysis for each hysteresis loop, the slope is plotted as a function of number of cycles $N$, and a Savitzky-Golay filter with a second order polynomial and variable number of points is employed to reduce the noise in the data. This method uses the least squares fitting of a second order polynomial with variable number of points (frame length). It has the advantage of smoothing without significant distortion of the original data trend [2, 3].

The smoothed slope data $d\sigma/d\varepsilon$, as shown in the fourth box of Fig. A.1.2, are then fitted to an exponential function represented by Eq. (A.1.1) in order to provide a better estimation of the initiation life.

$$\frac{d\sigma}{d\varepsilon} = c - \exp\left(\frac{N-a}{b}\right) \qquad \text{Eq. (A.1.1)}$$

where $a$, $b$ and $c$ are fitting constants controlling the start of the exponential decay on the x-axis (number of cycles $N$), the rate of decay and the y-axis (smoothed slope $d\sigma/d\varepsilon$) intercept, respectively. $N$ represents the number of cycles. The implemented method and algorithm are non-linear least squares and trust region, respectively. Table A.1.1 shows the range of allowable values for the parameters *a*, *b* and *c*, which vary with the data set.

Table A.1.1: Upper and lower bounds for the fitting parameters *a*, *b* and *c*, defined in Eq. (A.1.1).

| Parameter | Value |
|---|---|
| $a_{max}$ | total number of cycles |
| $a_{min}$ | -0.8 * total number of cycles |
| $b_{max}$ | 3000 |
| $b_{min}$ | 1 |
| $c_{max}$ | 1.5 * mean slope of 50% of the data |
| $c_{min}$ | 0.5* mean slope of 50% of the data |

The final step is the calculation of the number of cycles needed to yield a detectable decrease in slope, defined here as 1%, under the assumption that the slope remains approximately constant until a primary crack develops. The reference value for $d\sigma/d\varepsilon$ is the maximum value of the exponential fitting curve $(d\sigma/d\varepsilon)_{max}$, and then the fitting function is solved for $0.99^*(d\sigma/d\varepsilon)_{max}$. The initiation life obtained from this technique is plotted as a green star in the last box of Fig. A.1.2.

## A.2. Experimental details and data from LCF tests

Low cycle fatigue tests were performed in a closed-loop MTS servo-hydraulic testing system equipped with the following sensors: an MTS 661.20E-03 (S/N 104412, 100 kN capacity) and an Interface 1010AF-2.5k (S/N 69267A, 11 kN capacity) load cells and an MTS 632.26E-30 (S/N 441, ± 6% strain capacity) extensometer, which was attached to the specimen using 7.9 mm (5/16 in) rubber bands looped twice around the specimen. Regular/sharp knife edges were used on strain-hardened 316L stainless steel to prevent slippage of the extensometer. However, they left deep indents in the annealed CrMnFeCoNi specimens that acted as sites for the nucleation of a primary crack. For the subsequent tests, flat-faced radiused knife edges were glued to the gage section of the specimens. The alignment of the load frame was verified using a strain-gaged standard round specimen (Haynes 230 alloy, 12.7 mm gage diameter) connected to Vishay strain indicators. Adjustments on the MTS 609.10A-01 (Part # 90-083-501, S/N 1025805) alignment fixture corrected for concentric and angular misalignments. According to the ASTM standard for strain-controlled fatigue [4], the bending strains should not exceed 5% of the minimum axial strain range imposed during the tests. Since our fatigue tests use a 2% (total) strain range, concentric and angular strains were adjusted as often as needed to remain below 100 microstrain. More details on the LCF testing protocol are given in Chapters 2 and 4, and relevant testing variables are provided in Table A.2.1.

Table A.2.1: Variables for LCF setup in 316L and CrMnFeCoNi (HEA) alloys

| Material/ Condition | Elastic Modulus (MPa) | Tuning Parameters (Plastic Strain - SG) | | | | Flow Rate (gpm) | Valve Config. |
|---|---|---|---|---|---|---|---|
| | | P | I | D | F | | |
| 316L AR | 200,000 | 14,500-17,200 | 1,500 | 170 | 0 | 1 | Single |
| 316L PC | 206,000 | 13,700-17,200 | 1,500 | 170 | 0 | 1 | Single |
| 316L HT | 200,000 | 14,500-17,200 | 1,500 | 170 | 0 | 1 | Single |
| HEA | 229,000 | 2,600-2,800 | 40 | 35 | 1 | 10 | Single |
| H-HEA | 205,000 | 2,000-2,100 | 40 | 35 | 1.5 | 10 | Single |

The data obtained from the LCF tests were processed using a custom MATLAB® code and plotted using OriginPro®. The data contained in the cyclic stress-strain curves and in the strain-life plots are shown in Tables A.2.2-A.2.3 and A.2.4-A.2.5, respectively.

Table A.2.2: Tension peak stresses at half-life in strain-hardened 316L stainless steel

| **Strain-hardened 316L austenitic stainless steel** | | |
|---|---|---|
| | **Plastic Strain Amplitude (mm/mm)** | **True Peak Tension Stress (MPa)** |
| **AR** | 0.001 | 397.5 |
| | 0.001 | 387.7 |
| | 0.002 | 419.5 |
| | 0.002 | 423.9 |
| | 0.003 | 430.6 |
| | 0.004 | 453.6 |
| | 0.005 | 480.6 |
| | 0.007 | 520.5 |
| | 0.007 | 512.9 |
| | | |
| **PC** | 0.001 | 507.8 |
| | 0.001 | 487.5 |
| | 0.002 | 520.1 |
| | 0.002 | 527.5 |
| | 0.003 | 545.0 |
| | 0.004 | 553.1 |
| | 0.005 | 574.1 |
| | 0.007 | 587.3 |
| | 0.007 | 588.0 |
| | | |
| **HT** | 0.002 | 443.3 |
| | 0.004 | 482.2 |
| | 0.007 | 514.6 |

Table A.2.3: Tension peak stresses at half-life in annealed CrMnFeCoNi high entropy alloy

| **Annealed CrMnFeCoNi high entropy alloy** | | |
|---|---|---|
| | **Plastic Strain Amplitude (mm/mm)** | **True Peak Tension Stress (MPa)** |
| **HEA** | 0.003 | 308.9 |
| | 0.003 | 304.0 |
| | 0.004 | 340.6 |
| | 0.004 | 354.3 |
| | 0.006 | 384.7 |
| | 0.006 | 385.5 |
| | 0.006 | 380.0 |
| | 0.008 | 390.5 |
| | 0.008 | 388.9 |
| | | |
| **H-HEA** | 0.003 | 381.6 |
| | 0.003 | 387.0 |
| | 0.004 | 411.1 |
| | 0.004 | 406.9 |
| | 0.006 | 430.8 |
| | 0.006 | 434.9 |
| | 0.008 | 471.7 |
| | 0.008 | 476.4 |

Table A.2.4: Initiation and total LCF lifetimes in strain-hardened 316L stainless steel

| **Strain-hardened 316L austenitic stainless steel** | | | |
|---|---|---|---|
| | **Plastic Strain Amplitude (mm/mm)** | **Number of Cycles to Initiation (cycles)** | **Number of Cycles to Failure (cycles)** |
| **AR** | 0.001 | 25561 | 33834 |
| | 0.001 | 31605 | 32638 |
| | 0.002 | 8410 | 10175 |
| | 0.002 | 9348 | 9721 |
| | 0.003 | 3469 | 4227 |
| | 0.004 | 2649 | 2682 |
| | 0.005 | 1426 | 1967 |
| | 0.007 | - | 722 |
| | 0.007 | 602 | 827 |
| | | | |
| **PC** | 0.001 | 7436 | 7655 |
| | 0.001 | 8805 | 12739 |
| | 0.002 | 2931 | 3356 |
| | 0.002 | 2418 | 3442 |
| | 0.003 | 1297 | 1952 |
| | 0.004 | 1050 | 1257 |
| | 0.005 | 774 | 948 |
| | 0.007 | 360 | 484 |
| | 0.007 | 481 | 644 |
| | | | |
| **HT** | 0.002 | - | 9159 |
| | 0.004 | - | 2569 |
| | 0.007 | - | 1071 |

Table A.2.5: Initiation and total LCF lifetimes in annealed CrMnFeCoNi high entropy alloy

| Annealed CrMnFeCoNi high entropy alloy | | | |
|---|---|---|---|
| | **Plastic Strain Amplitude (mm/mm)** | **Number of Cycles to Initiation (cycles)** | **Number of Cycles to Failure (cycles)** |
| **HEA** | 0.003 | 20001 | 20885 |
| | 0.003 | 20601 | 21528 |
| | 0.004 | 10001 | 10536 |
| | 0.004 | 5401 | 6118 |
| | 0.006 | - | 3706 |
| | 0.006 | 4201 | 4249 |
| | 0.006 | 4744 | 5004 |
| | 0.008 | 2570 | 2957 |
| | 0.008 | 2201 | 2600 |
| | | | |
| **H-HEA** | 0.003 | 3001 | 3311 |
| | 0.003 | - | 2366 |
| | 0.004 | 901 | 1171 |
| | 0.004 | 1401 | 1698 |
| | 0.006 | 351 | 546 |
| | 0.006 | 301 | 485 |
| | 0.008 | 121 | 188 |
| | 0.008 | - | 105 |

### A.3. Experimental details and data from Plastic Strain Rate Change tests

Table A.3.1 contains relevant testing variables for the plastic strain rate change experiments. In addition, Table A.3.2 includes the plastic strain levels used for the rate change protocol. A detailed overview of the methodology is provided in Chapters 3 and 5.

Table A.3.1: Variables for Plastic Strain Rate Change setup

| **Material/ Condition** | **Elastic Modulus (MPa)** | **Tuning Parameters (Plastic Strain - SG)** | | | | **Tuning Parameters (Plastic Strain – 418.91)** | | | | **Flow Rate (gpm)** | **Valve Config.** |
|---|---|---|---|---|---|---|---|---|---|---|---|
| | | **P** | **I** | **D** | **F** | **P** | **I** | **D** | **F** | | |
| **316L AR** | 187,000 | 1900-2000 | 40 | 30 | 2 | 2000 | 40 | 40-45 | 2 | 10 | Single |
| **316L PC** | 193,000 | 1900-2000 | 40 | 30 | 2 | 2000 | 40 | 45 | 2 | 10 | Single |
| **HEA** | 229,000 | 2,000 | 40 | 30 | 2 | 2000 | 42.5 | 30 | 2 | 10 | Single |

Table A.3.2: Plastic strain levels for rate change protocol

| | **Plastic Strain Amplitude (mm/mm)** | **Transfer Level (mm/mm)** | **Jump Level (mm/mm)** | **End Level (mm/mm)** |
|---|---|---|---|---|
| **316L** | 0.003 | 0 | 0.003 | 0.0045 |
| | 0.004 | 0 | 0.004 | 0.0055 |
| | 0.006 | 0 | 0.006 | 0.0075 |
| | 0.008 | 0 | 0.008 | 0.0095 |
| **HEA** | 0.003 | 0 | 0.003 | 0.004 |
| | 0.004 | 0 | 0.004 | 0.005 |
| | 0.006 | 0 | 0.006 | 0.007 |

The data obtained from the Plastic Strain Rate Change tests were processed using a custom MATLAB® code and plotted using OriginPro®. The data contained in the Haasen plots are shown in Tables A.3.3 – A.3.14. The red font color is used to indicate data that were masked in the Haasen plots, following the criterion of lying outside the range between the 25th and 75th percentile by a factor of two times the interquartile range.

Table A.3.3: Haasen plot data for as-received (AR) strain-hardened 316L stainless steel at 0.3% plastic strain amplitude.

| **Specimen ID: AR4 A3** | | | | **Specimen ID: AR9 A3** | | | |
|---|---|---|---|---|---|---|---|
| **True Stress (MPa)** | **Stress Sensitivity of the Strain Rate $(\partial \ln \dot{\varepsilon}_p/\partial \ln \sigma)$** | $b^2/\Delta a^*$ | $\Delta a^*/b^2$ | **True Stress (MPa)** | **Stress Sensitivity of the Strain Rate $(\partial \ln \dot{\varepsilon}_p/\partial \ln \sigma)$** | $b^2/\Delta a^*$ | $\Delta a^*/b^2$ |
| 436.0 | 85 | 0.0067 | 150 | 442.1 | 95 | 0.0060 | 166 |
| 283.4 | 71 | 0.0051 | 195 | 314.1 | 87 | 0.0047 | 213 |
| 313.4 | 87 | 0.0047 | 213 | 339.9 | 89 | 0.0049 | 203 |
| 338.8 | 78 | 0.0057 | 177 | 362.9 | 81 | 0.0058 | 173 |
| 360.2 | 79 | 0.0059 | 169 | 382.4 | 83 | 0.0059 | 168 |
| 378.7 | 84 | 0.0059 | 171 | 400.0 | 79 | 0.0066 | 153 |
| 395.6 | 81 | 0.0063 | 158 | 415.6 | 78 | 0.0069 | 145 |
| 410.9 | 74 | 0.0072 | 139 | 429.6 | 79 | 0.0070 | 143 |
| 424.0 | 76 | 0.0072 | 139 | 442.4 | 81 | 0.0071 | 142 |
| 435.7 | 81 | 0.0070 | 143 | 442.0 | 85 | 0.0067 | 149 |
| 435.3 | 80 | 0.0070 | 142 | 281.9 | 95 | 0.0038 | 261 |
| 282.9 | 93 | 0.0040 | 253 | 313.4 | 88 | 0.0046 | 216 |
| 312.9 | 94 | 0.0043 | 232 | 339.5 | 90 | 0.0049 | 204 |
| 338.3 | 76 | 0.0057 | 174 | 362.2 | 82 | 0.0057 | 175 |
| 359.7 | 81 | 0.0058 | 174 | 382.0 | 79 | 0.0063 | 159 |
| 378.5 | 81 | 0.0061 | 165 | 399.2 | 80 | 0.0065 | 155 |
| 395.4 | 79 | 0.0065 | 154 | 414.9 | 76 | 0.0071 | 142 |
| 410.0 | 76 | 0.0070 | 143 | 428.9 | 83 | 0.0067 | 149 |
| 423.4 | 75 | 0.0073 | 136 | 441.5 | 84 | 0.0068 | 147 |
| 435.1 | 76 | 0.0075 | 134 | | | | |

Table A.3.4: Haasen plot data for as-received (AR) strain-hardened 316L stainless steel at 0.4% plastic strain amplitude. The red font color indicates data that were masked in the Haasen plots.

| **Specimen ID: AR2 A4** | | | | **Specimen ID: AR6 A4** | | | |
|---|---|---|---|---|---|---|---|
| **True Stress (MPa)** | **Stress Sensitivity of the Strain Rate $(\partial \ln \dot{\varepsilon}_p / \partial \ln \sigma)$** | **$b^2/\Delta a^*$** | **$\Delta a^*/ b^2$** | **True Stress (MPa)** | **Stress Sensitivity of the Strain Rate $(\partial \ln \dot{\varepsilon}_p / \partial \ln \sigma)$** | **$b^2/\Delta a^*$** | **$\Delta a^*/ b^2$** |
| 448.7 | 67 | 0.0087 | 115 | 449.8 | 73 | 0.0079 | 126 |
| 269.9 | 92 | 0.0038 | 261 | 274.0 | 94 | 0.0038 | 265 |
| 299.5 | 73 | 0.0053 | 189 | 302.8 | 87 | 0.0045 | 222 |
| 323.2 | 73 | 0.0057 | 174 | 326.2 | 77 | 0.0055 | 181 |
| 343.5 | 68 | 0.0065 | 154 | 346.4 | 66 | 0.0068 | 148 |
| 360.8 | 72 | 0.0065 | 153 | 363.5 | 72 | 0.0065 | 153 |
| 375.7 | 75 | 0.0065 | 153 | 377.8 | 86 | 0.0057 | 175 |
| 389.6 | 71 | 0.0072 | 140 | 391.6 | 77 | 0.0066 | 152 |
| 401.4 | 83 | 0.0063 | 159 | 403.5 | 81 | 0.0065 | 155 |
| 412.8 | 73 | 0.0073 | 137 | 414.7 | 79 | 0.0068 | 147 |
| 423.0 | 71 | 0.0077 | 130 | 424.5 | 76 | 0.0072 | 139 |
| 432.1 | 77 | 0.0073 | 137 | 433.5 | 76 | 0.0074 | 135 |
| 447.9 | 74 | 0.0079 | 127 | 449.0 | 70 | 0.0083 | 120 |
| 447.5 | 75 | 0.0077 | 129 | 448.8 | 70 | 0.0083 | 120 |
| 269.1 | 77 | 0.0045 | 221 | 272.5 | 103 | 0.0034 | 293 |
| 298.2 | 77 | 0.0050 | 200 | 301.4 | 95 | 0.0041 | 244 |
| 322.1 | 72 | 0.0058 | 173 | 325.2 | 75 | 0.0056 | 179 |
| 342.1 | 73 | 0.0061 | 164 | 344.8 | 75 | 0.0059 | 168 |
| 359.3 | 72 | 0.0065 | 155 | 361.8 | 75 | 0.0062 | 161 |
| 374.5 | 77 | 0.0063 | 159 | 376.7 | 83 | 0.0059 | 170 |
| 388.0 | 75 | 0.0067 | 148 | 390.4 | 76 | 0.0067 | 150 |
| 400.5 | 71 | 0.0073 | 137 | 402.4 | 77 | 0.0068 | 147 |
| 411.7 | 72 | 0.0074 | 135 | 413.1 | 78 | 0.0069 | 146 |
| 421.6 | 70 | 0.0078 | 129 | 423.2 | 73 | 0.0075 | 133 |
| 430.8 | 76 | 0.0074 | 136 | 431.8 | 81 | 0.0069 | 144 |
| 446.2 | 74 | 0.0078 | 128 | 447.5 | 73 | 0.0079 | 126 |

Table A.3.5: Haasen plot data for as-received (AR) strain-hardened 316L stainless steel at 0.6% plastic strain amplitude. The red font color indicates data that were masked in the Haasen plots.

| **Specimen ID: AR3 A6** | | | | **Specimen ID: AR5 A6** | | | |
|---|---|---|---|---|---|---|---|
| **True Stress (MPa)** | **Stress Sensitivity of the Strain Rate ($\partial \ln \dot{\varepsilon}_p/\partial \ln \sigma$)** | **$b^2/\Delta a^*$** | **$\Delta a^*/b^2$** | **True Stress (MPa)** | **Stress Sensitivity of the Strain Rate ($\partial \ln \dot{\varepsilon}_p/\partial \ln \sigma$)** | **$b^2/\Delta a^*$** | **$\Delta a^*/b^2$** |
| 328.9 | 71 | 0.0060 | 166 | 479.9 | 72 | 0.0086 | 116 |
| 365.4 | 65 | 0.0072 | 138 | 310.3 | 72 | 0.0056 | 179 |
| 392.9 | 65 | 0.0078 | 129 | 253.7 | 104 | 0.0032 | 317 |
| 414.8 | 68 | 0.0079 | 126 | 399.9 | 71 | 0.0073 | 137 |
| 433.0 | 68 | 0.0082 | 122 | 348.7 | 66 | 0.0068 | 146 |
| 448.2 | 70 | 0.0083 | 121 | 376.8 | 68 | 0.0072 | 140 |
| 461.2 | 66 | 0.0090 | 111 | 418.7 | 74 | 0.0074 | 136 |
| 472.2 | 71 | 0.0086 | 116 | 434.5 | 78 | 0.0072 | 139 |
| 326.4 | 73 | 0.0058 | 172 | 448.2 | 74 | 0.0079 | 127 |
| 362.7 | 69 | 0.0068 | 146 | 459.8 | 77 | 0.0077 | 129 |
| 390.2 | 67 | 0.0076 | 132 | 469.7 | 69 | 0.0089 | 113 |
| 412.1 | 65 | 0.0082 | 122 | 478.0 | 69 | 0.0090 | 111 |
| 430.2 | 67 | 0.0084 | 119 | 477.8 | 69 | 0.0090 | 111 |
| 445.4 | 70 | 0.0083 | 121 | 252.1 | 79 | 0.0041 | 243 |
| 458.3 | 66 | 0.0089 | 112 | 308.6 | 69 | 0.0058 | 171 |
| 469.3 | 72 | 0.0084 | 119 | 346.6 | 65 | 0.0069 | 145 |
| | | | | 374.8 | 67 | 0.0073 | 137 |
| | | | | 397.7 | 73 | 0.0071 | 141 |
| | | | | 416.7 | 72 | 0.0075 | 134 |
| | | | | 432.5 | 76 | 0.0074 | 135 |
| | | | | 446.1 | 77 | 0.0075 | 133 |
| | | | | 457.7 | 77 | 0.0077 | 129 |
| | | | | 467.6 | 69 | 0.0088 | 114 |
| | | | | 475.9 | 70 | 0.0088 | 113 |

Table A.3.6: Haasen plot data for as-received (AR) strain-hardened 316L stainless steel at 0.6% plastic strain amplitude. The red font color indicates data that were masked in the Haasen plots.

| **Specimen ID: AR10 A6** | | | | **Specimen ID: AR11 A6** | | | |
|---|---|---|---|---|---|---|---|
| **True Stress (MPa)** | **Stress Sensitivity of the Strain Rate $(\partial \ln \dot{\varepsilon}_p/\partial \ln \sigma)$** | **$b^2/\Delta a^*$** | **$\Delta a^*/b^2$** | **True Stress (MPa)** | **Stress Sensitivity of the Strain Rate $(\partial \ln \dot{\varepsilon}_p/\partial \ln \sigma)$** | **$b^2/\Delta a^*$** | **$\Delta a^*/b^2$** |
| 262.2 | 136 | 0.0025 | 400 | 492.9 | 80 | 0.0080 | 125 |
| 317.7 | 70 | 0.0059 | 169 | 238.8 | 154 | 0.0020 | 497 |
| 355.5 | 67 | 0.0069 | 145 | 301.3 | 76 | 0.0051 | 194 |
| 384.1 | 69 | 0.0072 | 139 | 343.4 | 71 | 0.0063 | 159 |
| 407.1 | 70 | 0.0075 | 133 | 375.0 | 74 | 0.0066 | 152 |
| 426.1 | 72 | 0.0077 | 130 | 400.7 | 75 | 0.0069 | 144 |
| 442.3 | 73 | 0.0078 | 128 | 421.9 | 76 | 0.0072 | 139 |
| 455.9 | 70 | 0.0084 | 119 | 439.9 | 78 | 0.0073 | 137 |
| 467.6 | 76 | 0.0079 | 126 | 455.3 | 80 | 0.0074 | 135 |
| 477.6 | 69 | 0.0090 | 111 | 468.7 | 80 | 0.0076 | 131 |
| | | | | 480.0 | 80 | 0.0080 | 128 |
| | | | | 489.9 | 79 | 0.0080 | 125 |
| | | | | 449.0 | 70 | 0.0080 | 120 |
| | | | | 448.8 | 70 | 0.0080 | 120 |
| | | | | 272.5 | 103 | 0.0030 | 293 |

Table A.3.7: Haasen plot data for as-received (AR) strain-hardened 316L stainless steel at 0.8% plastic strain amplitude. The red font color indicates data that were masked in the Haasen plots.

| **Specimen ID: AR7 A8** | | | | **Specimen ID: AR8 A8** | | | |
|---|---|---|---|---|---|---|---|
| **True Stress (MPa)** | **Stress Sensitivity of the Strain Rate $(\partial \ln \dot{\varepsilon}_p/\partial \ln \sigma)$** | **$b^2/\Delta a^*$** | **$\Delta a^*/b^2$** | **True Stress (MPa)** | **Stress Sensitivity of the Strain Rate $(\partial \ln \dot{\varepsilon}_p/\partial \ln \sigma)$** | **$b^2/\Delta a^*$** | **$\Delta a^*/b^2$** |
| 501.2 | 76 | 0.0086 | 117 | 518.3 | 72 | 0.0093 | 108 |
| 246.2 | 171 | 0.0019 | 536 | 269.9 | 120 | 0.0029 | 344 |
| 305.5 | 70 | 0.0056 | 177 | 326.7 | 72 | 0.0059 | 170 |
| 344.0 | 79 | 0.0057 | 177 | 364.7 | 68 | 0.0070 | 144 |
| 372.9 | 67 | 0.0072 | 139 | 392.4 | 70 | 0.0073 | 137 |
| 395.3 | 69 | 0.0074 | 135 | 414.2 | 71 | 0.0076 | 132 |
| 413.5 | 70 | 0.0076 | 131 | 432.1 | 72 | 0.0078 | 129 |
| 429.0 | 71 | 0.0078 | 129 | 447.2 | 74 | 0.0079 | 127 |
| 442.1 | 72 | 0.0079 | 126 | 460.1 | 74 | 0.0081 | 123 |
| 453.4 | 74 | 0.0080 | 125 | 471.3 | 73 | 0.0083 | 120 |
| 463.3 | 74 | 0.0082 | 122 | 480.7 | 82 | 0.0076 | 132 |
| 471.8 | 76 | 0.0081 | 124 | 489.4 | 76 | 0.0084 | 119 |
| 479.3 | 76 | 0.0082 | 122 | 496.7 | 72 | 0.0090 | 111 |
| 485.8 | 76 | 0.0083 | 120 | 503.0 | 77 | 0.0085 | 117 |
| 491.2 | 75 | 0.0085 | 118 | 508.4 | 70 | 0.0094 | 106 |
| 495.9 | 72 | 0.0089 | 113 | 512.8 | 71 | 0.0094 | 106 |

Table A.3.8: Haasen plot data for H-precharged (PC) strain-hardened 316L stainless steel at 0.3% plastic strain amplitude. The red font color indicates data that were masked in the Haasen plots.

| **Specimen ID: PC6 A3** | | | | **Specimen ID: PC11 A3** | | | |
|---|---|---|---|---|---|---|---|
| **True Stress (MPa)** | **Stress Sensitivity of the Strain Rate $(\partial \ln \dot{\varepsilon}_p/\partial \ln \sigma)$** | **$b^2/\Delta a^*$** | **$\Delta a^*/ b^2$** | **True Stress (MPa)** | **Stress Sensitivity of the Strain Rate $(\partial \ln \dot{\varepsilon}_p/\partial \ln \sigma)$** | **$b^2/\Delta a^*$** | **$\Delta a^*/ b^2$** |
| 529.3 | 59 | 0.0117 | 86 | 533.9 | 62 | 0.0112 | 89 |
| 352.0 | 67 | 0.0068 | 147 | 358.8 | 87 | 0.0053 | 188 |
| 388.8 | 72 | 0.0070 | 142 | 395.2 | 76 | 0.0067 | 148 |
| 418.7 | 61 | 0.0090 | 112 | 424.0 | 72 | 0.0076 | 131 |
| 443.0 | 60 | 0.0095 | 105 | 448.5 | 68 | 0.0085 | 117 |
| 464.3 | 60 | 0.0100 | 100 | 469.9 | 66 | 0.0093 | 108 |
| 483.7 | 60 | 0.0105 | 95 | 488.5 | 65 | 0.0097 | 103 |
| 500.2 | 58 | 0.0112 | 90 | 505.3 | 64 | 0.0102 | 98 |
| 514.7 | 62 | 0.0107 | 93 | 520.2 | 66 | 0.0102 | 98 |
| 527.6 | 61 | 0.0112 | 89 | 533.0 | 62 | 0.0111 | 90 |
| 527.8 | 59 | 0.0116 | 86 | 532.8 | 61 | 0.0112 | 89 |
| 350.0 | 81 | 0.0056 | 178 | 310.0 | 129 | 0.0031 | 321 |
| 387.6 | 76 | 0.0067 | 150 | 357.6 | 87 | 0.0054 | 187 |
| 416.4 | 67 | 0.0081 | 124 | 393.6 | 75 | 0.0068 | 146 |
| 440.9 | 68 | 0.0084 | 120 | 422.9 | 63 | 0.0086 | 116 |
| 462.7 | 62 | 0.0097 | 104 | 447.5 | 64 | 0.0091 | 110 |
| 481.1 | 67 | 0.0093 | 108 | 469.1 | 62 | 0.0098 | 102 |
| 498.2 | 63 | 0.0102 | 98 | 486.8 | 66 | 0.0096 | 104 |
| 513.1 | 61 | 0.0108 | 92 | 504.0 | 59 | 0.0110 | 91 |
| | | | | 518.5 | 63 | 0.0106 | 94 |
| | | | | 531.2 | 60 | 0.0114 | 88 |

Table A.3.9: Haasen plot data for H-precharged (PC) strain-hardened 316L stainless steel at 0.4% plastic strain amplitude. The red font color indicates data that were masked in the Haasen plots.

| **Specimen ID: PC3 A4** | | | | **Specimen ID: PC7 A4** | | | |
|---|---|---|---|---|---|---|---|
| **True Stress (MPa)** | **Stress Sensitivity of the Strain Rate ($\partial \ln\dot{\varepsilon}_p/\partial \ln\sigma$)** | **$b^2/\Delta a^*$** | **$\Delta a^*/b^2$** | **True Stress (MPa)** | **Stress Sensitivity of the Strain Rate ($\partial \ln\dot{\varepsilon}_p/\partial \ln\sigma$)** | **$b^2/\Delta a^*$** | **$\Delta a^*/b^2$** |
| 540.7 | 57 | 0.0123 | 82 | 544.6 | 53 | 0.0133 | 75 |
| 326.7 | 100 | 0.0042 | 237 | 329.7 | 72 | 0.0060 | 168 |
| 363.4 | 65 | 0.0072 | 138 | 365.6 | 64 | 0.0074 | 136 |
| 392.4 | 61 | 0.0083 | 121 | 394.8 | 65 | 0.0079 | 127 |
| 416.7 | 57 | 0.0094 | 106 | 418.9 | 58 | 0.0094 | 107 |
| 437.2 | 55 | 0.0103 | 97 | 440.0 | 53 | 0.0107 | 93 |
| 455.0 | 57 | 0.0103 | 97 | 457.5 | 61 | 0.0097 | 103 |
| 471.2 | 58 | 0.0106 | 95 | 474.1 | 58 | 0.0106 | 94 |
| 485.5 | 59 | 0.0106 | 94 | 488.7 | 56 | 0.0113 | 89 |
| 498.3 | 54 | 0.0119 | 84 | 501.6 | 52 | 0.0125 | 80 |
| 510.1 | 56 | 0.0119 | 84 | 513.4 | 52 | 0.0129 | 78 |
| 520.7 | 53 | 0.0128 | 78 | 524.3 | 51 | 0.0133 | 75 |
| 538.7 | 55 | 0.0126 | 80 | 542.2 | 54 | 0.0129 | 78 |
| 538.2 | 54 | 0.0130 | 77 | 541.5 | 57 | 0.0123 | 81 |
| 324.6 | 82 | 0.0051 | 195 | 327.4 | 73 | 0.0058 | 171 |
| 360.6 | 71 | 0.0066 | 151 | 363.3 | 69 | 0.0068 | 147 |
| 389.8 | 60 | 0.0084 | 119 | 392.2 | 68 | 0.0075 | 134 |
| 414.4 | 55 | 0.0097 | 103 | 416.9 | 54 | 0.0100 | 100 |
| 434.2 | 64 | 0.0088 | 114 | 437.1 | 56 | 0.0102 | 98 |
| 451.9 | 64 | 0.0092 | 109 | 455.2 | 56 | 0.0105 | 95 |
| 468.4 | 57 | 0.0106 | 95 | 471.3 | 58 | 0.0106 | 94 |
| 482.7 | 58 | 0.0107 | 93 | 485.8 | 57 | 0.0110 | 91 |
| 495.8 | 54 | 0.0120 | 84 | 498.7 | 53 | 0.0121 | 83 |
| 507.5 | 51 | 0.0128 | 78 | 510.6 | 51 | 0.0128 | 78 |
| 517.8 | 51 | 0.0131 | 76 | 521.0 | 51 | 0.0132 | 76 |
| 535.8 | 54 | 0.0129 | 77 | 539.2 | 54 | 0.0130 | 77 |

Table A.3.10: Haasen plot data for H-precharged (PC) strain-hardened 316L stainless steel at 0.6% plastic strain amplitude. The red font color indicates data that were masked in the Haasen plots.

| **Specimen ID: PC2 A6** | | | | **Specimen ID: PC5 A6** | | | |
|---|---|---|---|---|---|---|---|
| **True Stress (MPa)** | **Stress Sensitivity of the Strain Rate $(\partial \ln \dot{\varepsilon}_p/\partial \ln \sigma)$** | **$b^2/\Delta a^*$** | **$\Delta a^*/ b^2$** | **True Stress (MPa)** | **Stress Sensitivity of the Strain Rate $(\partial \ln \dot{\varepsilon}_p/\partial \ln \sigma)$** | **$b^2/\Delta a^*$** | **$\Delta a^*/ b^2$** |
| 557.3 | 51 | 0.0141 | 71 | 564.1 | 51 | 0.0143 | 70 |
| 307.7 | 78 | 0.0051 | 197 | 295.4 | 66 | 0.0058 | 174 |
| 371.0 | 52 | 0.0093 | 108 | 363.0 | 53 | 0.0089 | 113 |
| 412.9 | 50 | 0.0107 | 93 | 407.5 | 51 | 0.0103 | 97 |
| 444.1 | 50 | 0.0114 | 88 | 440.9 | 52 | 0.0110 | 91 |
| 468.9 | 52 | 0.0117 | 85 | 467.2 | 55 | 0.0110 | 91 |
| 489.4 | 54 | 0.0118 | 85 | 489.7 | 54 | 0.0118 | 84 |
| 506.7 | 50 | 0.0130 | 77 | 508.4 | 53 | 0.0123 | 81 |
| 521.6 | 51 | 0.0133 | 75 | 524.5 | 50 | 0.0136 | 73 |
| 534.2 | 51 | 0.0137 | 73 | 538.0 | 51 | 0.0137 | 73 |
| 544.6 | 51 | 0.0138 | 73 | 549.7 | 50 | 0.0142 | 71 |
| 553.1 | 51 | 0.0141 | 71 | 558.9 | 50 | 0.0146 | 69 |
| 552.6 | 50 | 0.0142 | 71 | 558.2 | 51 | 0.0141 | 71 |
| 304.3 | 73 | 0.0054 | 185 | 291.8 | 62 | 0.0061 | 163 |
| 366.9 | 57 | 0.0083 | 120 | 358.7 | 48 | 0.0096 | 104 |
| 408.9 | 50 | 0.0105 | 95 | 402.4 | 54 | 0.0096 | 104 |
| 440.0 | 50 | 0.0113 | 88 | 435.7 | 55 | 0.0102 | 98 |
| 464.8 | 51 | 0.0117 | 86 | 462.4 | 53 | 0.0112 | 89 |
| 485.1 | 54 | 0.0117 | 85 | 484.2 | 56 | 0.0112 | 89 |
| 502.5 | 50 | 0.0130 | 77 | 503.0 | 56 | 0.0117 | 85 |
| 517.2 | 51 | 0.0131 | 76 | 518.9 | 55 | 0.0123 | 81 |
| 529.7 | 51 | 0.0134 | 74 | 532.4 | 52 | 0.0133 | 75 |
| 540.4 | 49 | 0.0144 | 69 | 543.9 | 51 | 0.0139 | 72 |
| 548.8 | 51 | 0.0140 | 72 | 553.2 | 51 | 0.0139 | 72 |

Table A.3.11: Haasen plot data for H-precharged (PC) strain-hardened 316L stainless steel at 0.8% plastic strain amplitude. The red font color indicates data that were masked in the Haasen plots.

| **Specimen ID: PC8 A8** | | | | **Specimen ID: PC9 A8** | | | |
|---|---|---|---|---|---|---|---|
| **True Stress (MPa)** | **Stress Sensitivity of the Strain Rate ($\partial \ln \dot{\varepsilon}_p / \partial \ln \sigma$)** | **$b^2/\Delta a^*$** | **$\Delta a^*/ b^2$** | **True Stress (MPa)** | **Stress Sensitivity of the Strain Rate ($\partial \ln \dot{\varepsilon}_p / \partial \ln \sigma$)** | **$b^2/\Delta a^*$** | **$\Delta a^*/ b^2$** |
| 578.9 | 50 | 0.0150 | 67 | 590.8 | 50 | 0.0154 | 65 |
| 266.5 | 63 | 0.0055 | 182 | 294.8 | 79 | 0.0048 | 207 |
| 338.8 | 46 | 0.0095 | 105 | 361.4 | 54 | 0.0087 | 115 |
| 385.5 | 45 | 0.0111 | 90 | 405.6 | 46 | 0.0114 | 88 |
| 418.3 | 52 | 0.0104 | 96 | 437.5 | 48 | 0.0118 | 85 |
| 445.2 | 51 | 0.0112 | 89 | 462.9 | 48 | 0.0125 | 80 |
| 467.4 | 50 | 0.0121 | 83 | 483.6 | 50 | 0.0125 | 80 |
| 485.5 | 55 | 0.0115 | 87 | 501.2 | 50 | 0.0128 | 78 |
| 501.8 | 53 | 0.0123 | 81 | 515.8 | 51 | 0.0132 | 76 |
| 515.7 | 52 | 0.0128 | 78 | 529.0 | 49 | 0.0140 | 72 |
| 528.1 | 52 | 0.0131 | 76 | 540.5 | 49 | 0.0142 | 70 |
| 538.5 | 55 | 0.0128 | 78 | 550.3 | 51 | 0.0141 | 71 |
| 547.9 | 54 | 0.0131 | 76 | 558.8 | 50 | 0.0144 | 69 |
| 556.0 | 51 | 0.0140 | 71 | 566.1 | 51 | 0.0144 | 70 |
| 562.8 | 50 | 0.0146 | 69 | 571.9 | 51 | 0.0144 | 69 |
| 568.4 | 48 | 0.0153 | 66 | 576.5 | 50 | 0.0148 | 68 |

Table A.3.12: Haasen plot data for annealed CrMnFeCoNi high entropy alloy at 0.3% plastic strain amplitude. The red font color indicates data that were masked in the Haasen plots.

| **Specimen ID: HEA20 A3** | | | | **Specimen ID: HEA25 A3** | | | |
|---|---|---|---|---|---|---|---|
| **True Stress (MPa)** | **Stress Sensitivity of the Strain Rate $(\partial \ln \dot{\varepsilon}_p / \partial \ln \sigma)$** | **$b^2/\Delta a^*$** | **$\Delta a^*/ b^2$** | **True Stress (MPa)** | **Stress Sensitivity of the Strain Rate $(\partial \ln \dot{\varepsilon}_p / \partial \ln \sigma)$** | **$b^2/\Delta a^*$** | **$\Delta a^*/ b^2$** |
| 318.3 | 93 | 0.0045 | 223 | 333.9 | 84 | 0.0052 | 193 |
| 207.0 | 154 | 0.0018 | 566 | 248.4 | 81 | 0.0040 | 249 |
| 232.0 | 95 | 0.0032 | 313 | 267.2 | 88 | 0.0040 | 251 |
| 251.0 | 103 | 0.0032 | 312 | 283.4 | 86 | 0.0043 | 232 |
| 267.3 | 95 | 0.0037 | 271 | 296.6 | 88 | 0.0044 | 227 |
| 281.3 | 87 | 0.0043 | 234 | 308.4 | 90 | 0.0045 | 222 |
| 293.1 | 87 | 0.0044 | 226 | 318.4 | 87 | 0.0048 | 209 |
| 303.1 | 89 | 0.0045 | 225 | 326.7 | 89 | 0.0048 | 208 |
| 311.5 | 93 | 0.0044 | 228 | 333.7 | 85 | 0.0052 | 193 |
| 318.4 | 91 | 0.0046 | 219 | 333.4 | 86 | 0.0051 | 196 |
| 207.2 | 183 | 0.0015 | 673 | 247.7 | 94 | 0.0035 | 288 |
| 231.6 | 103 | 0.0030 | 339 | 266.6 | 99 | 0.0036 | 282 |
| 251.3 | 85 | 0.0039 | 258 | 282.4 | 93 | 0.0040 | 251 |
| 267.2 | 91 | 0.0039 | 258 | 296.0 | 91 | 0.0043 | 233 |
| 280.9 | 91 | 0.0041 | 247 | 307.6 | 87 | 0.0046 | 216 |
| 292.8 | 87 | 0.0044 | 225 | 317.7 | 88 | 0.0047 | 212 |
| 303.0 | 92 | 0.0043 | 230 | 326.0 | 90 | 0.0048 | 210 |
| 311.3 | 90 | 0.0046 | 220 | 332.9 | 86 | 0.0051 | 197 |
| 318.4 | 94 | 0.0044 | 226 | | | | |

Table A.3.13: Haasen plot data for annealed CrMnFeCoNi high entropy alloy at 0.4% plastic strain amplitude. The red font color indicates data that were masked in the Haasen plots.

| **Specimen ID: HEA23 A4** | | | | **Specimen ID: HEA40 A4** | | | |
|---|---|---|---|---|---|---|---|
| **True Stress (MPa)** | **Stress Sensitivity of the Strain Rate ($\partial \ln \dot{\varepsilon}_p / \partial \ln \sigma$)** | **$b^2/\Delta a^*$** | **$\Delta a^*/ b^2$** | **True Stress (MPa)** | **Stress Sensitivity of the Strain Rate ($\partial \ln \dot{\varepsilon}_p / \partial \ln \sigma$)** | **$b^2/\Delta a^*$** | **$\Delta a^*/ b^2$** |
| 342.2 | 86 | 0.0052 | 192 | 342.3 | 84 | 0.0053 | 188 |
| 217.7 | 92 | 0.0031 | 322 | 213.2 | 104 | 0.0027 | 372 |
| 240.8 | 91 | 0.0035 | 289 | 237.0 | 88 | 0.0035 | 284 |
| 258.6 | 93 | 0.0037 | 274 | 255.0 | 80 | 0.0042 | 239 |
| 273.3 | 87 | 0.0041 | 243 | 270.2 | 79 | 0.0045 | 224 |
| 285.6 | 88 | 0.0043 | 235 | 283.1 | 79 | 0.0047 | 212 |
| 296.3 | 86 | 0.0045 | 221 | 294.0 | 79 | 0.0049 | 205 |
| 305.8 | 84 | 0.0048 | 210 | 303.9 | 78 | 0.0051 | 195 |
| 314.1 | 84 | 0.0049 | 203 | 312.5 | 80 | 0.0051 | 195 |
| 321.4 | 84 | 0.0050 | 200 | 320.1 | 84 | 0.0050 | 200 |
| 327.7 | 84 | 0.0051 | 196 | 327.0 | 83 | 0.0052 | 193 |
| 333.2 | 85 | 0.0052 | 194 | 333.0 | 82 | 0.0053 | 187 |
| 342.0 | 86 | 0.0052 | 192 | 342.2 | 88 | 0.0051 | 195 |
| 341.9 | 86 | 0.0052 | 192 | 342.3 | 83 | 0.0054 | 185 |
| 217.3 | 103 | 0.0028 | 362 | 213.5 | 107 | 0.0026 | 382 |
| 240.3 | 94 | 0.0034 | 297 | 237.2 | 86 | 0.0036 | 275 |
| 258.1 | 92 | 0.0037 | 272 | 255.3 | 77 | 0.0043 | 231 |
| 272.6 | 94 | 0.0038 | 262 | 270.4 | 75 | 0.0047 | 211 |
| 285.1 | 90 | 0.0041 | 241 | 282.9 | 78 | 0.0048 | 210 |
| 295.8 | 87 | 0.0045 | 224 | 294.0 | 80 | 0.0049 | 206 |
| 305.3 | 83 | 0.0048 | 208 | 303.7 | 81 | 0.0049 | 204 |
| 313.6 | 84 | 0.0049 | 204 | 312.7 | 78 | 0.0052 | 191 |
| 320.9 | 83 | 0.0051 | 197 | 320.2 | 81 | 0.0052 | 192 |
| 327.3 | 86 | 0.0050 | 199 | 327.0 | 82 | 0.0052 | 192 |
| 332.8 | 87 | 0.0050 | 199 | 332.8 | 85 | 0.0051 | 195 |
| 341.6 | 84 | 0.0053 | 188 | 342.2 | 85 | 0.0053 | 189 |

Table A.3.14: Haasen plot data for annealed CrMnFeCoNi high entropy alloy at 0.6% plastic strain amplitude. The red font color indicates data that were masked in the Haasen plots.

| **Specimen ID: HEA24 A6** | | | | **Specimen ID: HEA38 A6** | | | |
|---|---|---|---|---|---|---|---|
| **True Stress (MPa)** | **Stress Sensitivity of the Strain Rate $(\partial \ln\dot{\varepsilon}_p/\partial \ln\sigma)$** | **$b^2/\Delta a^*$** | **$\Delta a^*/ b^2$** | **True Stress (MPa)** | **Stress Sensitivity of the Strain Rate $(\partial \ln\dot{\varepsilon}_p/\partial \ln\sigma)$** | **$b^2/\Delta a^*$** | **$\Delta a^*/ b^2$** |
| 373.5 | 83 | 0.0059 | 169 | 378.3 | 82 | 0.0061 | 165 |
| 188.5 | 194 | 0.0013 | 782 | 202.0 | 176 | 0.0015 | 663 |
| 243.0 | 83 | 0.0038 | 261 | 255.5 | 81 | 0.0042 | 241 |
| 275.4 | 89 | 0.0041 | 247 | 287.9 | 77 | 0.0049 | 203 |
| 298.6 | 83 | 0.0047 | 212 | 310.4 | 80 | 0.0051 | 196 |
| 316.6 | 79 | 0.0052 | 191 | 327.6 | 80 | 0.0054 | 185 |
| 330.9 | 80 | 0.0055 | 183 | 341.1 | 81 | 0.0055 | 181 |
| 342.7 | 82 | 0.0055 | 182 | 351.9 | 82 | 0.0056 | 178 |
| 352.6 | 82 | 0.0057 | 177 | 360.8 | 83 | 0.0057 | 176 |
| 360.9 | 82 | 0.0058 | 173 | 367.9 | 83 | 0.0058 | 172 |
| 367.6 | 83 | 0.0058 | 173 | 373.6 | 86 | 0.0057 | 175 |
| 372.8 | 82 | 0.0060 | 167 | 378.1 | 82 | 0.0060 | 166 |
| 187.4 | 410 | 0.0006 | 1663 | 200.4 | 206 | 0.0013 | 780 |
| 241.6 | 84 | 0.0038 | 265 | 254.7 | 81 | 0.0041 | 242 |
| 274.2 | 91 | 0.0040 | 252 | 287.3 | 77 | 0.0049 | 203 |
| 297.7 | 81 | 0.0048 | 207 | 310.1 | 79 | 0.0051 | 195 |
| 315.6 | 79 | 0.0052 | 192 | 327.3 | 81 | 0.0053 | 188 |
| 330.0 | 80 | 0.0054 | 184 | 341.0 | 79 | 0.0056 | 177 |
| 341.9 | 81 | 0.0055 | 180 | 351.9 | 81 | 0.0057 | 176 |
| 351.8 | 83 | 0.0056 | 179 | 360.8 | 84 | 0.0056 | 178 |
| 360.1 | 83 | 0.0057 | 176 | 368.0 | 85 | 0.0057 | 177 |
| 366.9 | 81 | 0.0059 | 169 | 373.8 | 83 | 0.0059 | 170 |
| 372.3 | 84 | 0.0058 | 173 | 378.3 | 83 | 0.0060 | 167 |

## References

[1] L. Sheridan, J. E. Gockel, O. E. Scott-Emuakpor, Rapid initiation and growth life characterization of additively manufactured alloy 718 through compliance monitoring, *EML* 40 (2020) 100856.

[2] R. W. Schafer, What Is a Savitzky-Golay Filter?, *IEEE Signal Process Mag* 28 (4) (2011) 111-117.

[3] S. J. Orfanidis, Signal Processing Applications, in: S. J. Orfanidis (Ed.), Introduction to signal processing, *Prentice-Hall, Inc.*, 1995, pp. 321-471.

[4] ASTM International. E606-04: Standard Test Method for Strain-Controlled Fatigue Testing. *ASTM International*, West Conshohocken, PA, 2004.